

Polymer Melt Extrusion and Mixing Processes

an introductory course

emeritus-professor dr.ir. Han E.H. Meijer,
Xplore Instruments BV, Sittard, April 23-25, 2018

	Page
Contents	1
Introduction: Some illustrations of polymer processing	3
A Extruder and screws	3
B Shaping Dies	4
C Continuous processes	4
D Discontinuous processes	
1. Extrusion, some basics	7
1.1 Pumps based on drag flow	7
1.2 Drag and pressure flow	7
1.3 Pump characteristics	9
1.4 Influence of operating conditions and geometry on pump characteristics	10
1.5 Combining pump and die, geometry optimization	11
1.6 Extruders, geometrical considerations	13
1.7 Extruders, power use and energy optimization	16
1.8 Thermal issues	18
2. Modeling of continuous mixers	23
2.1 Summary	23
2.2 Co- versus counter-rotating twin screw extruders	23
2.3 Screw geometries	25
2.4 Analysis of simplified geometry	27
2.5 Analysis of complex geometries	29
2.6 Torque, energy and specific energy	33
3. Scaling of continuous mixers	35
3.1 Definition of the scaling problem	35
3.2 Governing equations	35
3.3 Geometrical scaling	39
3.4 Thermal scaling	40

3.4a	Thermal scaling for laminar flows	41
3.4b	Thermal scaling for well-mixed flows	42
3.4b ₁	First choice: $l = 1$	42
3.4b ₂	Second choice: $h = 1$	43
4.	Mixing	45
4.1	Distributive versus dispersive mixing	45
4.2	Distributive mixing; $Ca \gg Ca_{crit}$	48
4.2a	Linear versus exponential mixing	48
4.2b	Couette flow	49
4.2c	Cavity flow	50
4.3	Static mixers	54
4.3a	Kenics mixer	54
4.3b	SMX mixer	55
4.3c	Optimizing mixers to compactness or pressure drop	56
4.4	Dynamic mixers	60
4.5	Dispersive mixing	61
4.5a	Disintegration of threads into a row of droplets	61
4.5b	Break up of drops	64
4.5c	Drops or threads	67
4.5d	Coalescence of drops	69
4.6	A simplified dynamic model	71
4.6a	Transient mixing process	72
4.6b	Optimization of viscosity ratio p	74
4.6c	Optimization of mixer geometry	75
5.	List of symbols	78
6.	References	80

Colour use:

drag flow, pressure flow, important to remember, background information

Introduction:

Some illustrations of polymer processing

A. Extruder and screws

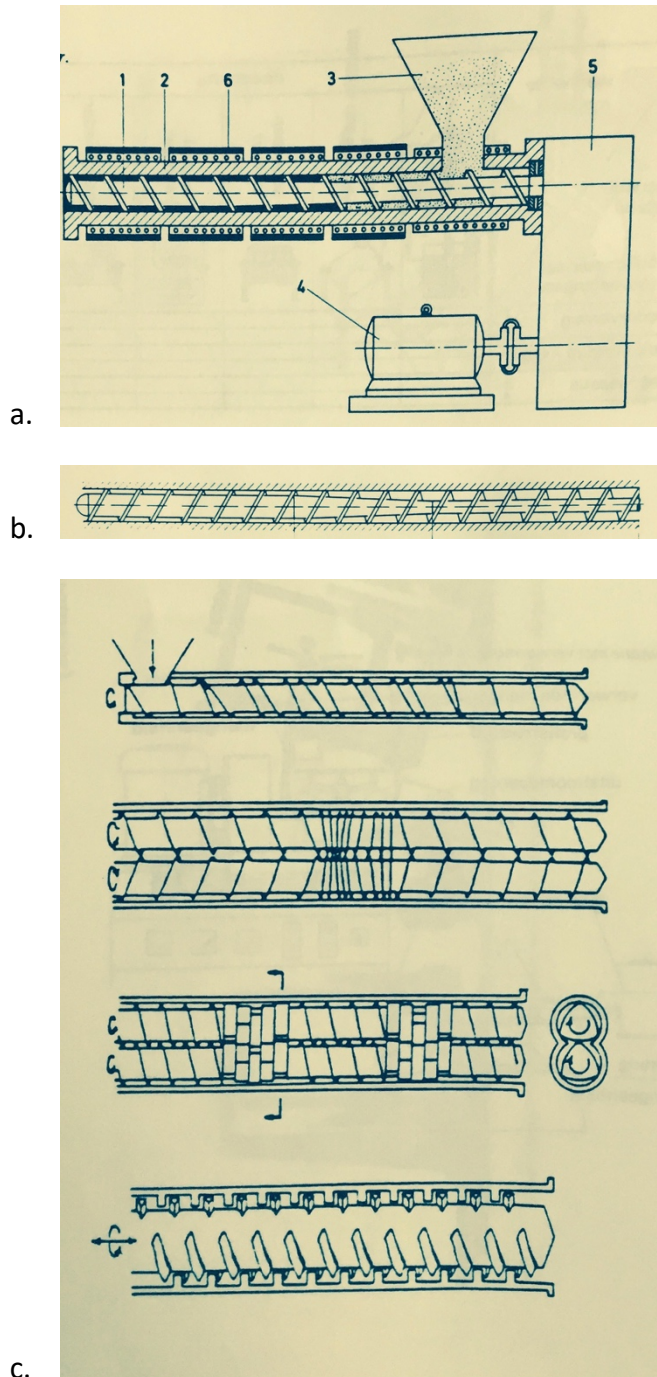


Figure 1 (a) Single screw extruder, (b) standard 3-zone compression screw, (c) from top to bottom: Maillefer phase-separating screw, counter-rotating twin screw, co-rotating twin screw, and Buss co-kneader.

B. Shaping Dies

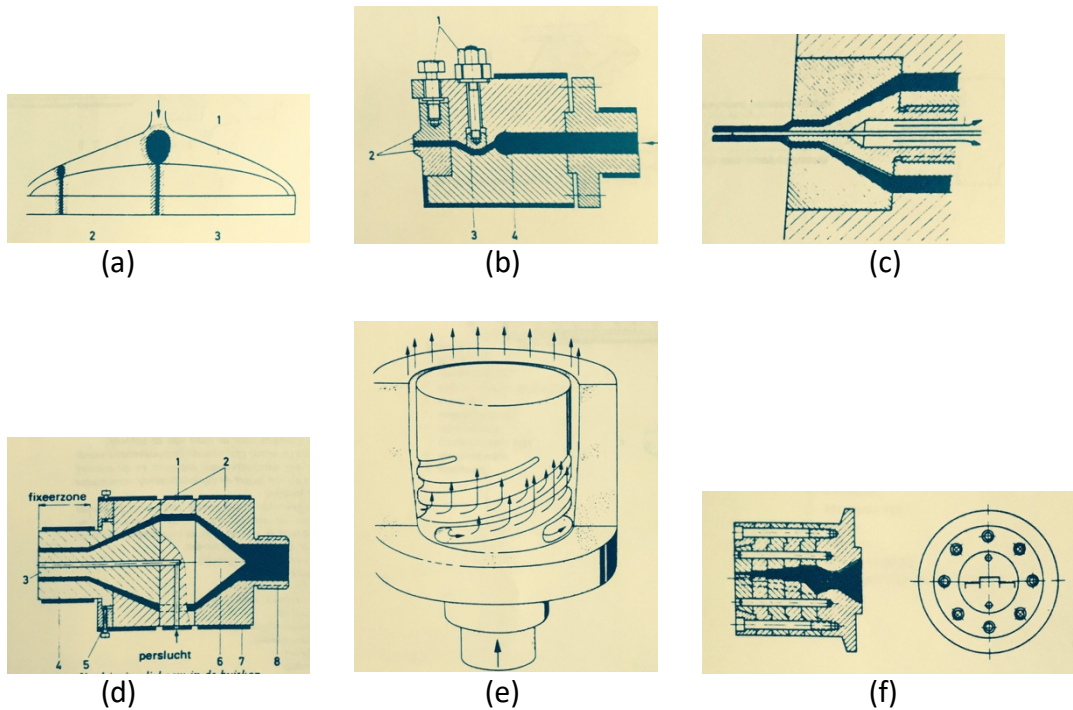
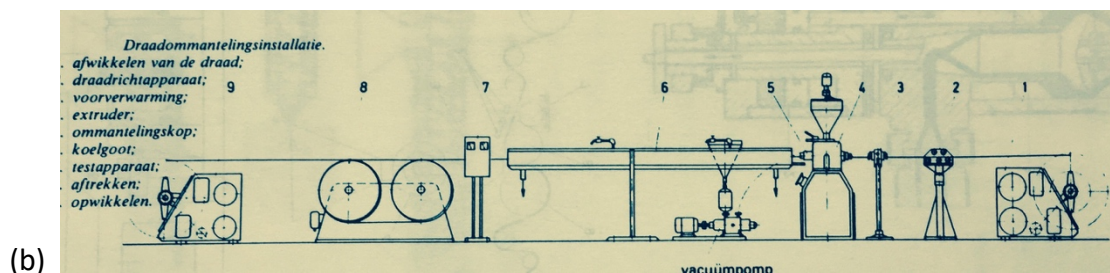
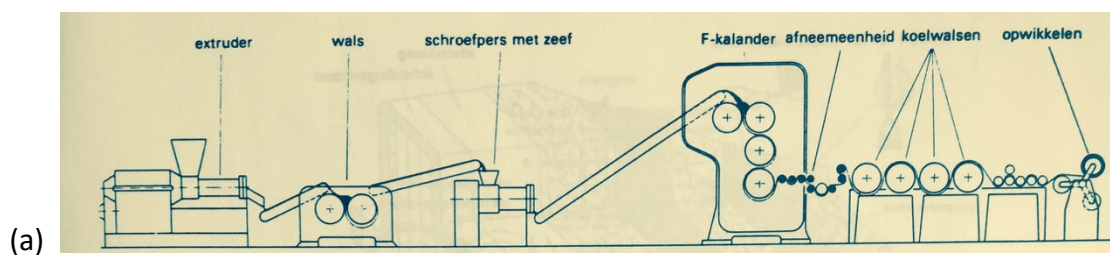
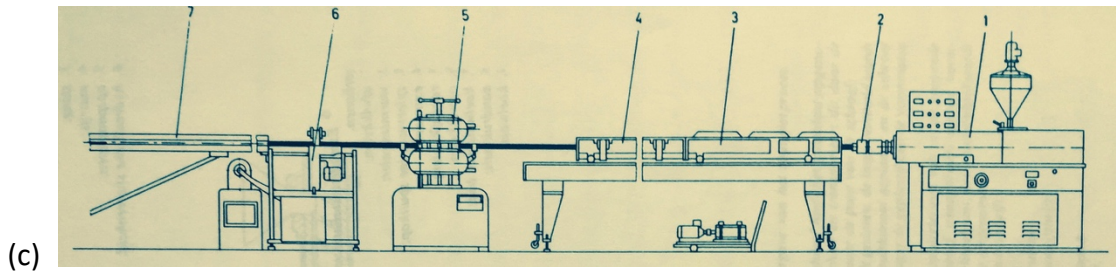


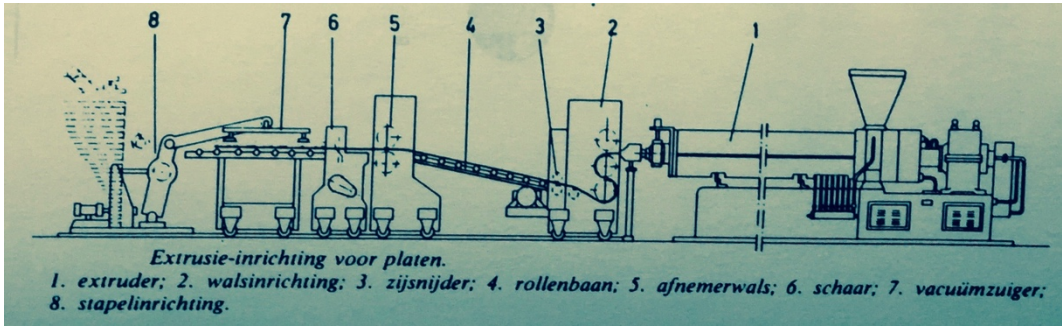
Figure 2 (a) and (b) coat hanger die, (c) cable coating die, (d) tube die and (e) tube die with modern 'wendelverteiler', and (f) profile die.

C. Continuous processes

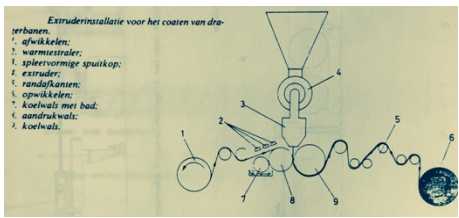




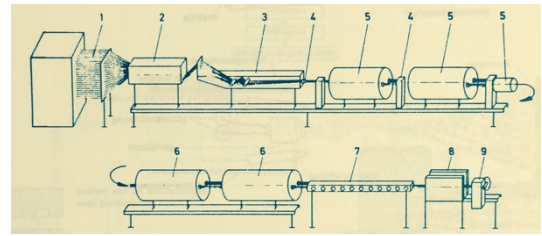
(c)



(d)



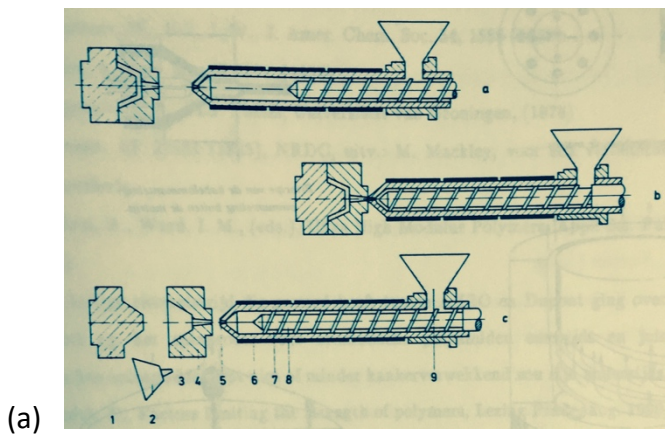
(e)



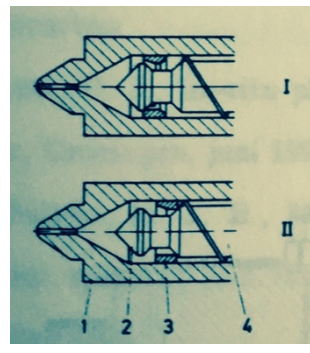
(f)

Figure 3 (a) sheet extrusion with calendering, (b) cable coating, (c) tube extrusion, (d) plate extrusion (e) paper coating, and (f) pulltrusion.

D. Discontinuous processes



(a)



(b)

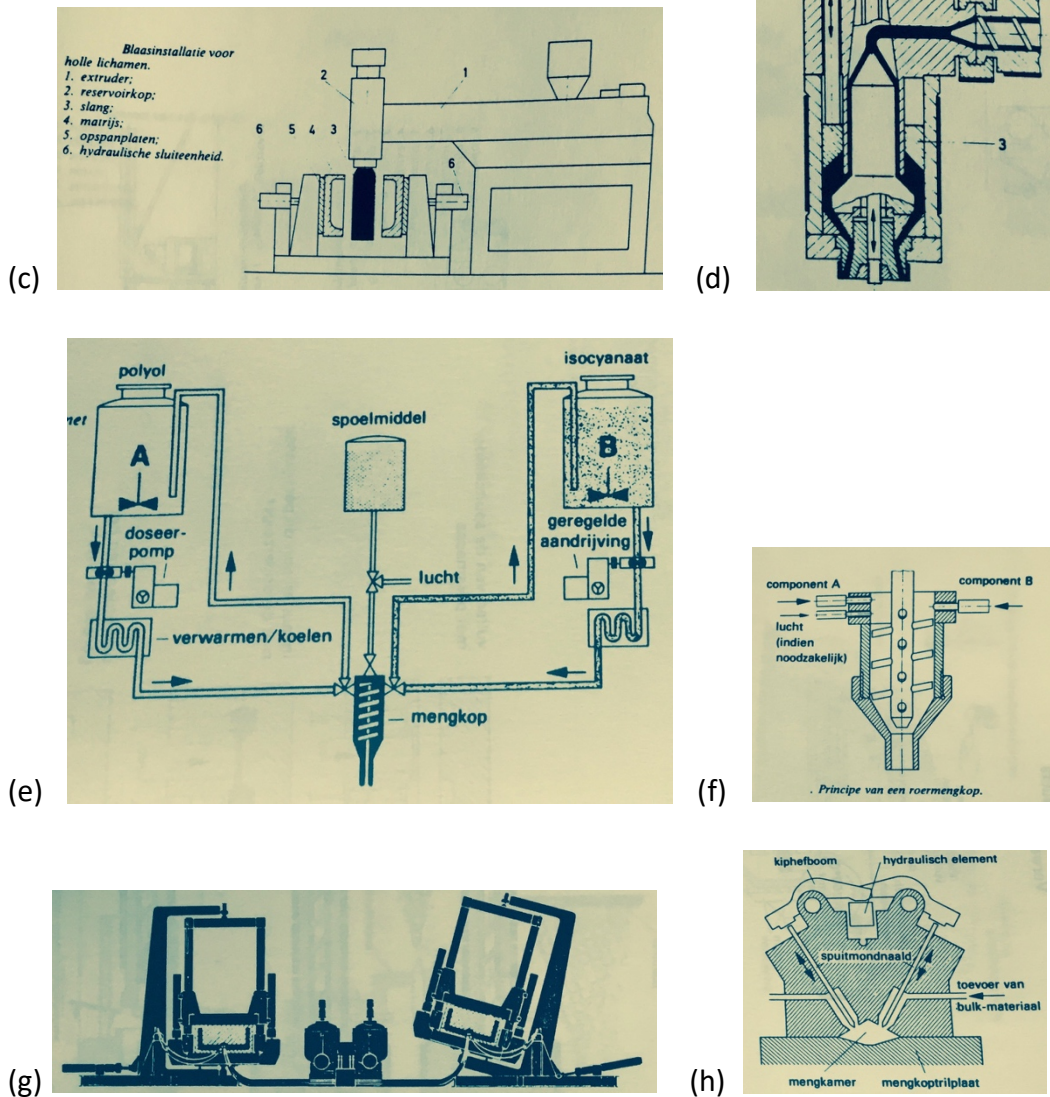


Figure 3 (a) injection moulding, (b) closing valve at screw end, (c) container blowing with (d) accumulator, (e) and (g) reaction injection moulding, and (f) and (h) mixing reactive components.

1. Extrusion, some basics

1.1 Pumps based on drag flow

Pumps can be distinguished based on their working principle, (open) drag flow or (closed) positive displacement flow. If a (small) object, like a sphere, can freely move through the pump, by tilting or holding it upside down, we deal with a drag pump, if the sphere can not move and stays captured, it is a displacement pump. Examples of the last are injection needles, bicycle tyre pumps, gear pumps and (their axial extended version:) counter-rotating closely intermeshing twin screw extruders. All other pumps are based on drag flow en examples include ventilators, turbines, wind mills, blade coaters, two roll mills, calendars, and single screw and co-rotating twin screw extruders. A pump is used to force a fluid through a resistance. The simplest, 2-dimensional, representation of such a combination is given in Figure 1.1.

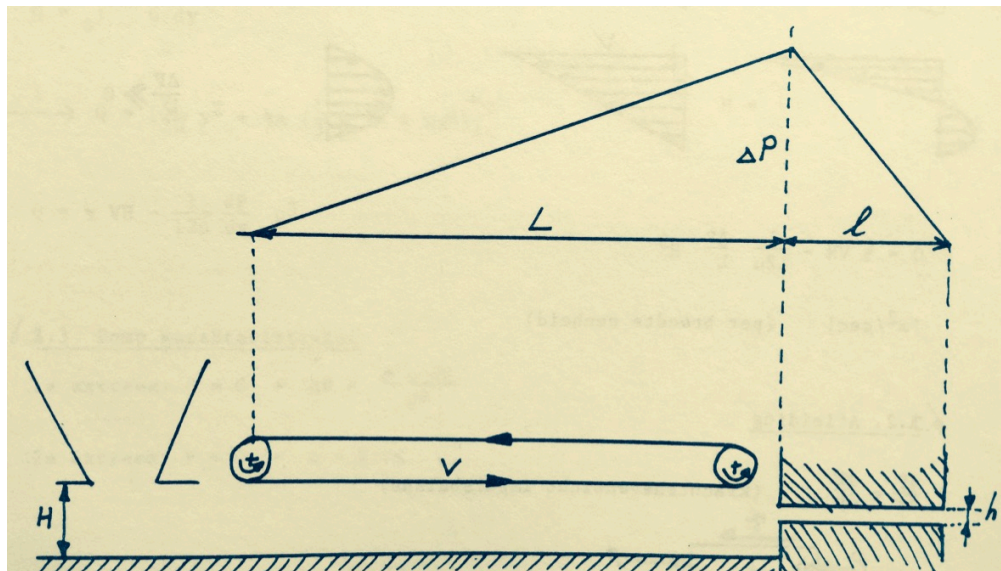


Figure 1.1 Two-dimensional drag pump with height H , and length L , running at drag speed V (to produce a pressure difference ΔP), combined with a resistance of height h and length l (that consumes the same pressure difference ΔP to drive the fluid through).

Inside the drag pump the combined drag flow and pressure flow results in the effective throughput Q , in this 2-dimensional example with dimension $[m^2/s]$. (If you prefer the 3D case of a physical throughput Q of $[m^3/s]$, please add a width B to both pump and die of $B = 1$ $[m]$).

1.2 Drag and pressure flow

Figure 1.2 illustrates how throughput Q is the sum of drag flow $\frac{1}{2}VH$ and pressure flow $(\frac{H^3}{12\mu}) * \Delta P/L$, in three cases with different sign and magnitude of the pressure gradient $\Delta P/L$. The middle example shows that locally the pressure gradient can be negative, such that the pressure flow adds to the drag flow to increase the total flow. The bottom example shows

what happens if we increase the die resistance such that it is almost closed: the throughput diminishes and the fluids start circulating.

$$Q = \frac{1}{2}VH + (H^3/12\mu) * \Delta P/L \tag{1.1}$$

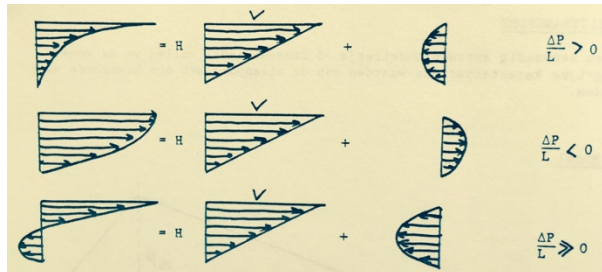


Figure 1.2 Throughput Q [m^2/s] equals the sum of the drag flow $\frac{1}{2}VH$ and the pressure flow $(H^3/12\mu) * \Delta P/L$.

Derivation:

Rather than a complete treatment of the momentum equations, we prefer to use here a pretty simplified version. We define: the pressure P [$Pa = N/m^2$], the shear stress τ [Pa], the viscosity μ [$Pa.s$] and the length segments dx [m] and dy [m]. A local stress analysis over a small area $dx.dy$ illustrates that the pressure gradient dP/dx is balanced by de shear stress gradient $d\tau/dy$:

$$dP/dx = d\tau/dy \tag{1.2}$$

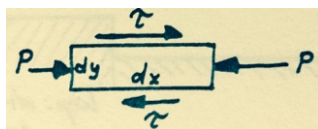


Figure 1.3 Stresses acting on a small local area with length dx and height dy , balancing the shear stress τ (that acts on the length segment dx) and the normal stress P (that acts on the height segment dy).

since the horizontal force balance reads $(P_{x+dx} - P_x).dy = (\tau_{y+dy} - \tau_y).dx$
 while $P_{x+dx} = P_x + (dP/dx).dx$
 and $\tau_{y+dy} = \tau_y + (d\tau/dy).dy$

Rather than dealing with complex rheology, we prefer to use here the simplest fluid. The pumping fluid is **Newtonian**. It linearly relates the shear stress τ to the velocity gradient du/dy , with the proportionality constant, the viscosity μ , constant:

$$\tau = \mu du/dy \tag{1.3}$$

Combining Eqs (1.2) and (1.3) yields:

$$dP/dx = \mu \cdot d^2u/dy^2$$

two times integration gives $\rightarrow du/dy = A y + C_1 \rightarrow u = \frac{1}{2} A y^2 + C_1 y + C_2$ (1.4)

with $A = 1/\mu (dP/dx)$

Using the two boundary conditions of the flow in the drag pump of Figure (1.1)

$$\begin{aligned} y=0 & \quad u=0 & \rightarrow C_2=0 \\ y=H & \quad u=V & \rightarrow C_1=(V-\frac{1}{2} A H^2)/H \end{aligned} \quad (1.5)$$

yields the velocity profile:

$$u = V/H y + \frac{1}{2} A (y^2 - Hy) \quad (1.6)$$

Integration of the velocity over the height gives the throughput:

$$\begin{aligned} Q &= \int_0^H u dy \rightarrow Q = [\frac{1}{2} V/H y^2 + \frac{1}{2} A (1/3 y^3 - \frac{1}{2} H y^2)]_0^H \\ Q &= \frac{1}{2} VH + (H^3/12\mu) * \Delta P/L \end{aligned} \quad (1.7)$$

1.3 Pump characteristics

Eq. (1.1) represents the collection of all operating points of the pump, relating the throughput Q to the pressure gradient $\Delta P/L$. Since the pressure gradient is constant, we can also construct $Q - \Delta P$, the pump characteristic, see Figure (1.4). The intercepts are found by substituting $Q = 0$ and $\Delta P = 0$ in Eq (1.1) :

$$\begin{aligned} Q=0 & \rightarrow \Delta P = 6\mu VL/H^2 \\ \Delta P=0 & \rightarrow Q = \frac{1}{2} VH \end{aligned} \quad (1.8)$$

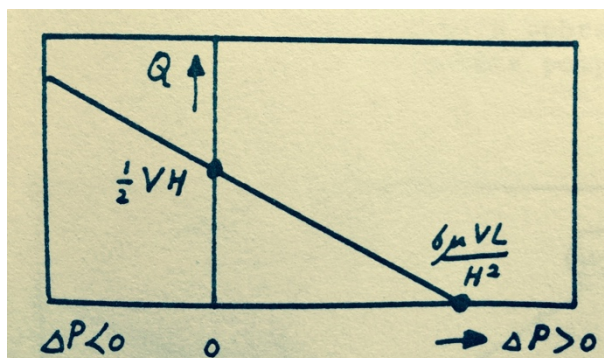


Figure 1.4 Pump characteristic.

Note that the line extends to the area of negative pressure difference (pressure is consumed, $\Delta P < 0$) and, therefore, negative pressure gradient, $\Delta P/L < 0$, see *Figure (1.2 middle)*.

1.4 Influence of operating conditions and geometry on pump characteristics

If the pump is a rotary device, like an extruder, the wall velocity V relates to the rotational speed N [rpm]:

$$V = \pi D N / 60 \quad (1.9)$$

with V the wall velocity [m/s], D the screw diameter [m] and N the screw rotational speed [rpm]. Both intercepts are proportional to V , see *Eq (1.7)* and *Figure (1.4)*, therefore changing N gives a parallel shift of the pump characteristics, see *Figure (1.5)*:

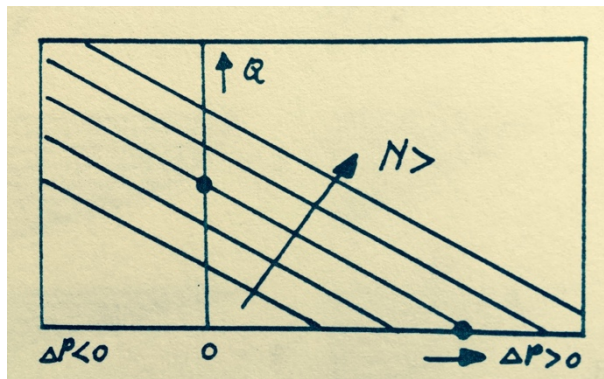


Figure 1.5 Pump characteristics; influence of screw speed N [rpm].

Interesting is to investigate the influence of the pump channel height H . From *Eq (1.7)* and *Figure (1.4)* we learn that the throughput Q (intercept at $\Delta P = 0$) is proportional to H , while the pressure build up ΔP (intercept $Q = 0$) is proportional to $1/H^2$. Changing H , therefore, causes a tilting of the pump characteristic, see *Figure (1.6)*:

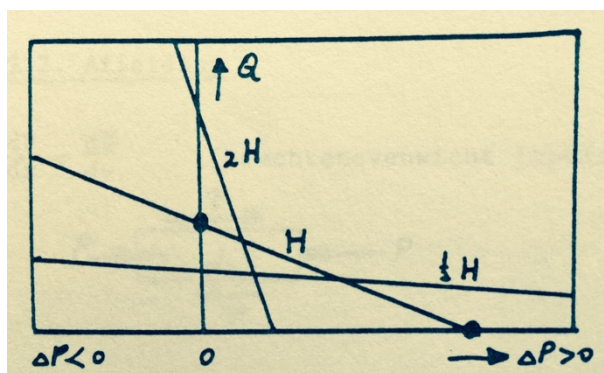


Figure 1.6 Pump characteristics; influence of channel height H [m].

This explains why pumps that require a high throughput against a small pressure difference (ventilators) have deep channels, while load bearing spiral groove bearings have very shallow channels; this now is explained in more detail in the next *Section 1.5*.

1.5 Combining pump and die, geometry optimization

The operating point of a pump–resistance combination is found by the intersection point of the pump characteristic, see *Figures (1.4 – 1.6)* and the die characteristic, see *Figure (1.7)*. In the die no moving parts are present, and only pressure flow exists. The throughput Q is proportional to the pressure drop ΔP over the die:

$$Q = (h^3/12\mu)*\Delta P/l \tag{1.10}$$

or

$$Q = k/\mu*\Delta P \quad \text{with} \quad k = 1/w \tag{1.11}$$

With h is the height and l the length of the die, and k [m^2] and w [$1/m^2$] constants that indicate the die resistance. The derivation of *Eq. (1.10)* is identical to the one of the pump characteristic, *Eqs. (1.2 – 1.7)*, if one puts $V = 0$ and realizes that ΔP over the die is negative.

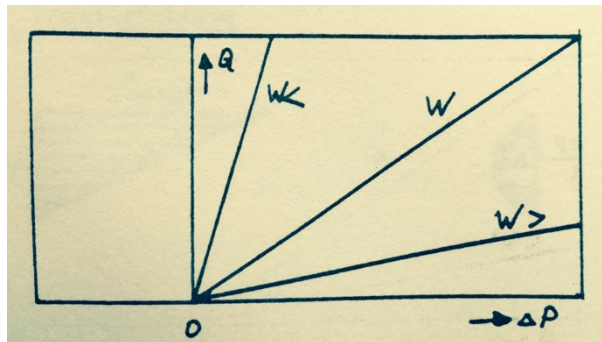


Figure 1.7 Die characteristics for die's with a small, intermediate and large resistance W .

Combining pump and die characteristics in one plot, see *Figure (1.8)*, gives the collection of working points of the pump-die combination. On the vertical axis we read the throughput–screw speed characteristic ($Q - N$), on the horizontal axis the pressure ($\Delta P - N$).

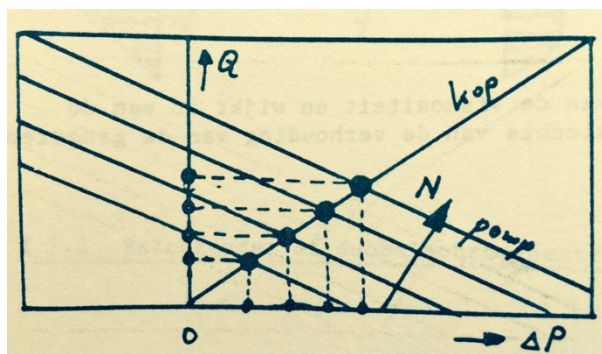


Figure 1.8 Pump and die characteristics and their intersection points, yielding the throughput ($Q - N$) and pressure build up ($\Delta P - N$) relations of this pump–die combination.

Next we optimize the pump with respect to the throughput using as a parameter the pump height ($2H$, H , and $\frac{1}{2} H$) for different die resistances ($w <$, w , and $w >$), see Figure (1.9):

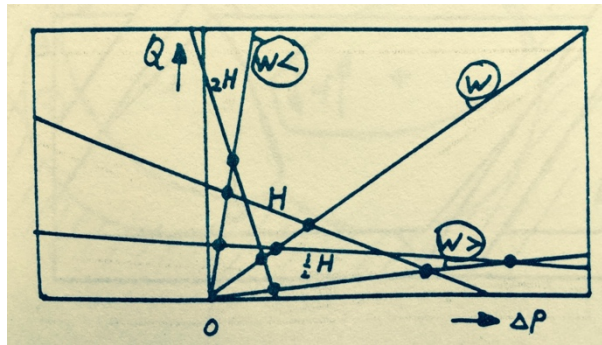


Figure 1.9 Optimization of pump height for different resistances of the die.

Clearly, for bigger dies, with small resistances ($w <$), the deeper channel is the better ($2H$) with respect to throughput. For intermediate resistance (w), the intermediate height (H) gives the best result, while small die's with a large resistance ($w >$) require shallow channel heights ($\frac{1}{2} H$).

The working points of the pump–die combination can also be expressed in a simple equation: Eqs (1.1) and (1.10) give expression for the throughput–pressure drop relations in pump and die:

$$Q = \frac{1}{2} V H + (H^3 / 12 \mu) * \Delta P / L \quad \text{and} \quad Q = (h^3 / 12 \mu) * \Delta P / l$$

The throughput Q in both is the same (integrated continuity equation, expressing conservation of mass), therefore:

$$\frac{1}{2} V H + (H^3 / 12 \mu) * \Delta P / L = (h^3 / 12 \mu) * \Delta P / l \tag{1.12}$$

Solving Eq. (1.12) for the pressure difference yields:

$$\Delta P = 6 \mu V H / (H^3 / L + h^3 / l) \tag{1.13}$$

The pressure differences is proportional to viscosity and screw speed, and depends further on the geometry. While substituting Eq. (1.13) in Eq. (1.1) yields for the throughput:

$$Q = \frac{1}{2} V H / \{1 - 1 / [1 + (h/H)^3 L / l]\} \tag{1.14}$$

With as result that the throughput depends on screw speed and channel depth, and some ratio's of the details of the geometry of the combination, but most interesting it is **independent** of the viscosity. And that is exactly why extruders are used in polymer processing. The viscosity of the long-chain polymers is huge. In a pump–die combination, extruders pump independent of that viscosity. Only the pressure, in front of the die, directly depends on the viscosity of the fluid.

1.6 Extruders, geometrical considerations

The drag pump sketched in *Figure (1.1)* does not directly look like an extruder, but still it represents exactly what happens locally in real machines. To understand that, we take a look at a simple single screw extruder, with channel height H and pitch angle ϕ . In this extruder, we consider the screw stationary, and make the barrel wall to rotate in opposite direction with velocity V which relates to the screw speed N accordingly to *Eq. (1.9)*. The velocity V is in circumventor direction and can be decomposed into a in-channel component $V \cos\phi$, and a cross-channel component $V \sin\phi$, see *Figure (1.10)*.

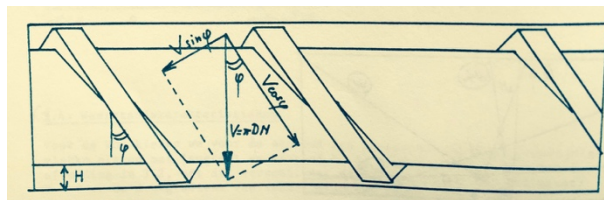


Figure 1.10 Geometry of a single screw extruder; the screw is thought stationary, the barrel rotates in opposite direction with speed $V = \pi D N/60$.

The in-channel component $V \cos\phi$ drags the fluid towards against the pressure difference ΔP towards the die. The cross-channel component $V \sin\phi$ makes the fluid rotate in the cross-section (no transport in cross-channel direction is possible, because of the presence of the screw flight; leakage over the flight is neglected here for simplicity), see *Figure (1.11)*. Together both velocity components form a spiral motion inside the channel towards the exit die.

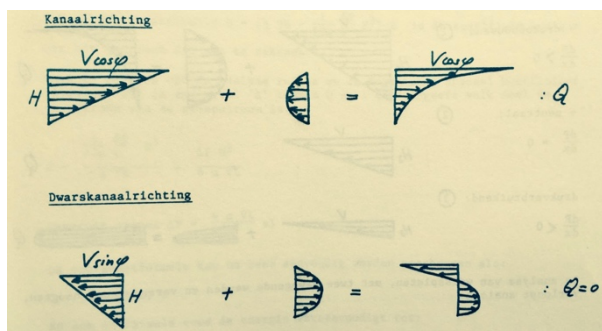


Figure 1.11 In-channel (top) and cross-channel (bottom) velocity profile, locally inside the channel of a single screw extruder.

This spiral motion inside the channel is again spiralled, since the channel is spiralled around the central screw shaft. Usually in extruder analyses, this last spiral is neglected, by unrolling the screw channel from the screw shaft. As a consequence, the screw channel degenerates to a straight gutter under an angle ϕ , of height H and width $W = \pi D \sin\phi - e$, where D is the screw diameter and e represents the flight width, over which an infinite plate, the unrolled barrel wall, moves with velocity V . This makes the extruder, *Figure (1.10)*, in the end, functionally look like the drag pump in *Figure (1.1)*.

Rather often in polymer processing equipment, the channel height H is not constant, but changes continuously. This has a direct effect of the local capacity of the drag flow. Given continuity of mass and, with constant density, continuity of volume to be transported, this results in an interesting interplay of geometry and drag and pressure flows. Pump and resistance are fully integrated. As an example, we consider the local cross-sectional flow in one arm of a batch mixer or one screw of a co- or counter-rotating twin screw extruder, see *Figures (1.12) and (1.13)*.

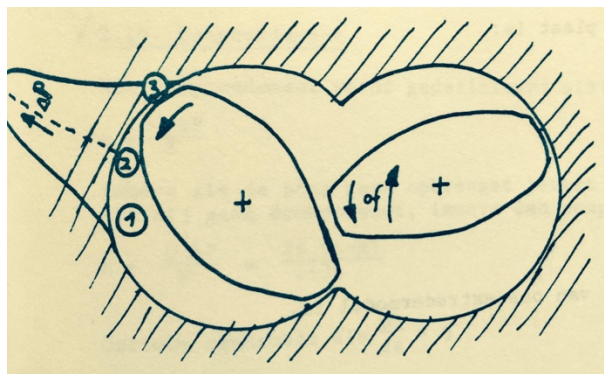


Figure 1.12 Cross-sectional flow in a batch mixer or a co- or counter-rotating twin screw extruder.

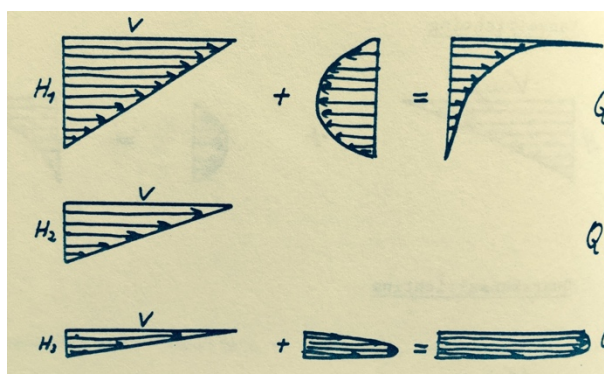


Figure 1.13 Drag- and pressure flow in the three locations (top, middle, bottom) as indicated in *Figure (1.12)* (1, 2, and 3, respectively). The throughput Q in all

three positions is the same. Continuity of Q determines the magnitude of the local pressure gradients.

In the cross-section the pressure on some distance of the screw or kneading flight is the same, in case of partially filled systems even $P = P_0$. On position 1, with large H , the drag flow is large, and pressure can be build up, ($dP/dx > 0$). On position 2, the drag flow is just sufficient to transport the fluid Q , so there the pressure gradient is zero, ($dP/dx = 0$). Finally, on position 3, the drag flow is too small and must be supported by pressure flow with negative pressure gradient to transport Q , ($dP/dx < 0$). Starting at $P = P_0$ the total pressure profile can be sketched, see *Figure (1.12)*.

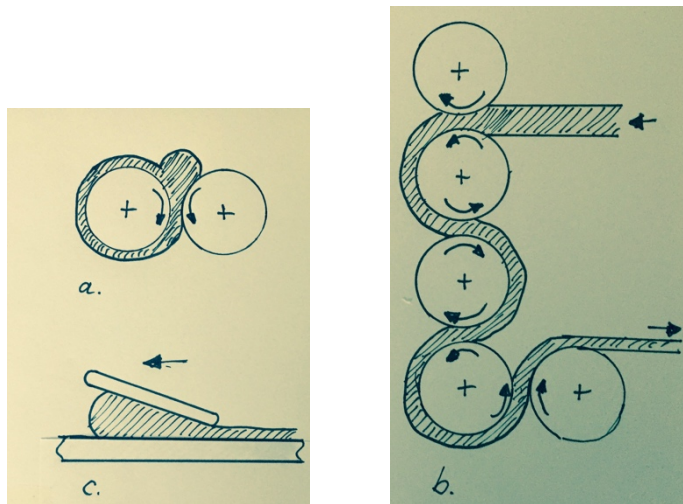


Figure 1.14a Integrated drag pump and resistance: (a) two roll mill, (b) calender, and (c) blade coating.

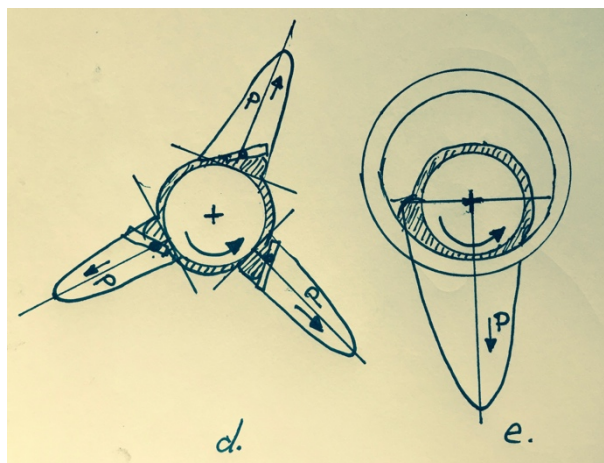


Figure 1.14b Two examples from tribology: (d) Mitchell block bearing, and (e) journal bearing.

The same holds for the two-roll mill process, more-roll calendering process, blade coating process and, in tribology, the Mitchell block bearing (a kind of triple blade coating process) and the full cylindrical journal bearing, see *Figures (1.14_{a,b})*.

When we consider the continuous change in channel height in all these devices consisting of a series of sections with parallel flows and a systematic change in height, a complete analysis can be done, even with the simplified equations as derived in this chapter, to compute both throughput Q as well as maximum pressure P . So analyses can be done quantitatively. **You can compute how much force you have to put on your knife to produce a thin slice of butter on your bread.**

Also the conical co-rotating twin screw extruder (with free entrance and exit in the example of *Figure (1.15)*) shows a large drag flow at the feed and, therefore, a large positive pressure gradient that gives the ability to build up pressure (*Figure (1.13 top)*). At some point along the screw axis, the channel depth is just sufficient to transport the throughput Q just by drag flow, and the pressure gradient is zero leading to a maximum in pressure (*Figure (1.13 middle)*). Finally, at the end of the screw the channels are shallow, the drag flow small and the pressure flow must help transporting Q , therefore the pressure gradient is negative (*Figure (1.13 bottom)*), lowering the pressure towards zero.

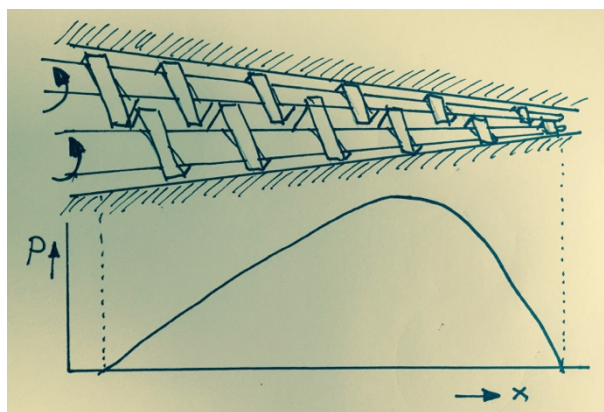


Figure 1.15 Integrated drag pump and resistance: The conical corotating twin screw extruder has a decreasing channel depth. Therefore at the entrance the drag flow is large, somewhere on 2/3 of its length the drag flow is just sufficient to transport the throughput Q . At the end of the screws it is by far insufficient, and pressure flow must support transport.

1.7 Extruders, power use and energy optimization

Next we investigate how much torque and energy is required to operate an extruder, as an example of a pump based on drag flow. **In words:**

In extruders the torque T_o equals the total force F on the wall times the radius $\frac{1}{2} D$. The force F equals the (shear)stress-at-the-wall times the total-wall-surface. The energy E equals the force times the screw speed (in [revolutions per second]).

Given the Newtonian pumping fluid, Eq (1.3), the wall shear stress equals:

$$\tau = \mu \, du/dy|_{y=H}$$

From Eqs (1.4) and (1.5) we find for the wall shear rate (by substitution $y = H$):

$$du/dy|_{y=H} = \Delta P/2\mu \cdot H/L + V/H$$

The torque T_o [Nm] on an extruder with diameter D [m], channel length L [m] and height H [m] and axial length L_{ax} [m] is:

$$T_o = \frac{1}{2} L_{ax} \pi D^2 (\mu V/H + \frac{1}{2} \Delta P H/L) \quad (1.15)$$

and the energy E [J/s] = [Nm/s] per unit of extruder channel width B [m], of an extruder of channel length L [m], equals:

$$E/B = \mu V^2 L / H + \frac{1}{2} \Delta P V H \quad (1.16)$$

The throughput Q per unit of extruder channel width B reads, Eq (1.1):

$$Q/B = \frac{1}{2} V H + (H^3/12\mu) * \Delta P/L$$

Introducing the so-called “drossel-ratio” a , which is a number between $0 \leq a \leq 1$ that expresses the ratio of pressure flow to drag flow:

$$a = (H^3/12\mu) * \Delta P/L / \frac{1}{2} V H$$

$$a = \Delta P H^2 / 6 \mu V L \quad (1.17)$$

thus also: $\Delta P = 6 \mu V L / H \cdot a \quad (1.18)$

the throughput reads:

$$Q/B = \frac{1}{2} V H (1-a) \quad (1.19)$$

and the energy:

$$E/B = \mu V^2 L / H (1+3a) \quad (1.20)$$

Combining Eqs (1.19) and (1.20) gives the **specific energy**:

$$E_{sp} = E/Q = 2\mu V L / H^2 \cdot (1+3a)/(1-a) \quad (1.21)$$

The specific energy E_{sp} [J/m³] represents the mechanical energy pumped into the fluid that causes it to increase in temperature. Generally, extrusion strategies (screw design and operating conditions) aim at keeping the specific energy as low as possible in order to prevent overheating and burning of the polymers.

Finally, we define the pump **efficiency** η [-] as:

$$\eta = Q\Delta P/E \quad (1.22)$$

since a pump that does not pump ($Q = 0$) is not a pump, while a pump that does not generate pressure ($\Delta P = 0$) is also no pump.

Substituting Eqs. (1.18), (1.19), and (1.20) in (1.22) gives:

$$\eta = 3a(1-a)/(1+3a) \quad (1.23)$$

A beautiful, simple, result.

The optimum efficiency can be found by differentiating η with respect to a and setting it zero:

$$d\eta/da = 0$$

$$d\eta/da = 3(a+1)(1-3a)/(1+3a)^2 = 0$$

with solutions: $a = -1$ and $a = 1/3$ (1.24)

Substituting the real solution $a = 1/3$ in Eq. (1.23) shows that the maximum efficiency of extruders equals: $\eta_{max} = 1/3$. The extruder efficiency as a function of the drossel ratio a is shown in Figure (1.16).

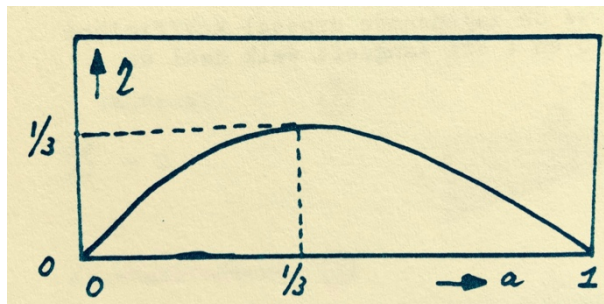


Figure 1.16 Extruder efficiency as function of ratio between pressure flow and drag flow.

From the analysis in the Section 1.7, and Section 1.5, Eq. (1.14), we can conclude that extruders are viscosity independent pumps with only a moderate efficiency of ~30%. The majority of the mechanical energy brought into the system by the motor (~70%) is dissipated into heat. This brings us to the next section, that deals with thermal issues.

1.8 Thermal issues

With a rather simplified approach we will try to illustrate the most important factors determining the temperature changes along the extruder axis during pumping. This is

relevant since the viscosity of polymers is high, and most of the mechanical energy is dissipated into heat.

A basic heat balance is shown in Figures (1.17) and (1.18):

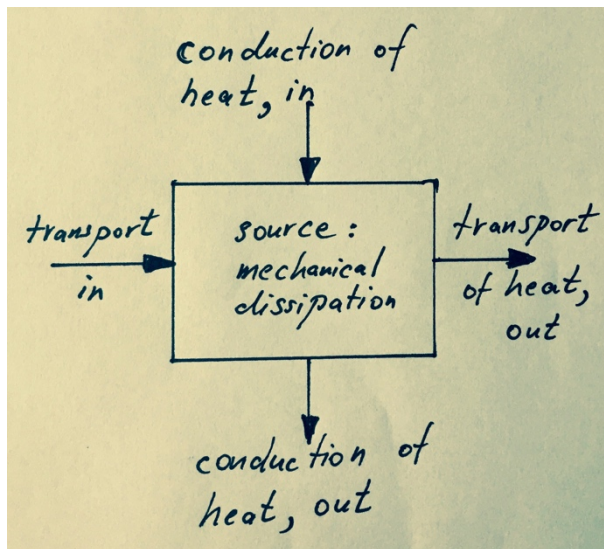


Figure 1.17 Local heat balance.

- With
- u = velocity [m/s]
 - ρ = density [kg/m³]
 - c = heat capacity [J/kg⁰C]
 - T = temperature [°C]
 - q'' = heat flux density [J/sm²]
 - D_{is} = heat dissipation [J/sm³]
 - λ = heat conductivity coefficient [J/sm⁰C]

we can cast Figure (1.17) in equation form, see Figure (1.18):

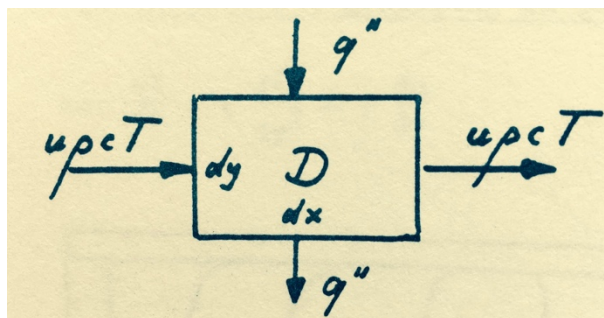


Figure 1.18 Local heat balance.

Using $T_{x+dx} = T_x + dT/dx \cdot dx$ and $q''_{y+dy} = q''_y + dq''/dy \cdot dy$ the net heat transport and net heat conduction (in – out) equal:

$$u\rho c dT/dx \cdot dx dy \quad \text{and} \quad dq''/dy \cdot dx dy$$

The dissipation D_{is} works in the total volume, see its dimension, thus in this 2D case it equals:

$$D_{is} \cdot dx dy$$

The sum of all contributions results in heat accumulation in the test volume, here in 2D:

$$\rho c dT/dt \cdot dx dy$$

such that the total heat balance reads:

$$\rho c dT/dt = u\rho c \cdot dT/dx + dq''/dy + D_{is} \quad (1.25)$$

In stationary situation, thus after the start up of the pumping process, $dT/dt = 0$. Furthermore in shear flow: $D_{is} = \tau \cdot du/dy$ and, by applying Fourier's law: $q'' = -\lambda dT/dy$ with λ the heat conductivity coefficient, and Newton's law $\tau = \mu \cdot du/dy$ with μ the viscosity, we reach our final result:

$$u\rho c dT/dx = \lambda d^2T/dy^2 + \mu (du/dy)^2 \quad (1.26)$$

In words: the flow transported with temperature T and speed u will change in temperature due to heat conducted into the system and heat dissipated inside the system. The volumetric heat capacity of the fluid (ρc) in [J/m³. °C] transforms energy into temperature change.

Two simplified cases can be considered. The first where the system is at rest ($u = 0$) and the second when the system is moving but in equilibrium ($dT/dx = 0$).

First case: $\lambda d^2T/dy^2 = 0 \quad (1.27)$

two times integration gives $\rightarrow dT/dy = C_1 \rightarrow T = C_1 y + C_2$

with boundary conditions $y = 0 \rightarrow T = T_0$
 $y = H \rightarrow T = T_1$

the linear temperature profile is found:

$$(T-T_0)/(T_1-T_0) = y/H \quad (1.28)$$

Second case: $\lambda d^2T/dy^2 + \mu (du/dy)^2 = 0$

two times integration gives $\rightarrow dT/dy = A y + C_1 \rightarrow T = \frac{1}{2} A y^2 + C_1 y + C_2$ (1.29)

with $A = \mu/\lambda \cdot (V/H)^2$

Realizing that the average shear stress in the channel equals:

$$du/dy = V/H$$

and using the two boundary conditions

$$\begin{array}{ll} y = 0 & T = T_0 \\ y = H & T = T_1 \end{array}$$

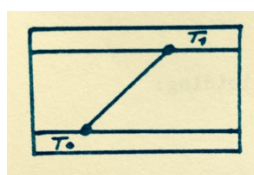
and the definition of the Brinkman number that reflects the ration of heat dissipation to heat conduction:

$$Br = \frac{1}{2} \mu V^2 / \lambda (T_1 - T_0) \tag{1.30}$$

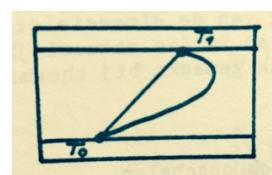
the temperature profile is found:

$$(T - T_0) / (T_1 - T_0) = y/H + Br \cdot [y/H \cdot (1 - y/H)] \tag{1.31}$$

Both cases are illustrated in *Figure (1.19)*:



Case 1: Heat conduction only



Case 2: Heat conduction and dissipation

Figure 1.19 Temperature profiles over the channel height.

In real practice neither of the two cases occur; we move with velocity u and thus dissipation is present, but we do not reach equilibrium. Generally, we are underway from the initial feed temperature towards the full equilibrium situation of case 2, see *Eq. (1.26)* and *Figure (1.20)*.

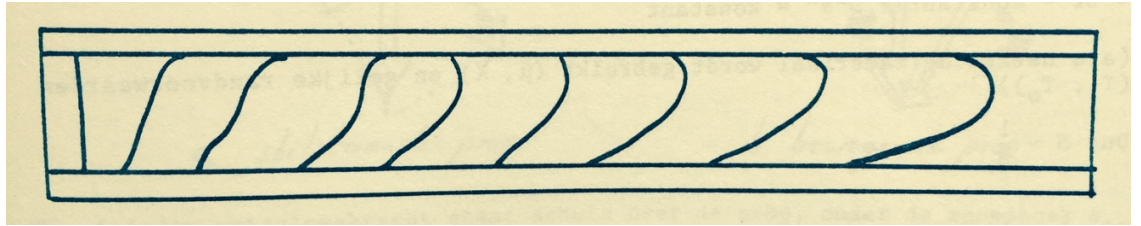


Figure 1.20 Illustration of the temperature profile over the channel height as it develops along the pump, extruder, axis.

Eq. (1.26) is not easy to solve. It can be made dimensionless to reveal the characteristic dimensionless numbers that determine the temperature development. One of them we already met: the **Brinkman number Br**. Now we will add the **Graetz number Gz**:

With dimensionless quantities:

$$T^* = T/(T_1 - T_0) \quad y^* = y/H \quad x^* = x/L \quad u^* = u/V$$

The dimensionless form of Eq. (2.26) reads:

$$Gz \cdot u^* \frac{dT^*}{dx^*} = 1 \cdot \frac{d^2T^*}{dy^{*2}} + Br \cdot (du^*/dy^*)^2 \quad (1.32)$$

with $Gz = VH/a \cdot H/L$ and $a = \lambda/\rho c$

$$Br = \frac{1}{2} \mu V^2 / \lambda (T_1 - T_0) \quad (1.33)$$

These important dimensionless numbers will be used in Chapter 3, when and where we deal with Thermal Scaling of Extruders.

2. Modeling of continuous mixers

2.1 Summary

In many operations in polymer processing, such as polymer blending, devolatilisation, or incorporation of fillers in a polymeric matrix, continuous mixers are used; e.g., co-rotating twin-screw extruders (zwei schnecken kneter: ZSK), Buss co-kneaders, and Farrel Continuous Mixers, FCM. Theoretical analyses of these machines tend to emphasize the flow in complex geometries rather than generate results that can be directly used [1-5]. In this chapter¹, a simple model is developed for the hot melt closely intermeshing co-rotating twin-screw extruder, analogous to the analysis of the single-screw extruder carried out in 1922 and 1928 [6-7], as dealt with in Chapter 1 of this course on polymer melt extrusion and mixing processes. With this model, and more specifically with its extension to the complete non-isothermal, non-Newtonian situation, it is possible to understand the extrusion process and to calculate the energy, specific energy, and temperature rise during the process with respect not only to the viscosity of the melt, but also to the screw speed and screw geometry: location and number of transport elements, kneading sections and blisters, pitch, positive or negative, screw clearance, and flight width. To support the theoretical analysis, model experiments with a plexiglas-walled twin-screw extruder were performed, in addition to practical experiments with melts on small- and large-scale extruders, with very reasonable results. The Buss co-kneader has been analysed analogously².

2.2 Co- versus counter-rotating twin screw extruders

Twin-screw extruders may be divided into counter- and co-rotating types and into closely, partly, and non-intermeshing systems (8-10). Apart from the direction of rotation of the screws, they can be subdivided according to their transport mechanism: positive displacement or drag flow. This division can be made by investigating whether the channel is closed in the axial direction (by flight of the opposite screw) or in fact open (11-13).

Counter-rotating extruders can be constructed with smaller clearances from a geometrical point of view, and the closely intermeshing types are therefore often associated with positive displacement. In practice, this does not prove to be very realistic because, apart from the typical tetrahedron gap between the sides of the adherent screw flights and the necessary clearance between barrel and screws, the so-called calender gap between screw root and tip of the flight of the opposite screw is often rather large. This gap drags material (with two moving walls!) backward into the previous C-shaped chamber. Without this gap, plastification (or gelation) of, for instance, poly(vinylchloride) (PVC) would be impossible. PVC is rather

¹ Based on, and see for details: H.E.H. Meijer and P.H.M. Elemans, *The Modeling of Continuous Mixers. Part 1, The Corotating Twin-Screw Extruder*, Pol. Eng. Sci., **28**, 5 (1988), 275 – 290.

² P.H.M. Elemans and H.E.H. Meijer, *On the Modeling of Continuous Mixers. Part 2, The Cokneader*, Pol. Eng. Sci., **30**, 15 (1990), 893 – 904.

typically processed with this type of extruders because of its poor thermal stability combined with its very high viscosity. Reason for the high viscosity is not so much the polymer's molecular weight, but more caused by that the remaining ~1% crystallinity –the tiny crystals melt at around 260 °C where PVC degrades- act at the processing temperature of 190 °C as physical crosslink points of a network; therefore PVC is basically processed as a rubber. Moreover, given the high viscosity and poor thermal stability it is not allowed to heavily shear PVC and, therefore, external and internal plasticizers are added to the compound, yielding poor transport mechanism in drag extruders. The counter-rotating extruder is treated in detail in *Refs. 14 and 15* with the final result that the pumping characteristic, throughput versus pressure build-up, is rather easily obtained as the number of C-shaped chambers, becoming free per unit of time, multiplied by the volume of one chamber, minus the sum of all leakage flows. Even with small clearances, the backflow because of the leakage is in the order of half the positive displacement (depending on the pressure at the die).

Apart from some non-intermeshing types which are sometimes used for devolatilization [16] counter-rotating twin-screw extruders can in principle, given the importance of the calender gap, be treated as a continuous two- roll mill process. The analysis of the milling process can be found in any good textbook on polymer processing (17- 19).

Analogously, the FCM, Farrel Continuous Mixer, can be treated as an internal mixer fed by a non-intermeshing counter-rotating twin-screw extruder. Although numerous papers have been published on these mixers, especially with respect to rubber compounding, only a few are significant. Examples are the work by Noordermeer (20) whose emphasis is on the rubber, following the work originally done by Tokita and White (21,22), and the work by Manas *et al.* (23) who developed the first really interesting model on the dispersive mixing of carbon black in a rubber matrix, an analysis that can be easily extended to other processing equipment or to the mixing of polymer blends (24, 25). Further discussion of this subject is not in the scope of this chapter, which is confined to the modeling of the corotating twin-screw extruder.

In practice, co-rotating extruders also can be constructed with broad flights, as is sometimes done in the feed section, to solve problems with difficult-to-transport powders. However, their tetraheder gap is again from the geometrical point of view always much larger than the one in counter-rotating extruders. Moreover, they are constructed with closely intermeshing screws to promote the self-wiping and, as a consequence, the flights leave a completely open 8-shaped chamber. Therefore, the transport mechanism is drag flow. The analysis of the co-rotating twin-screw extruder can be found in Ref. 4, but as in *Refs. 14 and 15*, too much effort is paid to a detailed treatment of the complex geometry and the reader becomes easily lost. Rauwendaal (14) pays some attention to the modeling of co-rotating twin-screw extruders, but the analysis is incomplete and, therefore, of little practical use. Of course, the more important extruder manufacturers have developed their own computer programs to predict the performance of their extruders dependent on screw design, and to scale up the results from laboratory measurements to production size (26). But for reasons that are easily under-

stood, they do not always present their know-how to the competitors in the open literature.

Here, the co-rotating twin-screw extruder will be dealt with as a single-screw extruder using the theories developed in 1922 and 1928, as derived in Chapter 1. This is allowed with respect to the transport characteristics of the melt-filled sections because of the completely open channel.

2.3 Screw geometries

Different screw elements exist: single-, double-, or triple-flighted screws with different pitch, even with negative pitch, mixing and kneading elements. Screw configuration is extremely flexible, one of the major advantages of this kind of extruders, and can be fitted to the job. At present, mostly double-flighted screw elements are used because of the larger useful volume. Single-flighted screws are less popular. because mixing increases with the number of flights. *Figure (2.1)* shows 8 examples of different screw configurations that all have been used in different trials and applications in different laboratories.

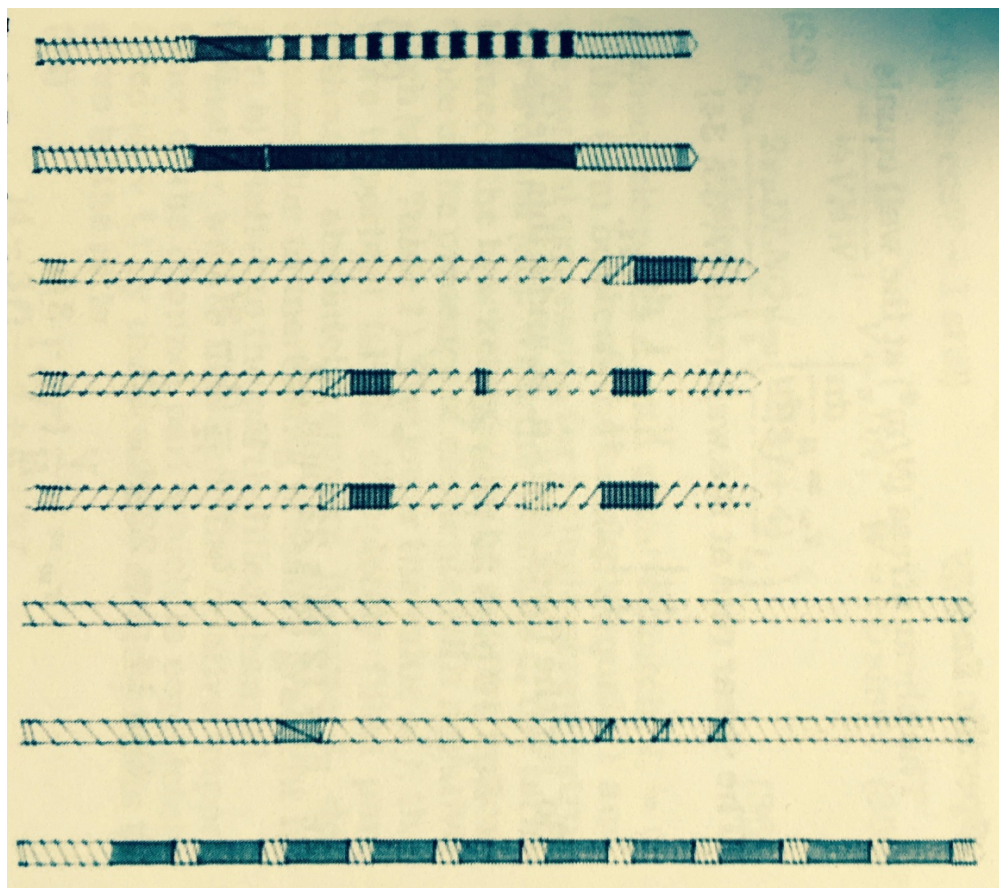


Figure 2.1 Eight different examples of the flexible screw design in co-rotating twin-screw extruders.

Although the maximum applicable torque on the screws has been recently (*we talk 1988*) doubled in the new series of extruders, the maximum torque is still relatively low in comparison with single- screw extruders and (conical) counter-rotating twin-screw extruders. This is inherent to the flexible screw design and self-wiping action.

Attention will be focused on the hot melt extruder, which in practice is used for devolatilization or is present after the melting section in each compounding extruder. Solids conveying, transition, and melting sections are difficult to analyze because no distinguished melting mechanism can be recognized as in single- screw extruders (27-30). Rather, a mixture of solids and melt exists as in the dissipative mix melting mechanism (31). Nevertheless, incorporation of the modeling of the melting section will be important because during compounding most of the limited torque is used in this stage of the process and sometimes even an important part of the dispersive mixing is already achieved here, because of the high viscosity (low temperature) of this mixture (32).

The most elementary screw geometry is given in *Figure (2.2)* and consists of a sequence of transport elements with positive pitch combined with an element with negative pitch. The principle of the analysis will be explained using this geometry. In the screw segment of *Figure (2.2)*, three functional parts can be distinguished: part *a*, partially filled having a degree of fill f ($0 < f < 1$); part *b*, completely filled, pressure generating; and part *c*, completely filled, pressure consuming.

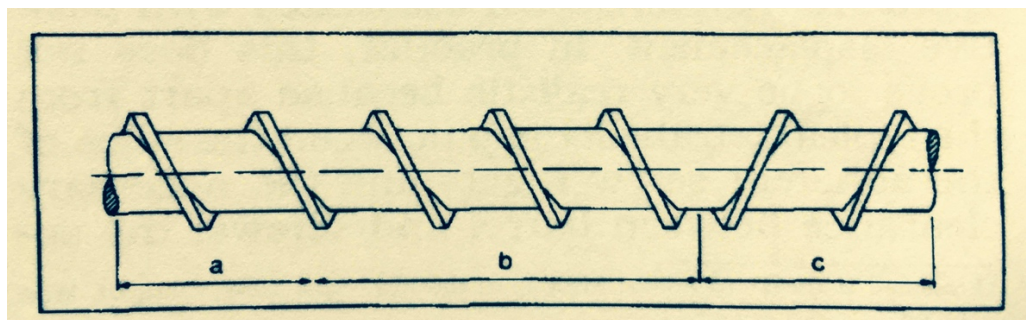


Figure 2.2 Elementary screw geometry of under-fed co-rotating twin-screw extruders. The counter-transporting element 'c' is used to fill the screw in element 'b', in order to create residence time.

In principle, every screw (some examples are given schematically in *Figure (2.1)*) can be thought to consist of parts *a*, *b*, and *c*. The reason is that a primary task of co-rotating twin-screw extruders is either to remove volatiles from the melt (water, solvents, monomers) or to add fillers (glass, chalk, talc, mica) via openings in the barrel. As a consequence, all co-rotating extruders must be underfed, which means that the throughput locally at least in the open barrel sections is only part of the maximum theoretical throughput. **(Correct metering**

of the individual components is often stated to be 80% of the compounding job). Subsequently the screws must be locally complete filled to allow operations, like melting and mixing, that require residence time. If partly filled screws would only consist of transporting elements, the residence time would be very short. Think about transport of a sphere in an empty screw. In every revolution of the screw, it transfers a distance D in axial direction. (Reason is that screws are generally “square”, meaning that the pitch angle ϕ is chosen such that $\tan\phi = 1/\pi$, see Figure (2.3)). In a screw rotating at 120 [rpm] the sphere travels an axial distance of $120D$ per minute. If the screw has a length of $L/D = 20$, the sphere needs 1/6 of a minute, thus 10 seconds, to reach the exit. This is the order of magnitude of the residence time if no pressure consuming screw elements would be present. In complete filled sections of the screw, with volume $V_f = L_f WH$ [m³] and metered throughput Q [m³/s], the residence time T_{res} [s] equals:

$$T_{res} = V_f / Q \quad (2.1)$$

which is generally considerably longer than 10 seconds and depends on the throughput metered and the screw geometry chosen. In conclusion: In continuous co-rotating twin-extrusion blisters, kneading blocks and counter-transporting elements are required to fill the screw to create residence time.

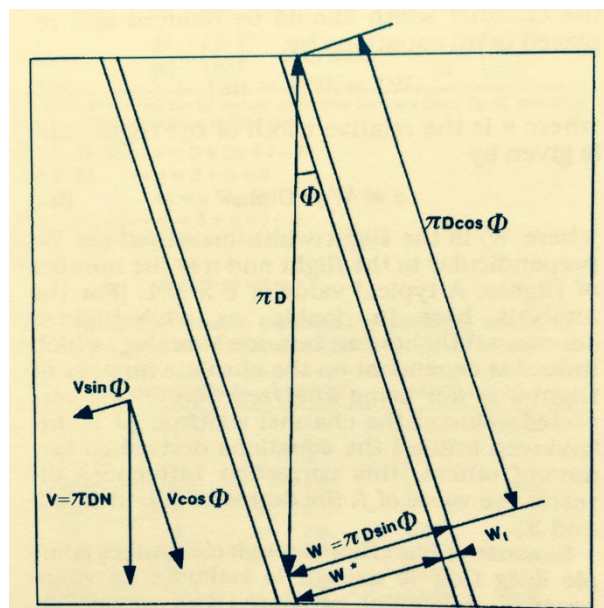


Figure 2.3 The unrolled screw channel. In square screws the pitch equals the diameter.

2.4 Analysis of simplified geometry

(Local) pressure gradients (following from throughput compared with theoretically maximum throughput) and lengths determine the relative dimensions of sections a , b and c . The screw is thought to be stationary and the barrel rotating in opposite direction as usual. Furthermore,

curvatures are neglected by either looking very locally or by unrolling the screw channel. In first approximation, the screw channel is thought to have a rectangular cross-sectional shape, with average height H and width W . The barrel wall moves with a velocity $V = \pi DN/60$ over the screw channel under an angle ϕ and drags the fluid towards the die. The analysis of the situation is completely analogous to the one treated in Chapter 1, with a drag flow $Q_d = \frac{1}{2}VHW$, and the only difference is that in continuous twin-screw extrusion the throughput Q is metered and prescribed to be only a fraction f of the maximum drag flow capacity:

$$Q = fQ_d \quad (2.2)$$

With f typically 0.5, see Figure (2.4):

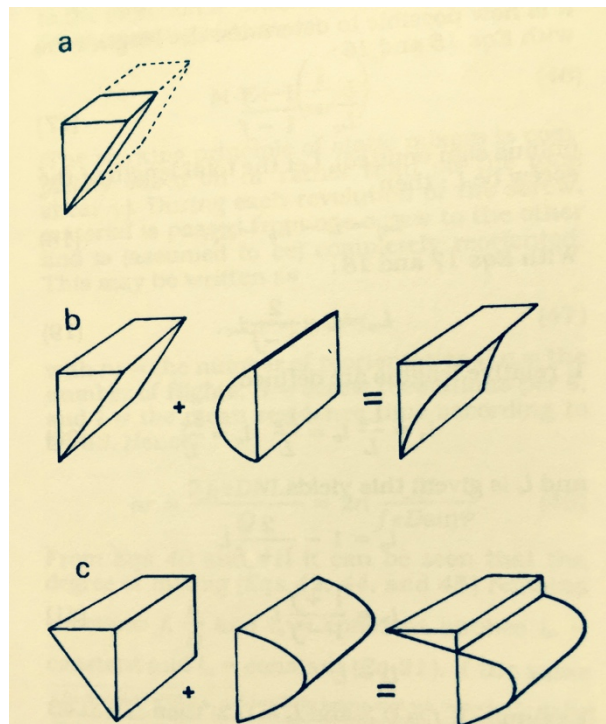


Figure 2.3 3D velocity profiles in sections a, b, and c of the extruder, see Figure (2.2). In all three sections, the throughput Q is the same and equals the metered throughput.

Always the (same) throughput Q is transported by drag Q_d and pressure Q_p flow:

$$Q = Q_d + Q_p \quad (2.3)$$

The filled parts b build up pressure and the pressure flow directs in negative transport direction and equals:

$$Q_p = -(1-f) Q_d \quad (2.4)$$

while in parts *c*, where the drag flow transports in negative direction, $Q_d = -\frac{1}{2}VHW$, the pressure flow, now in positive direction, must counteract this:

$$Q_p = (1+f) Q_d \quad (2.5)$$

The analysis follows that in Chapter 1. For instance with Eq. (1.1), Eqs (2.2) and (2.3) combined read:

$$f \frac{1}{2}VHW = \frac{1}{2}VHW + (WH^3/12\mu) * dP/dz \quad (2.6)$$

with *z* the channel direction, from which directly the local pressure gradients dP/dz can be determined. It follows:

$$dP/dz_b / dP/dz_c = -(1+f)/(1-f) \quad (2.7)$$

Given (i) the linear pressure gradients when working with Newtonian fluids, $dP/dz_b = \Delta P/L_b$ and $dP/dz_c = \Delta P/L_c$, (ii) the total extruder length *L* and (iii) -by screw design- the local relative length of the negative transport section *c*, $l_c = L_c/L$, the local lengths read:

$$l_a = 1-2/(1-f) l_c \quad l_b = (1+f)/(1-f) l_c \quad l_c = l_c \quad (2.8)$$

In conclusion: the working of the most simple version of a continuous co-rotating twin screw extruder, like shown in Figure (2.2), is uniquely determined by the screw design in terms of the relative length l_c of the counter transporting elements parts *c*, and the operating conditions in the form of the metered throughput that determines the degree of fill *f*.

Example: If $f = 0.3$ and $l_c = 0.2$, then $l_a = 0.43$ and $l_b = 0.37$.

2.5 Analysis of complex geometries

Apart from the counter-transporting, so-called 'left' elements '*c*', different kind of kneading blocks are used in co-rotating twin-screw extrusion. Interestingly, the cross-sections of all screw elements used are identical, and prescribed by the action of self-whipening where one screw during passage cleans the surface of the other. As a consequence, their cross-sectional mixing is identical. Terms like 'kneading blocks' are therefore somewhat misleading, since these elements do not so much more 'kneading' than transport elements but rather, as understood from the previous section, 2.4, they are present to fill the screws and create residence time. Basically kneading blocks consist of a number of identical discs, that are staggered such that their tops show a positive pitch (of 45°), a neutral pitch (no pitch angle) or a negative pitch (of -45°), see Figure 2.4. Therefore, they are called positive, neutral or negative kneading blocks. Sometimes in stead of 'positive' and 'negative', the terms 'right' and 'left' screw elements and kneading blocks are used, but this could be confusing since some extruder manufacturers prefer to let the screws rotate (as seen from the back) clockwise rather than the standard counter clock wise, see Figure (2.1). Kneading blocks basically only (and only slightly) differ in the direction of their drag flow, that is overall pretty weak because of the presence of all large leakage gaps in between the discs.

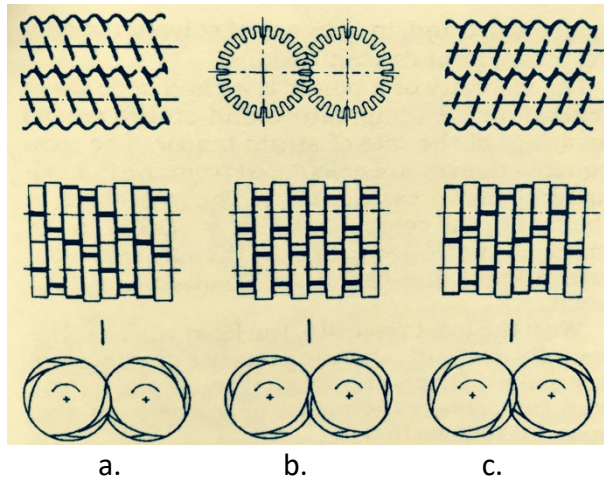


Figure 2.4 Positive (so-called 'right') (a), neutral (b) and negative (so-called 'left') (c) kneading blocks.

The analysis of complex screws based on combinations of these screw elements follows the same line as demonstrated in Chapter 1: we compute drag flow and pressure flow and sum up to obtain the throughput Q that is constant throughout the extruder. We thus construct the pump characteristics of all different elements. First Figure (2.5) shows the pump characteristics (here in throughput Q versus the linear pressure gradient $\Delta P/L$) of (1) a standard transporting screw element, a and b in (Figure 2.2), and (2) a counter-transporting screw element, c in (Figure 2.2).

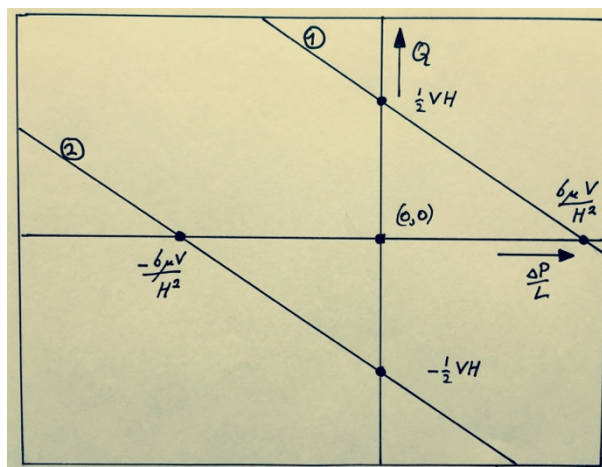


Figure 2.5 Pump characteristics in terms of throughput Q versus pressure gradient $\Delta P/L$ of (1) transporting screw element and (2) counter-transporting negative (left) screw element

Next Figure (2.6) adds the pump characteristics of a (3) positive-transporting, (4) neutral, and (5) negative-transporting kneading block. As is clear from these characteristics, the presence of large leakage flows in the big gaps between the staggered discs that constitute the kneading block make the pump characteristics very steep and only little pressure can be build up, or is

used. Apart from that, the influence of the precise staggering (positive, neutral or negative) is only marginal.

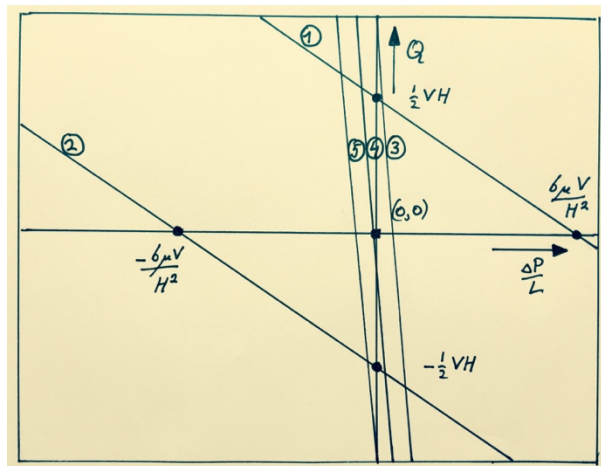


Figure 2.6 Pump characteristics of (1) transporting screw element, (2) counter-transporting screw element (3) transporting kneading block, (4) neutral kneading block, and (5) counter-transporting kneading block

Next we find the intersections of all pump characteristics with the horizontal line of constant, metered throughput Q in order to obtain the local pressure gradients $\Delta P/L$. They are required to predict filled-sections in e.g. the standard compounding screw of Figure (2.8). Of course $Q < Q_d$ since (i) for solids-fed extruders the density of the granular feedstock is lower than that of the melt, (ii) when melt is present and transported, we need partially filled channels at the second feed to make room for the fillers, and (iii) the same holds for the third barrel opening where room for gas and foaming is required.

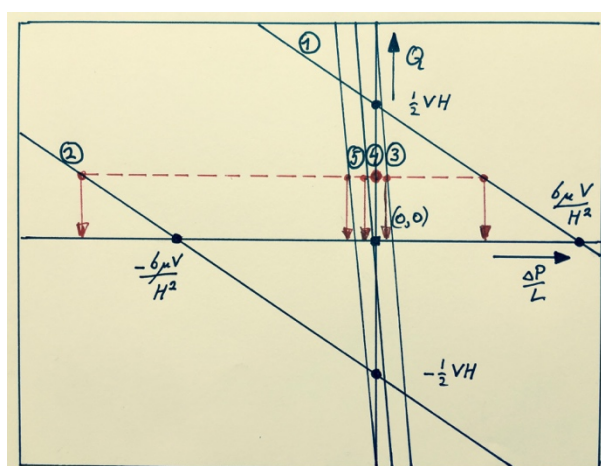


Figure 2.7 Given the constant metered throughput $Q < Q_d$ the local pressure gradients are found (red arrows) by intersecting the line Q is constant (red dashed line) with the 5 different pump characteristics.

From the red dashed line and the red arrows in *Figure (2.7)* we learn that for all kneading blocks the pressure gradients are close to zero. For transporting elements, we find the familiar value of a positive pressure gradient, for counter-transporting, negative, 'left', elements, large negative pressure gradients are required to overcome the drag in negative direction and to transport Q towards the die exit.

With the known pressure gradients, and the known local lengths of the different screw element sections, the pressure profile can be obtained, working from the right ($P=0$ at the die exit, and $P=0$ in the sections of the screw where holes in the barrel allow transport in- or out) to the left. Basically the procedure results in the, originally unknown, lengths ' a ' and ' b ' (see *Figure (2.2)*) of the screw. **Operating is safe as long as lengths ' a ' are positive.**

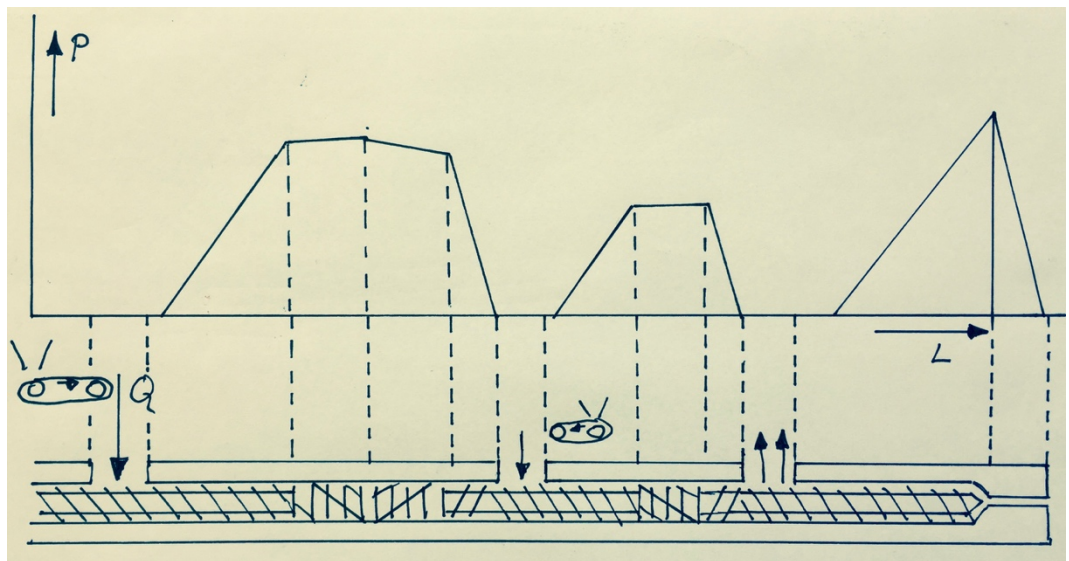


Figure 2.8 An standard compounding screw, with metered throughput left, melting section, addition of filler, mixing section and degassing section before the die exit. With the local pressure gradients just determined, the filled parts of the extruder can be determined graphically, working from right to left.

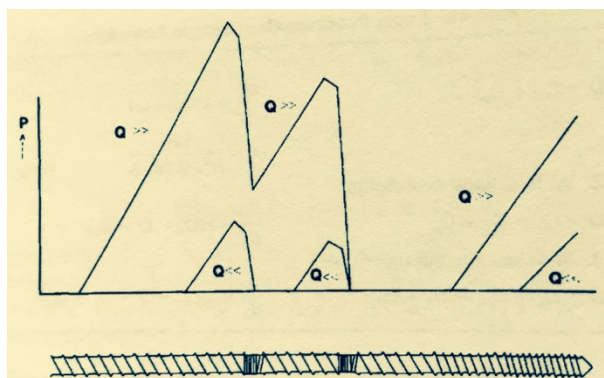


Figure 2.9 Like Figure (2.8) illustrating in a different screw configuration the dependence of filled lengths on the metered throughput Q .

Figure (2.9) illustrates that filled length of the screw strongly depend on the dosed throughput Q , of course relative to the maximum drag flow capacity Q_d that depends directly on e.g. screw speed N .

2.6 Torque, energy and specific energy

Since all pressure gradients are obtained, the local velocity profiles are known and, by differentiation and substituting $y = H$, the local wall shear stresses. Since the length of all screw parts is also obtained, the force and torque on the extruder barrel wall are directly computed. Given the screw speed, the energy required to run the extruder is known, and with the metered throughput we find the specific energy, E_{sp} . Since we know that extruders are viscosity independent pumps with a low efficiency, a large part of the driving energy is dissipated into heat. This causes the pumping fluid, usually a polymer melt, to increase in temperature. Consequently, the viscosity lowers, as does the energy and specific energy required. It is outside the scope of this introductory course to deal with all the details, that can be found in H.E.H. Meijer and P.H.M. Elemans, *The Modeling of Continuous Mixers. Part 1, The Corotating Twin-Screw Extruder*, Pol. Eng. Sci., **28**, 5 (1988), 275 – 290.

Here we only summarize the results, see Figures (2.10) and (2.11).

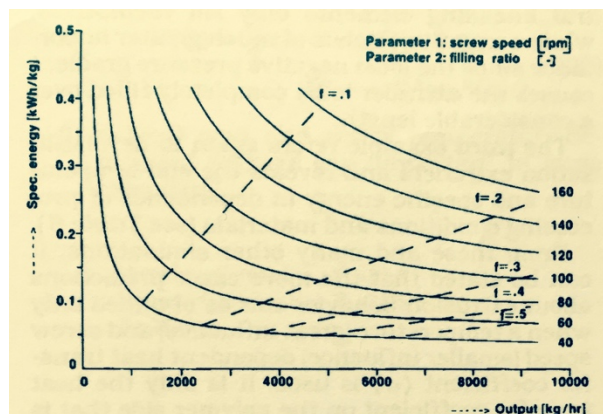


Figure 2.10 Specific energy E_{sp} as a function of metered throughput Q . Parameter is the screw speed N . Lines of constant degree of fill, f , are indicated with dashed lines. Isothermal case with a Newtonian fluid.

The specific energy that if it is too high might overheat the polymer melt decreases with decreasing screw speed and increasing throughput. Basically the degree of fill, f , should be maximized. In practise this means that the extruder should run at maximum available torque.

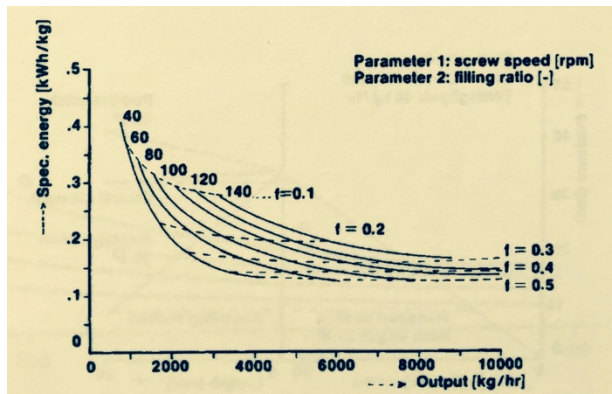


Figure 2.11 As Figure (2.10): Specific energy E_{sp} as a function of metered throughput Q , now for the non-isothermal case using a powerlaw model.

The results of the more precise non-isothermal, powerlaw calculations, *Figure (2.11)*, are qualitatively similar to those of the isothermal Newtonian case. The physical feed back: higher specific energy \rightarrow higher melt temperature \rightarrow lower viscosity \rightarrow lower specific energy more or less auto-regulates the system. All lines for different screw speeds lower and approach each other, the overall conclusion that maximizing the degree of fill, f , thus maximizing the torque, for low specific energy remains valid.

3. Scaling of continuous mixers

3.1 Definition of the scaling problem

Once experiments on small, laboratory, scale have been successful, the next question arises: how do we translate the results to the macro scale, and what do we precisely need in terms of equipment size, screw design and operating conditions. In order to answer these questions, simple scaling rules have been designed³, see also⁴. They distinguish different scaling strategies that give different answers. The most straightforward strategy is *geometrical scaling*, that is intuitively also the most direct one, and that keeps mixing in small and large machines identical. But this is only true if the extruders, on both scales, work fully adiabatic, i.e. no heat exchange with the barrel wall and surroundings exists. Usually this is not the case, and differences in heat exchange cause the temperature development to be not the same. The main cause of the problem is that the content of the screw scales with the diameter to the power 3, while the barrel surface scales with the power 2. If thermal issues are important, e.g. once heat exchange via the barrel wall is required in the melting process or when the melt need to be cooled in order to avoid to high melt temperatures, *thermal scaling* is required.

3.2 Governing equations

We first summarize the relevant equations derived so far in our modelling of extruders, see [Chapters 1 and 2](#), the set of Equations (3.1).

Throughput	$Q = \frac{1}{2}VH + (H^3/12\mu)*\Delta P/L$
Newtonian fluid	$\tau = \mu du/dy$
Wall velocity	$V = \pi D N/60$
Pressure flow in die	$Q = (h^3/12\mu)*\Delta P/l$
Torque	$T_o = \frac{1}{2} L_{ax} \pi D^2 (\mu V/H + \frac{1}{2} \Delta P H/L)$
Drossel ratio	$a = \Delta PH^2 / 6 \mu VL$
Channel width	$B = \pi D \sin \phi$
Throughput per channel width	$Q/B = \frac{1}{2} VH (1-a)$
Energy per channel width	$E/B = \mu V^2 L/H (1+3a)$
Specific energy	$E_{sp} = E/Q = 2\mu VL/H^2 \cdot (1+3a)/(1-a)$
Energy equation:	$u\rho c dT/dx = \lambda d^2T/dy^2 + \mu (du/dy)^2$
Dimensionless energy equation	$Gz \cdot u^* dT^*/dx^* = 1 \cdot d^2T^*/dy^2 + Br \cdot (du^*/dy^*)^2$
Dimensionless Graetz number	$Gz = VH/a \cdot H/L$ and $a = \lambda/\rho c$
Dimensionless Brinkman number	$Br = \frac{1}{2} \mu V^2/\lambda(T_1-T_0)$

³ P.H.M. Elemans, H.E.H. Meijer, *Scale-up of the Mixing Process in Continuous Mixers*, in *Mixing and Compounding of Polymers. Theory and Practice*. Eds. I. Manas Zloczower and Z. Tadmor. Hanser Publisher New York. Chapter 13, pp 457-470 (1993); (only in first edition).

⁴ H.E.H. Meijer and P.H.M. Elemans, *The Modeling of Continuous Mixers. Part 1, The Corotating Twin-Screw Extruder*, *Pol. Eng. Sci.*, **28**, 5 (1988), 275 – 290.

Next we greatly simplify this set, realizing that we only need to mutually compare results on the large, diameter D , extruder with those obtained on the small laboratory one with D_0 . Therefore, only ratio's of the two have to be compared with the advantage that all constants drop off. First we define the ratio's of the relevant parameters on the large (no index) and the small (index $_0$) extruder, like N/N_0 for the rotational screw speed ratio, and express them as a power of the ratio of their diameters, as the size determining parameter D/D_0 ; set of Equations (3.2):

Screw speed	N/N_0	=	$(D/D_0)^n$
Channel depth	H/H_0	=	$(D/D_0)^h$
Screw length	L/L_0	=	$(D/D_0)^l$
Throughput	Q/Q_0	=	$(D/D_0)^q$
Mean residence time	t/t_0	=	$(D/D_0)^t$
Shear rate	$\dot{\gamma}/\dot{\gamma}_0$	=	$(D/D_0)^g$
Total shear	$\dot{\gamma}_{tot}/\dot{\gamma}_{tot 0}$	=	$(D/D_0)^{gt}$
Torque	T_0/T_0	=	$(D/D_0)^t$
Energy	E/E_0	=	$(D/D_0)^e$
Specific energy	$E_{sp}/E_{sp 0}$	=	$(D/D_0)^{es}$
Graetz number	Gz/Gz_0	=	$(D/D_0)^{gz}$
Brinkman number	Br/Br_0	=	$(D/D_0)^{br}$
P* number	P^*/P^*_0	=	$(D/D_0)^{p^*}$
B* number	B^*/B^*_0	=	$(D/D_0)^{b^*}$

Next define the ratio's for throughput, shear rate, total shear, torque, energy, and specific energy. As an example for the throughput we find in Eq. (3.1):

$$Q = \frac{1}{2} V H (1-a) B, \text{ with } V = \pi D N / 60 \text{ and } B = \pi D \sin \phi \quad (3.3)$$

Thus

$$Q = \frac{1}{2} \pi^2 D^2 N H (1-a) \sin \phi / 60 \quad (3.4)$$

We decide to keep the pitch angle of the screw ϕ and the ratio a , the pressure flow to drag flow, the same in both extruders, thus $\phi = \phi_0$ and $a = a_0$. Then:

$$Q/Q_0 = D^2 N H / D_0^2 N_0 H_0 \quad (3.5)$$

Thus:

$$Q/Q_0 = (D/D_0)^2 \cdot (N/N_0) \cdot (H/H_0) \quad (3.6)$$

With help of Eq. (3.2) we rewrite Eq. (3.6) to obtain:

$$(D/D_0)^q = (D/D_0)^2 \cdot (D/D_0)^n \cdot (D/D_0)^h$$

From which the relation between the power coefficients is found:

$$q = 2 + n + h \quad (3.7)$$

Repeating the same procedure for the other expressions from Eq. (3.1), all relations between all different power coefficients are found, set of Equations (3.8):

<i>throughput</i>	q	=	$2 + n + h$		
<i>mean residence time</i>	t	=	$h + 1 + l - q$	=	$l - 1 - n$
<i>shear rate</i>	g	=	$n - h + 1$		
<i>total shear</i>	g_t	=	$g + t$	=	$l - h$
<i>torque</i>	t_o	=	$3 + n + l - h$		
<i>energy</i>	e	=	$3 + 2n + l - h$		
<i>specific energy</i>	es	=	$e - q$	=	$1 + n + l - 2h$

The temperature development in extruders is obtained from solving the energy equation with the proper boundary conditions. It was given in Eq. (3.1) in its dimensionless form:

$$Gz \cdot u^* dT^*/dx^* = 1 \cdot d^2T^*/dy^2 + Br \cdot (du^*/dy^*)^2 \quad (3.9)$$

The solution of the dimensionless equation Eq. (3.9) is always the same when using the same dimensionless numbers Gz and Br and boundary conditions. With:

$$Gz = VH/a \cdot H/L \text{ and } a = \lambda/\rho c$$

$$Br = \frac{1}{2} \mu V^2 / \lambda (T_1 - T_0)$$

we write:

$$Gz/Gz_0 = (VH^2/L)/(V_0H_0^2/L_0) \quad (3.10a)$$

$$Br/Br_0 = V^2/V_0^2 \quad (3.10b)$$

which, with $V = \pi D N/60$ and Eq. (3.2), yields:

$$(D/D_0)^{Gz} = (D/D_0)(D/D_0)^n(D/D_0)^{2h}(D/D_0)^{-l} \quad (3.11a)$$

$$(D/D_0)^{Br} = (D/D_0)^2(D/D_0)^{2n} \quad (3.11b)$$

thus

$$\text{Graetz} \quad gz = 1 + n + 2h - 1 \quad (3.12a)$$

$$\text{Brinkman} \quad br = 2 + 2n \quad (3.12b)$$

The energy equation (3.9) is valid for laminar flows as they occur in single screw and counter-rotating twin screw extruders. Given the excellent mixing in co-rotating twin-screw extruders, where every time that a screw wipes the other, a reorientation of the melt occurs resulting in exponential rather than linear mixing, a better heat balance is the one shown in *Figure (3.1)*.

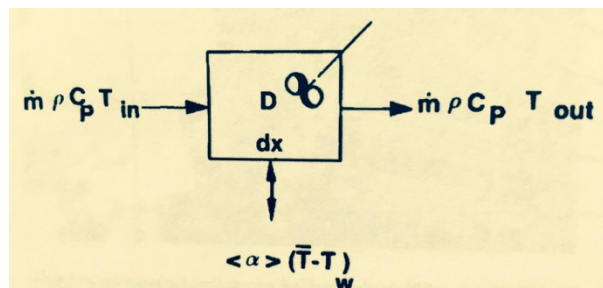


Figure 3.1 Local heat balance in well mixed flows.

Elaborating the heat balance results in the energy equation that is more simple since inside the flow because of good mixing we do not have to solve heat conduction and just can take T^{a*} as the average dimensionless temperature and u^{a*} as the average dimensionless velocity:

$$P^* \cdot u^{a*} dT^{a*}/dx^* = T^{a*} + B^* \cdot (du^{a*}/dy^*)^2 \quad (3.9)$$

With for the P^* and B^* numbers:

$$P^* = 1/\langle \alpha \rangle VH/L \quad (3.10a)$$

$$B^* = 1/\langle \alpha \rangle \mu V^2/H(T_1 - T_0) \quad (3.10b)$$

With $\langle \alpha \rangle$ the heat transfer coefficient. Defining its dimensionless form, the *Nusselt* number:

$$Nu = \langle \alpha \rangle L/\lambda, \quad (3.11)$$

the *Peclet* number $Pe = VH/a$, and aspect ratio $A_s = H/L$, we find:

$$P^* = Pe/Nu = Gz/Nu \cdot A_s \quad (3.12a)$$

$$B^* = Br \cdot A_s / Nu \quad (3.12b)$$

For scaling from extruder D_0 to D we keep the material parameters $a = \lambda/\rho c$ and the heat transfer conditions, *Nusselt* number, constant, and thus can write:

$$P^*/P_0^* = (VH/L)/(V_0H_0/L_0) \quad (3.13a)$$

$$B^*/B_0^* = V^2/V_0^2 \quad (3.13b)$$

which, with $V = \pi D N/60$, yields:

$$(D/D_0)^{p^*} = (D/D_0)(D/D_0)^n(D/D_0)^h(D/D_0)^{-l} \quad (3.14a)$$

$$(D/D_0)^{b^*} = (D/D_0)^2(D/D_0)^{2n} \quad (3.14b)$$

thus

$$P^* \quad \quad \quad p^* = 1 + n + h - l \quad (3.15a)$$

$$B^* \quad \quad \quad b^* = 2 + 2n - h \quad (3.15b)$$

With this result, all relations between the power coefficients of all relevant quantities are established. We can start scaling, following the two different strategies: geometrical and thermal scaling.

3.3 Geometrical scaling

Geometrical scaling is the most intuitive way of scaling. All geometrical parameters scale with the diameter. Thus with the second 2 lines of Eq. (3.2):

$$\begin{array}{lll} \text{Channel depth} & H/H_0 & = (D/D_0)^h \\ \text{Screw length} & L/L_0 & = (D/D_0)^l \end{array}$$

This scaling reads:

$$h = 1 \quad (3.16a)$$

$$l = 1 \quad (3.16b)$$

and, if we chose to operate both extruders with the same rotational speed, line 1 of Eq. (3.2):

$$n = 0 \quad (3.16c)$$

That is all.

And it demonstrates the ease of use of scaling rules, since substituting Eq. (3.16) in Eq. (3.2) yields the power coefficients of all other parameters, set of Equations (3.17):

<i>screw speed</i>	n	=	0
<i>extruder length</i>	l	=	1
<i>channel depth</i>	h	=	1
<i>throughput:</i>	q	=	3
<i>mean residence time</i>	t	=	0
<i>shear rate</i>	g	=	0
<i>total shear</i>	g_t	=	0
<i>torque</i>	t_o	=	3
<i>energy</i>	e	=	3
<i>specific energy</i>	es	=	0

For example, in a two-times larger extruder $D/D_0 = 2$ running at the same screw speed, diameter, channel depth and extruder length are twice as large. The volume is 2^3 thus eight times larger to give an eight times higher throughput, that requires the torque and driving energy (motor) to be also eight times larger. Mixing is identical, since shear rate, residence time, total shear and specific energy are the same in both extruders.

Eq. (3.17) explains why geometrical scaling is popular. However, substitution of Eq. (3.16) in Eq. (3.12) and Eq. (3.15) learns, for both laminar and well-mixed flows, that the power coefficients that determine the temperature development are not zero: set of Equations (3.18):

<i>laminar flows:</i>			
<i>Graetz:</i>	gz	=	1
<i>Brinkman</i>	br	=	2
<i>well-mixed flows:</i>			
P^* :	p^*	=	1
B^* :	b^*	=	1

The temperature development is therefore clearly different. This is due to the fact the the barrel surface, πDL , scales with D^2 while volume (and throughput and energy, thus dissipation) with D^3 . Small extruders tend to have relatively more heat exchanging barrel surface. So the barrel heat source during melting and heat sink during melt cooling are much more pronounced. Differences in temperature development may cause huge problems for example when the melting capacity is limited, like in grooved feed section plastificating single screw extruders, or when thermal degradation threatens the polymer quality in melt fed

degassing extruders in polymerization plants. In these cases, therefore, **thermal scaling must be considered that, however, does not keep the mixing the same.**

3.4 Thermal scaling

In order to arrive at the same temperature development in laminar flows, as present in plasticating single screw extruders and counter-rotating twin screw extruders, or in well-mixed flows, such as in the co-rotating twin-screw extruders, the dimensionless numbers Gz , Br , P^* and B^* , should stay the same, set of *Equations (3.19)*:

laminar flows:

$$\begin{array}{l} \text{Graetz:} \\ \text{Brinkman} \end{array} \quad \begin{array}{l} gz \\ br \end{array} = \begin{array}{l} 0 \\ 0 \end{array}$$

well-mixed flows:

$$\begin{array}{l} P^* \\ B^* \end{array} \quad \begin{array}{l} p^* \\ b^* \end{array} = \begin{array}{l} 0 \\ 0 \end{array}$$

3.4a Thermal scaling for laminar flows

First we consider laminar flows. Combining *Eqs. (3.19)* with *(3.12b)* yields:

$$\text{screw speed} \quad n = -1$$

The screw speed is disproportional to the diameter ratio; thus a twice as big extruder should run at only half the speed (the circumventor velocity is the same). This has huge consequences. Furthermore, we chose the extruder length proportional to the diameter:

$$l = 1$$

and from $n = -1$, $l = 1$, combined with *Eqs. (3.19)* and *(3.12a)* we get:

$$h = 0.5$$

The channel depth of a twice as big extruder should be only $\sqrt{2}$ times as large. Combining all results yields for thermal scaling in laminar flows, set of *Equations (3.20)*:

$$\begin{array}{l} \text{Graetz:} \\ \text{Brinkman} \end{array} \quad \begin{array}{l} gz \\ br \end{array} = \begin{array}{l} 0 \\ 0 \end{array}$$

screw speed	n	=	- 1
extruder length	l	=	1
channel depth	h	=	0.5
throughput:	q	=	1.5
mean residence time	t	=	1
shear rate	g	=	- 0.5
total shear	g_t	=	0.5
torque	t_o	=	2.5
energy	e	=	1.5
specific energy	es	=	0.5

These results are indeed applied in practice in the scaling of plasticating single-screw extruders foreseen with very efficient groove-bored feed sections that make the melting capacity the limiting factor.

The relatively low throughput on larger machines, $q = 1.5$, is also interesting from an economic price-performance point of view. An inspection of sales prices of single screw extruders learns that for the power coefficient in the price ratio: $pr/pr_o = (D/D_o)^{pr}$, we find:

$$price \quad pr = 1.7 \quad (3.21)$$

which implies that, to increase throughput, a row of smaller extruders is cheaper than one bigger extruder. (The disadvantage is, however, that all auxiliary equipment must also be multiplied, which probably is more expensive).

3.4b Thermal scaling for well-mixed flows

Next we consider well-mixed flows. Combining Eqs. (3.19) with (3.15a) and (3.15b) yields:

$$1 + n + h - l = 0 \quad \text{and} \quad 2 + 2n - h = 0$$

Now we can choose: geometrical scaling of the extruder length, $l = 1$, or of the channel depth, $h = 1$. The last is practice in co-rotating twin-screw extruders, because of the self-whipening action required.

3.4b₁ First choice: $l = 1$

with	$l = 1$		
we find from Eq. (3.15b)	$n = - h$		
and from Eq. (3.15a)	$h = 2/3$	thus	$n = - 2/3$

Combining all results yields for thermal scaling in well-mixed flows, set of Equations (3.22):

P^*	p^*	=	0
B^*	b^*	=	0
<i>screw speed</i>	n	=	- 2/3
<i>extruder length</i>	l	=	1
<i>channel depth</i>	h	=	2/3
<i>throughput:</i>	q	=	2
<i>mean residence time</i>	t	=	2/3
<i>shear rate</i>	g	=	- 1/3
<i>total shear</i>	g_t	=	1/3
<i>torque</i>	t_o	=	2 + 2/3
<i>energy</i>	e	=	2
<i>specific energy</i>	es	=	0

3.4b₂ Second choice: $h = 1$

This is the case in co-rotating self-whipping twin-screw extruders.

With	$h = 1$
we find from Eq. (3.15b)	$n = - 0.5$
and from Eq. (3.15a)	$l = 1.5$

The screw speed is disproportional to the square root of the diameter ratio; the length on larger extruders is more than proportional larger. This also holds for the local length, like the size of kneading blocks. Combining all results yields for thermal scaling in well-mixed flows, set of Equations (3.23):

P^*	p^*	=	0
B^*	b^*	=	0
<i>screw speed</i>	n	=	- 0.5
<i>extruder length</i>	l	=	1.5
<i>channel depth</i>	h	=	1
<i>throughput:</i>	q	=	2.5
<i>mean residence time</i>	t	=	1
<i>shear rate</i>	g	=	- 0.5
<i>total shear</i>	g_t	=	0.5
<i>torque</i>	t_o	=	3
<i>energy</i>	e	=	2.5
<i>specific energy</i>	es	=	0

This final set of scale up rules shows, especially by the power coefficient for the throughput: $q = 2.5$, that twin screw extruders scale up well, but that for similar temperature development in both extruders, $p^* = b^* = 0$, the screw speed on the larger extruder should be somewhat lower, $n = -0.5$, which is OK for screw wear, further that all kneading blocks and counter-transporting elements should be relatively longer, $l = 1.5$, and finally that shear rate is somewhat lower, the residence time longer, resulting in more total shear.

4. Mixing^{5,6}

4.1 Distributive versus dispersive mixing

In polymer technology, two main routes can be discerned for the attainment of specific material properties that homopolymers often cannot accomplish (e.g., a high notched impact strength combined with a reasonable modulus and continuous use temperature necessary for engineering applications of polymers). One way is to blend or modify polymers in the reactor (in situ), as in the case of (block) copolymerization of, for example, polyurethanes (PUR), styrene-butadiene-styrene (SBS) block copolymers, reactor modified polypropylene (RMPP), high impact polystyrene (HIPS), and acrylonitrile-butadiene-styrene (ABS). The other way is the (extrusion) melt blending of different existing (homo)polymers. The versatility of melt blending techniques offers some advantages over the more traditional reactor modification. In addition, in reactive extrusion, in situ blending is promoted by specific reactions at the interface. Since most polymer combinations of interest are thermodynamically immiscible on a molecular scale, a specific microstructure of the separate phases results from the melt blending process; this morphology partly determines the final properties of the blend. Figure 3.1 gives some examples of such morphologies for the model system polystyrene (PS)/high density polyethylene (HDPE) [1].

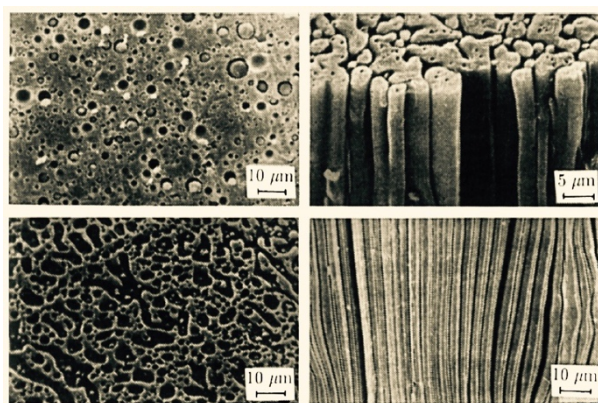


Figure 4.1 Examples of spherical, rod-like, sheet, and co-continuous morphologies in an incompatible blend of PS-HDPE.

At the end of the melt blending process the morphology, which is not necessarily in an equilibrium state, is frozen-in in the solid state. In a subsequent processing step, such as injection molding or film blowing, the morphology achieved may be altered as a result of the typical processing conditions there. Since the resulting morphology depends on the processing technique and conditions, the volume fractions and viscosity ratio of the polymers, the melt elasticity, and, most important, the time of mixing, it is of great concern to model

⁵ Based on: H.E.H. Meijer, J.M.H. Janssen, P.D. Anderson, *Mixing of immiscible liquids*, in *Mixing and Compounding of Polymers: Theory and Practice*; Editors: Ica Manas-Zloczower, 41-177, Hanser Publications, Book Chapter, ISBN 978-1569904244 (2009)

⁶ and: Han E.H. Meijer, Mrityunjay K. Singh, Patrick D. Anderson, *On the performance of static mixers: A quantitative comparison*, *Progr. Polym. Sci*, 37, (2012) 1333 – 1349.

the mixing process in a principally transient approach. However, since polymer blending involves complex, nonisothermal, non-Newtonian, time-dependent flows, direct research on industrial compounding equipment generally yields compound- and machine-limited results that might be useful for the specific problem under investigation but are not conclusive in a more general sense. As a consequence, most of the fundamental research on the mixing of immiscible liquids has been focused on idealized systems: using single drops of Newtonian model liquids in well-defined flow fields at room temperature. The results of this research generally are represented in dimensionless form and are scaled to practical processes in the areas of, for example, polymer blending and food technology.

In the mixing of immiscible liquids, the minor component is generally present as the dispersed phase (drops or filaments) in a continuous phase of the major component. An elementary step in the mixing process is the deformation of dispersed drops in the flow field, yielding an increase in the interfacial area between the two components accompanied by a decrease in local dimensions perpendicular to the flow direction: the striation thickness. Either the interfacial area or the striation thickness can be used as a measure for the quality of mixing. Deformation of drops is promoted by the shear stress τ exerted on the drops by the flow field and counteracted by the interfacial stress σ/R (with σ the interfacial tension and R the local radius) minimizing the surface to volume ratio, thus tending to a spherical shape. The ratio between these two stresses is called the capillary number Ca :

$$Ca = \tau R / \sigma \quad (4.1)$$

If the capillary number exceeds a critical value Ca_{crit} , the viscous shear stress overrules the interfacial stress, no stable equilibrium drop shape exists and the drop is extended and finally breaks up into smaller droplets. If $Ca < Ca_{crit}$, the interfacial stress competes with the shear stress and the drop will deform only slightly in the flow field, yielding a stable drop shape. Taylor [3, 4] was the first theoretically and experimentally, to investigate the critical conditions for breakup of dispersed drops.

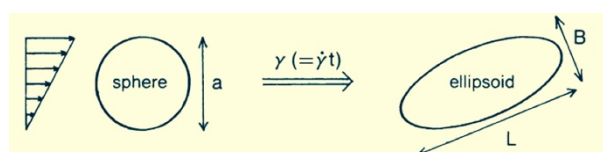


Figure 4.2 Deformation of an originally spherical drop in a steady shear flow into an ellips.

Taylor originally attempted to predict the viscosity of an emulsion, a liquid containing deformable drops of another (immiscible) liquid, via an extension of Einsteins [5] relation for the viscosity of a suspension, a liquid containing rigid spheres:

$$\eta = \eta_0 (1 + 2.5 \varphi) \quad (4.2)$$

with φ the volume fraction of rigid spheres and η_0 the viscosity of the surrounding liquid. Via a calculation of the flow inside and around a dispersed liquid drop, Taylor [3] derived the expression:

$$\eta = \eta_0 [1 + 2.5 \varphi (p + 2/5)/(p + 1)] \quad (4.3)$$

with

$$p = \eta_d / \eta_c \quad (4.4)$$

the viscosity ratio between the dispersed and the continuous (matrix) phase, which for $p \rightarrow \infty$ renders Einsteins original result. Einsteins goal was not so much to initiate the dispersion rheology but to obtain, from viscosity measurements in a dilute solution, quantitative information on the radius of gyration of molecules. Similarly, Taylor did not intend to begin the modeling of dispersive mixing. To verify his assumption that the drop would stay almost spherical, he had to investigate the circumstances under which a drop would severely deform and break up. The results of this research, the genuine start of the modeling of dispersive mixing, were published in 1934 [4].

Taylor found that in simple shear flow, a dispersed drop with viscosity ratio $p = 1$ becomes unstable and breaks up if $Ca > 0.5$, thus Ca_{crit} is of the order unity. Apparently, breakup occurs when both competitive stresses (τ and σ/R) are of the same order of magnitude. Ca_{crit} depends on die type of flow, simple shear versus elongational flow, and on the viscosity ratio p , as demonstrated later. Also, the rate of drop deformation and the time to breakup strongly depend on p . All microrheological processes generally occur faster for drops of low viscosity in a highly viscous continuous phase ($p < 1$) than in the opposite case ($p > 1$).

A useful subdivision of the mixing process can be based on the value of the (local) capillary number, which continuously decreases during the process, as a result of the decrease of the typical length scale (in polymer blending roughly from 1 mm to 1 μ m):

1. Distributive mixing when $Ca > Ca_{crit}$ (large dispersed domains, passive interfaces); drops are extended affinely with the matrix but do not develop capillary waves leading to breakup, since the interfacial stress is overruled by the shear stress.
2. Dispersive mixing when $Ca \cong Ca_{crit}$ (locally small radii of curvature, active interfaces); σ/R competes with τ and causes disturbances at the interface to grow, leading to breakup into smaller droplets and thus to a finer dispersion.

Although in reality distributive and dispersive mixing do not occur separately in a mixing device, this distinction is useful for a better understanding of the mixing process. Apart from a tendency toward finer morphologies resulting from distributive and dispersive mixing, a coarsening of the morphology may occur during mixing due to coalescence of the dispersed droplets. As is indicated later coalescence preferentially takes place at almost quiescent

regions of the flow, in contrast to the two mixing mechanisms described above. The sections that follow discuss distributive mixing, dispersive mixing, and coalescence.

4.2 Distributive mixing; $Ca \gg Ca_{crit}$

Some attention has been given to lamellar starting morphologies for the mixing process (see, e.g., [6]). These stratified structures originate from the melting process of polymers in an extruder, characterized by drag removal. Sheets of the dispersed phase become unstable and break up into threads, which then may break up into drops. Here, however, a drop in matrix structure, with the drop size of the same order of magnitude as the granular polymeric feedstock (~ 1 mm), is considered to be a typical starting morphology. This drop size might be considered to be an upper bound in terms of the characteristic length scale. For immiscible polymer melts, an order of magnitude estimate of the local capillary number yields:

$$\tau = \eta_c \cdot \dot{\gamma}_{dot} = 10^2 \cdot 10^2 = 10^4 \text{ Pa}$$

and

$$\sigma / R = 10^{-2} \cdot 10^{-3} = 10 \text{ Pa}$$

thus:

$$Ca = \eta_c \cdot \dot{\gamma}_{dot} \cdot R / \sigma = 10^3 \tag{4.5}$$

where τ is shear stress [Pa], η_c the viscosity of the continuous phase [Pa.s], $\dot{\gamma}_{dot}$ the shear rate [s^{-1}], σ the interfacial tension [N/m], and R is drop radius [m]. Note that in Eq. (4.5) the Newtonian constitutive equation is substituted; our knowledge of the mixing process is largely limited to the mixing of Newtonian liquids. From Eq. (4.5) it follows that $Ca \gg Ca_{crit}$, since $Ca_{crit} \approx 1$. Consequently, the interfacial stress (σ/R) is overruled by the deforming shear stress and the (millimeter sized) drops deform affinely with the matrix (i.e., distributive mixing with passive interfaces). Note that for miscible liquids (no interfacial tension), distributive mixing is the only process of interest (apart, of course, from diffusion).

4.2a Linear versus exponential mixing

Stirring during processing results in linear mixing where the interface length increases linearly with total shear or total deformation. A combination of stretching, folding, and reorienting can, however, change the efficiency of the distributive mixing process from a linear dependence of the total shear into an exponential dependence. The principle of this “stretching and folding” mechanism is depicted schematically in Figure 4.3.

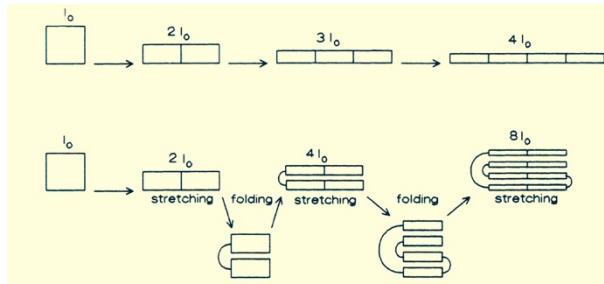


Figure 4.3 Stretching and folding during distributive mixing; the material is folded after every extension equal to the initial length l_0 (baker's transformation)

This transformation, resulting in the exponential way of mixing, is familiar to everybody who cooks. It is called the baker's transformation, named after the way dough is mixed by repeatedly rolling (which is a stretching operation) and folding.

In the past, when the maximum attainable temperature in ovens (ca. 1100 °C) was below the melting point of iron (ca. 1500 °C), iron could be separated from the ore only because the diffusion of carbon from the cokes in the furnace caused a depression in melting temperature. The result was cast iron with inferior mechanical properties. Upgrading to steel proved to be possible via oxidative removal of the extra carbon from the iron by forging. During forging, the iron is heated, hammered (which is stretching), folded, heated again, and so on. In this way, the striation thickness, which is the typical distance for diffusion of oxygen and carbon dioxide, is efficiently decreased, while the surface area is increased. That good steel required 5000 repetitions of this baker's transformation apparently has been known for a long time [7, 8].

4.2b Couette flow

Ng and Erwin [9] performed experiments using polymers to illustrate the efficiency of the baker's transformation in a Couette flow. By alternating black and white strokes of the same polymer in the gap between two concentric rotors (Figure 4.4) and, after melting, rotating one of the cylinders over a total angle γ_{tot} , mixing can be visualized. Quantitatively, mixing efficiency can be measured and calculated with the striation thickness, the total number of layers or the total interfacial area A :

$$A / A_0 \approx \gamma_{tot} \quad (4.6)$$

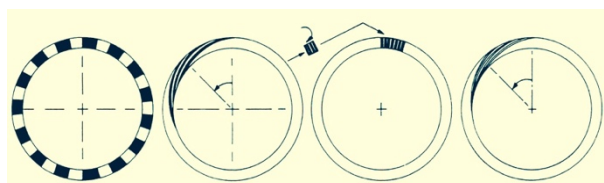


Figure 4.4 Exponential mixing in a Couette device. From left to right we find: (a) starting configuration, (b) shearing, (c) stop, cool, cut, reorient, and reheat, (d) shearing.

By dividing the total shear γ_{tot} in n equal intervals and reorienting the flow, once a shear of γ_{tot}/n has been reached, (this division can be achieved perfectly by cutting the ring into square pieces and rotating each individual piece over 90°) the interfacial area increases exponentially with shear:

$$A / A_0 \approx (\gamma_{tot} / n)^n \quad (4.7)$$

Distributive mixing can be summarized as affine deformation, with no influence of the interfacial tension (passive interfaces); stretching, with equivalency of shear rate and time, since only the total shear is important; and folding and reorienting, which yields the exponential mixing coefficient n .

4.2c Cavity flow

A systematic approach to the modeling of distributive mixing, valid in general three dimensional flows, is attributed to Ottino's group, which published a multitude of relevant papers on this subject. Of special interest and great didactic value is their numerical and experimental work on periodic (chaotic) flows in two-dimensional geometries (see, e.g., [34, 35]). An example is shown in *Figures (4.5) and (4.6)*. We will analyze Ottino's cavity flow here in some detail, especially because its simplicity and accessibility represent the best didactic tools available today, at least if we want to learn about the basics of mixing.

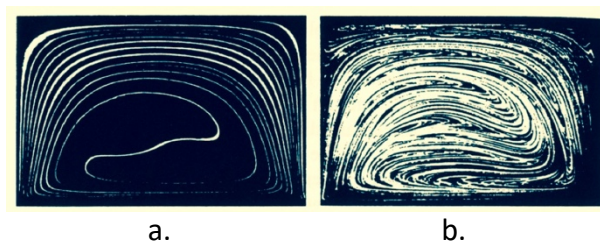


Figure 4.6 Comparison of (a) continuous and (b) discontinuous movement of the cavity walls; the total displacement of the walls is equal in both cases (from [36])

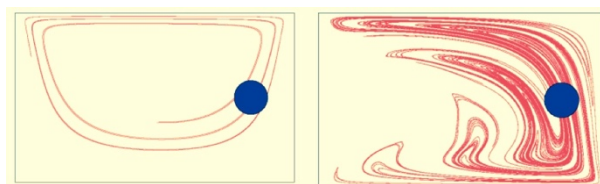


Figure 4.7 Adaptive front tracking results [38]. Comparison of (a) continuous and (b) discontinuous movement of the cavity walls; the total displacement of the walls is equal in both cases. The blue point represents size and original position of the stretched red blob

The top and bottom wall of the cavity, a rectangular duct, can be translated independently and periodically. The resulting flow patterns are visualized with two fluorescent tracer drops.

No interfacial tension is present between the tracer drops and the continuous phase, so only distributive mixing is studied. In the example of *Figures (4.8) and (4.9)*, one of the blobs (the red one) is stretched, folded, and transferred back to its initial position before the periodic movement is repeated, thus undergoing efficient mixing. The second blob (blue), however, is only rotated and convected, without any significant deformation. It moves inside a dead zone, called a regular island. The presence or absence of those important zones in general flows can be analyzed by different methods, the so-called dynamical tools. They include periodic point analyses, Poincaré sections, adaptive front tracking, and Mapping Method analyses, see e.g. *Figure (4.10)*.

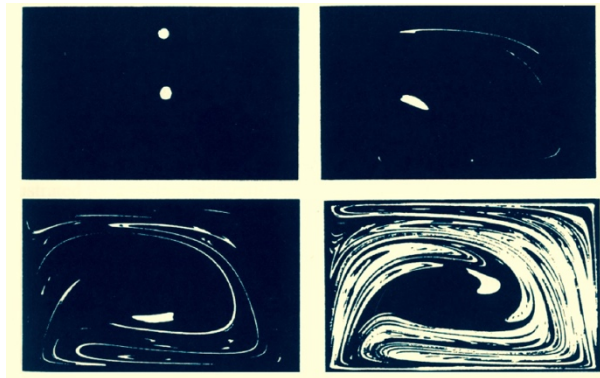


Figure 4.8 Distributive mixing in a cavity flow; top and bottom wall are translated periodically (from [35]).

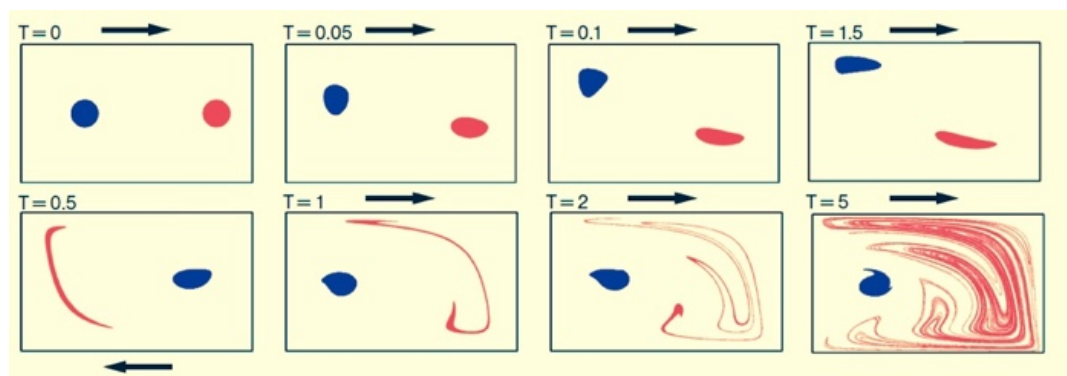


Figure 4.9 Distributive mixing in a cavity flow; top and bottom wall are translated periodically. The red blob is positioned in a first order hyperbolic periodic point, the blue blob in a first order elliptic periodic point. We follow the first period in detail ($T = 0$ to $T = 1$), then we jump to period 2 and 5.

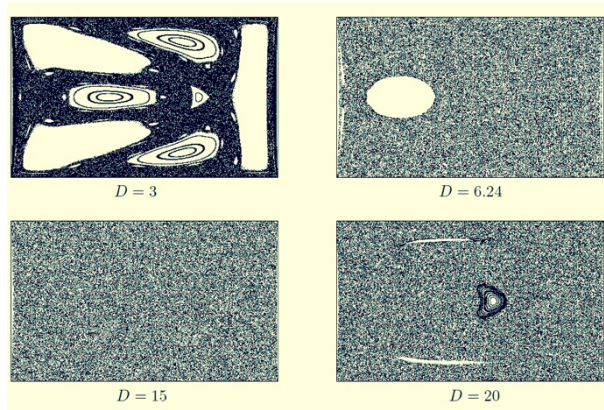


Figure 4.10 Poincaré sections of the cavity flow with different dimensionless wall displacements D . The example of top right, with $D = 6.24$, represents the experiments from Figure (4.8) and the simulations (4.9).

Next we apply mapping to study different flow protocols, see Figure (4.11). We compare the simple, top only movement flow (protocol A: $TTTTTTTTTTTTTTTT$), which yields poor closed streamlines and linear, bad mixing, with chaotic advection flows such as (protocol B: $TBTBTBTBTBTBTBTB$), the top-bottom protocol with crossing streamlines and exponential mixing, the symmetry breaking protocol (protocol D: $TBBTBTBBTBTBBT$), and the reverse protocol (protocol E: $TB-T-BTB-T-BTB-T-B$). Here TB stands for clock wise motion of top and bottom walls, respectively, and $-T-B$ stands for counter clock wise motion of the walls.

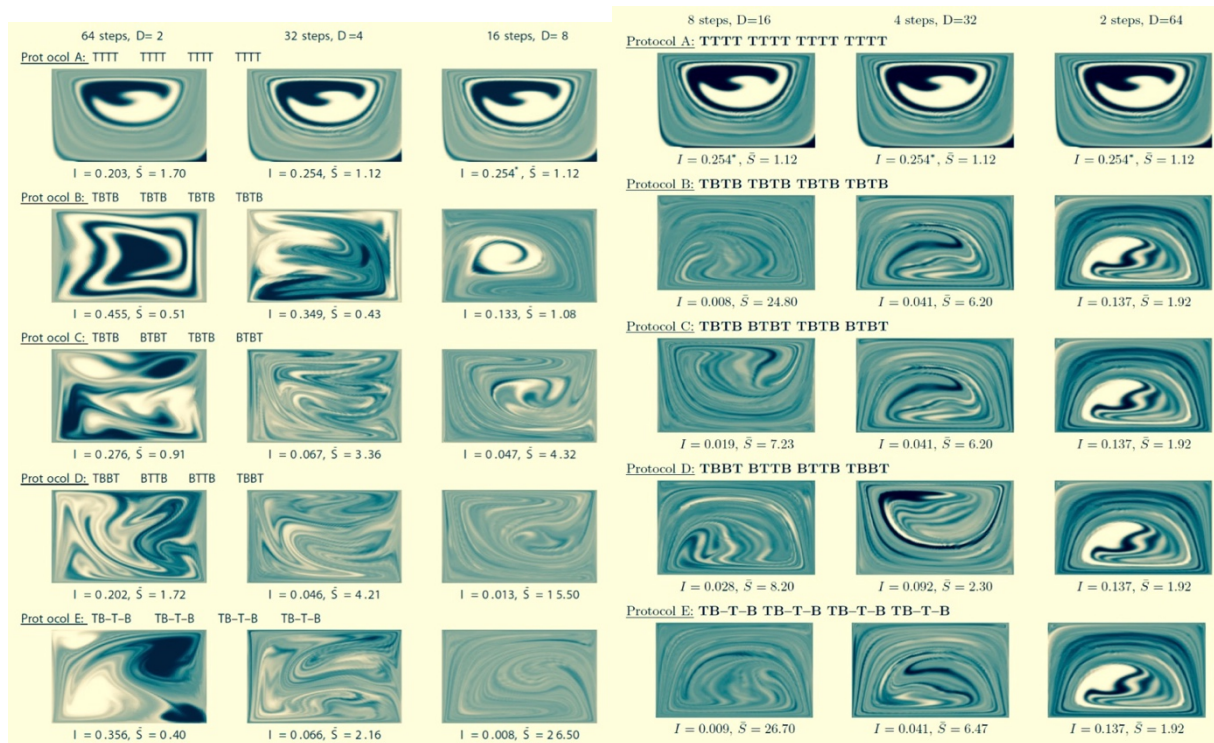


Figure 4.11 Comparing protocols and combinations of # steps and wall displacements D .

In all computations, the total wall displacement is kept constant at 128. Different numbers of steps are taken for different wall displacements (64 steps of $D = 2$; 32 steps of $D = 4$ and 16 steps of $D = 8$). Apparently, larger wall displacements provide better mixing in all protocols and the symmetry breaking protocol (D) together with the inverse protocol (E) seems superior to the standard TB protocol. This is investigated in more detail.

Mixing quality is expressed in the area-averaged intensity of segregation I . It changes from the value 1: no mixing to 0: perfect mixing. From the *Figure (4.11)* and values of I in that figure, it is clear that neither a large number of small steps, with little stretching in every step, nor a few steps with large stretching, gives optimal results. Differences between the protocols are found, but are non conclusive.

Therefore, an even more detailed analysis is needed and was performed, using 100.000 of computations with little steps in-between and the results are shown in *Figure (4.12)* for the standard $TBTB$ protocol A. A hyperbolic line in the figure represents mixing with equal energy input. The spiky appearance of the results illustrates the appearance and disappearance of islands, depending on the details of the operation expressed in different values of wall displacement D , as demonstrated in the snap shots at the border of the figure.

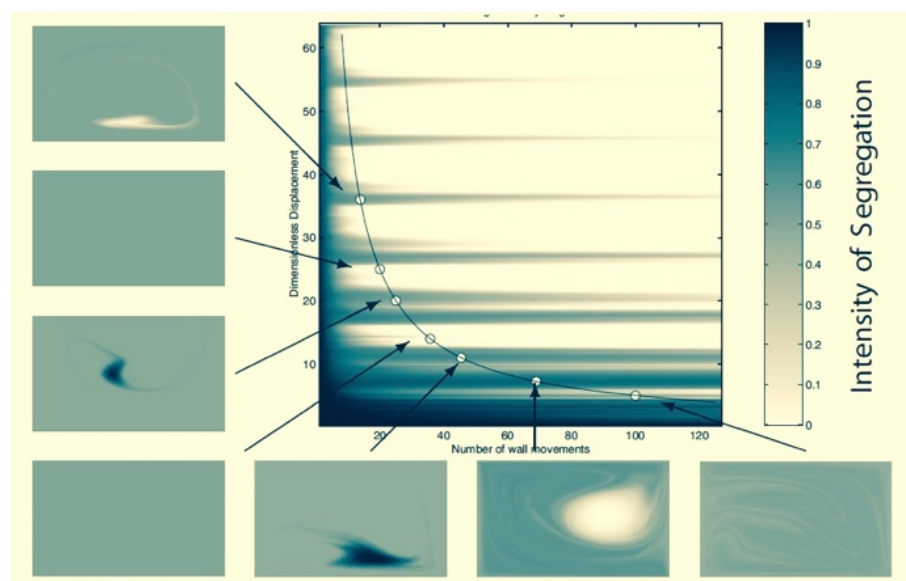


Figure 4.11 Final optimization of how to operate the lid-driven cavity using the standard protocol A ($TBTBTBTBTBTB$). Plotted is the area-averaged intensity of segregation I , with values from 1 (black, no mixing) to 0 (white, perfect mixing) for different wall displacements D (vertical axis) and number of wall movements N (horizontal axis) [18].

4.3 Static mixers

A perfect illustration of the application of the efficient baker's transformation in practical mixing is realized in almost all well-designed static mixers. The working principle of a static mixer is based on the stretching and folding mechanism illustrated in *Figure (4.5)*. Three major steps can be distinguished: stretching, cutting, and stacking. The last two steps have the same function as the folding in *Figure (4.3)*.

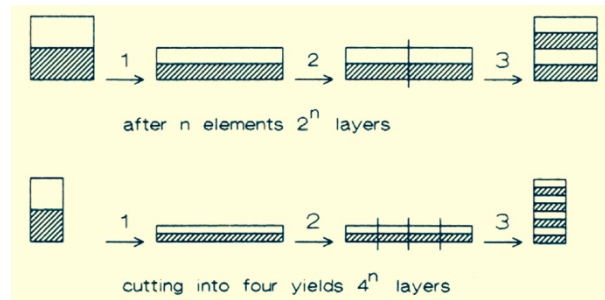


Figure 4.5 Stretching, cutting, stacking.

4.3a Kenics mixer

The Kenics static mixer, (*Figure (4.6)*), is industrially often used, probably because it adds function (mixing) to connecting tubes that are present anyway in technical processes to transport fluids. The elements inside the tube resemble platelets twisted 180° , like butterfly ties, with each successive element, again, rotated over 90° .

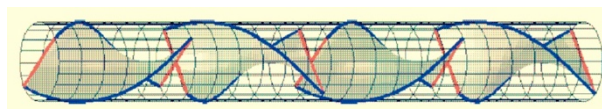


Figure 4.6 Kenics static mixer with alternating L-R, left-right turning elements

The working principle is shown in *Figures (4.7)* and *(4.8)*. Stretching of an interface between a white and a black fluid is caused by the rotation of the blades that make a secondary flow increase the cross-sectional interface typically from $0.5D$ to $1D$, with D the tube diameter. Cutting and stacking is cleverly realized by placing the next element under 90° .

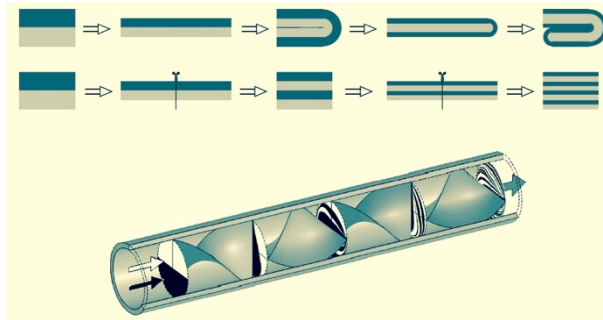


Figure 4.7 Mixing inside the Kenics static mixer is based on stretching, cutting, stacking.

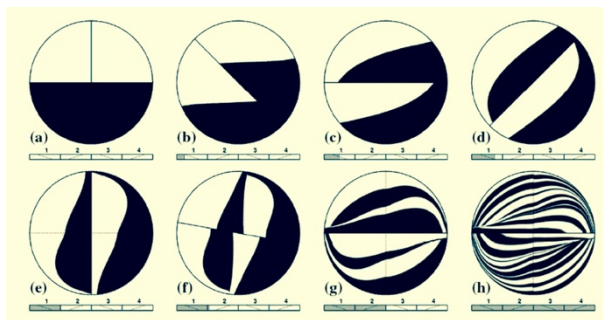


Figure 4.8 Interface creation inside the Kenics static mixer in the first element (a – e), in the second element (f - g) and after 4 elements (h).

If the platelets are thought to be straight, while the relative motion between wall and platelets, during the passage of the flow, is kept the same by adding an imaginary rotation of the barrel wall over the very same 180° , we arrive at the so-called partitioned pipe mixer [21], with roughly the same performance, although clear differences remain.

4.3b SMX mixer

A complex but, given its efficiency, frequently used static mixers is the SMX mixer (Static Mixer based on cross X plates), as at present produced by Sulzer. The interior parts look like crossing screens made out of parallel strips forming distinct elements that are consistently rotated, with alteration, over 90° , see *Figure (4.9)*. Some years ago, Sulzer produced an illustrative movie on its working principle by allowing a Lagrangian view of the flow inside. They fed two streams of colored white and red epoxies in the mixer, let the material react and consequently sliced through the resulting system, allowing to create a movie where the observer travels with the material through the mixer. *Figure (4.10)* shows some snapshots of the movie. Basically, the working principle can be explained as follows: If two horizontally crossed forks (or alternatively crossed fingers of your hands) are positioned on both sides of a vertical interface between a white and a red fluid, a line with length D of the channel diameter, and subsequently moved perpendicular to that interface to the other side of the channel, the

interface is distorted and stretched by folding between the teeth of the forks (or your fingers). A serpentine shaped interface line results with a length of $8D$ if forks with 4 teeth (or 4 fingers – thumbs are too small) are used. Now it becomes clear why the next element should be rotated over 90° . The teeth of the forks (or the fingers) reached the opposite side of the cross section of the channel. No more stretching of the interface is possible. The 90° rotation reorients the flow direction, again to be perpendicular to the – now 8 horizontal – interfaces formed in the first element. The crossing forks now fold $8D$ interfaces together to become $8 \times 8D$ in length after reaching the bottom and top side of the channel, respectively. To conclude, after n repetition with n elements, a total of 8^n layers result.

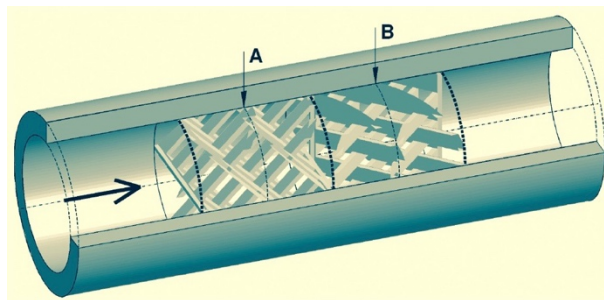


Figure 4.9 Sulzer SMX static mixer.

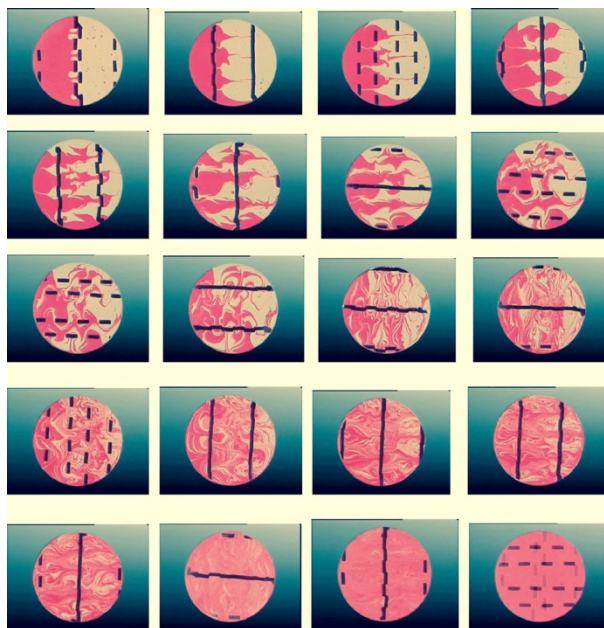


Figure 4.9 Interface creation inside a SMX static mixer.

4.3c Optimizing mixers to compactness or pressure drop

All static mixers use the same working principle of the Kenics and the SMX mixers. Using the Mapping Method to compute the flow inside, and the interface stretching and positioning in all cross sections, these mixers can be understood and optimized. Figure 4.10 shows examples

of different geometries. Interestingly, for the complex SMX mixers a whole series of geometries could be established that is optimum with respect to interface stretching. If we characterize an SMX by three numbers, $(n, N_p, N_x) =$ (number of crosses over the height, number of parallel bars over the length, number of crossing bars over the width of an element) this optimum series reads:

$$SMX(n) (n, N_p, N_x) = (2, 2n-1, 3n) \quad (4.8)$$

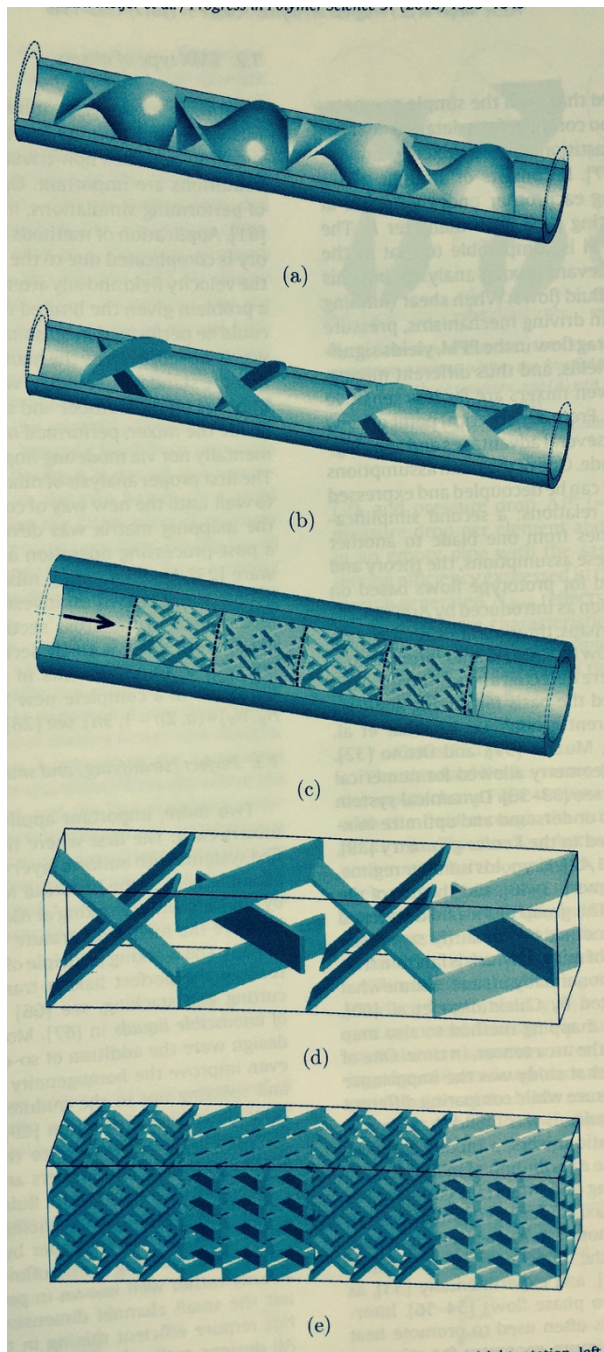


Figure 4.9 Motionless mixers: (a) Kenics (right twist – left twist; angle of blade twist 180°), (b) Ross LPD (right rotation – left rotation; crossing angle $\theta = 90^\circ$), (c) standard Sulzer SMX (n, N_p, N_x) = (number of crosses over the height, number of parallel bars over the length, number of crossing bars over the width of an element) = (2, 3, 8), and two examples of the new series of the most efficient SMX(n) (n, N_p, N_x) = (2, $2n-1$, $3n$), here in rectangular version of (d) the ‘working horse’ ($n = 1$), and of (e) the compact $n = 3$.

The mixing profiles along the length of most common static mixers, Kenics, Ross, and Sulzer, and their modifications, are computed using the mapping method and illustrated in Figure (4.10).

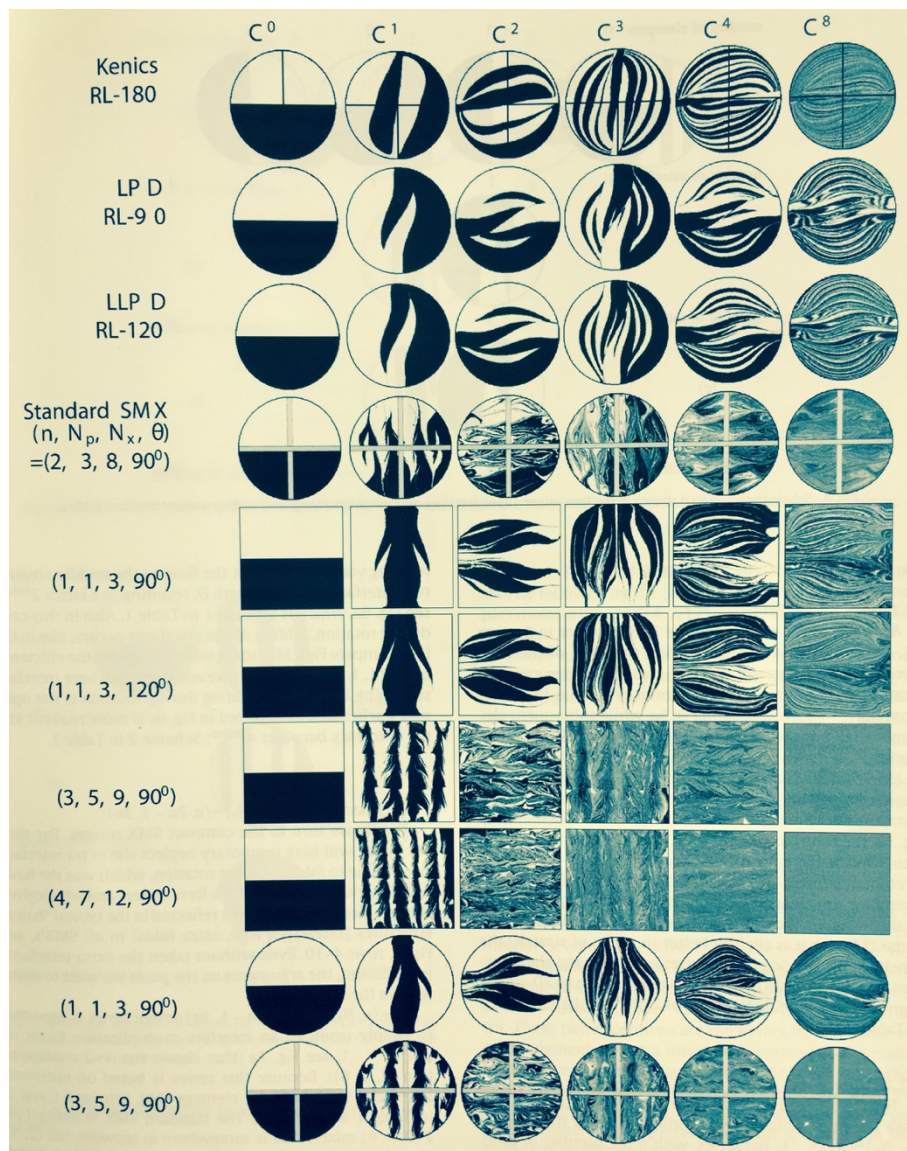


Figure 4.10 Mixing profiles in the cross sections of subsequent elements (1, 2,...8): $C^0 - C^8$, in different motionless mixers with their modifications.

Based on these computed cross sections, the mixing quality is determined. It is reflected in the so-called volume averaged 'Intensity of Segregation', which is a dimensionless number I that varies between 1 (completely un-mixed) to 0 (completely mixed). Usually its logarithm is plotted, $\log I$, since good mixing is exponential and moreover in order to enhance the visibility of the information at the most relevant level, close to zero. *Figure (4.11a)* plots mixing quality versus the length of the mixer, *Figure (4.11b)* plots quality versus pressure drop. From *Figure (4.11a)* it is clear the dense SMX mixers, winner *SMX (4, 7, 12)*, are very compact. But use a lot of pressure, see *Figure (4.11b)*. The Kenics mixer, and the low pressure drop versions *LPD* and *LLPD*, use little pressure only, *Figure (4.11b)* but are very long, *Figure (4.11a)*. Most interesting, however, is that a special version of an optimized SMX mixer, the *SMX (1, 1, 4, with $\theta = 135^\circ$)*, gives a slightly lower pressure drop than the optimized Kenics *RL-140*. This makes the static mixers based on cross plates X the most efficient ones, both with respect to compactness *SMX (4, 7, 12)*, as in pressure loses *SMX (1, 1, 4, with $\theta = 135^\circ$)*.

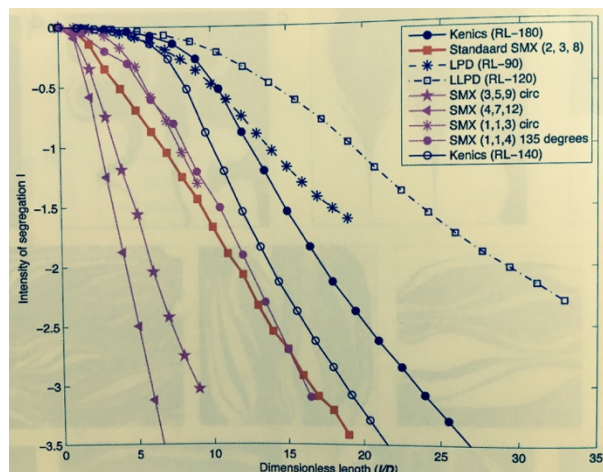


Figure 4.11a Mixing quality in terms of the logarithm of the volume averaged intensity of segregation, $\log I$, versus the (dimensionless) length of the mixer.

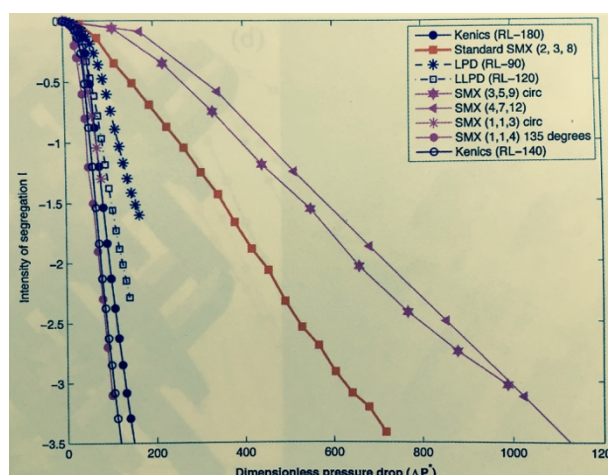


Figure 4.11b *Mixing quality in terms of the logarithm of the volume averaged intensity of segregation, $\log I$, versus pressure drop over the mixer.*

4.4 Dynamic mixers

As the discussion of static mixers has demonstrated, the principles of efficient distributive mixing can be realized in practice. In operating static mixers, a pressure flow is responsible for the throughput. Consequently, a pressure-generating device is needed. Mixing can also be directly improved in these pumps, typically extruders, because of their viscosity independent working principle. This is the area of the dynamic mixers. Although less efficient than static mixers, dynamic mixers offer a continuous flow field in which stretching, folding, and reorienting can be realized. An illustrative example is the closely intermeshing and, consequently, self-wiping co-rotating twin screw extruder, which induces folds and reorientations with respect to the streamlines during takeover of the material from one screw to the other, (Figure (4.12)).

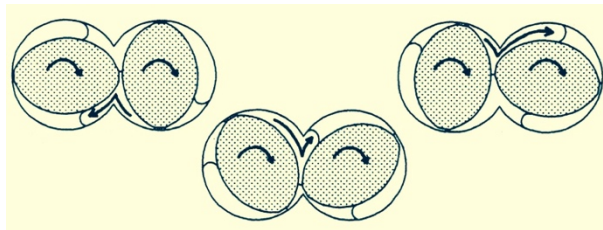


Figure 4.12 *Stretching, folding and reorienting during whipping of one screw by the other, in co-rotating twin-screw extruders.*

As stated in *Chapter 1*, modelling of co-rotating twin screw extruders is frustrated by the complex 3D geometries involved, but modern computational power has overcome this problem, see for example *Figure (4.13)*.

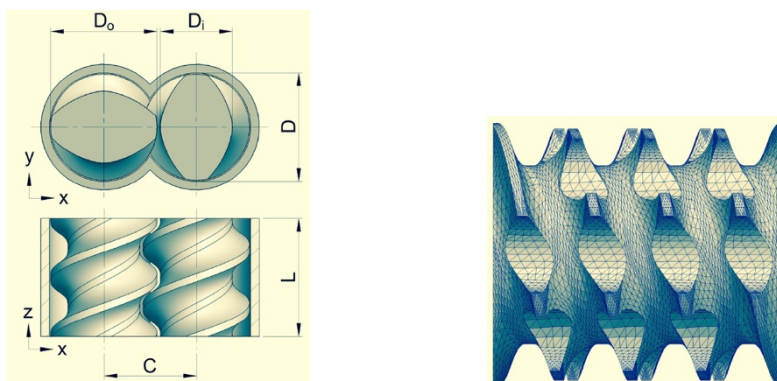


Figure 4.13 An recent example (2015) of the detailed geometry for advanced analysis, from Andres Eitzlmayr et al. from Graz University of Technology; left geometry, right mesh.

The outcomes of these, usually only local, analyses are pump characteristics of the different screw parts. How to use them to obtain information about the filled and partially filled sections of the screw has been explained in *Chapter 1*. Sometimes even a measure for mixing is tried. However, as we have concluded above, mixing can only be quantified if a measure like the area (in 2D) or volume (in 3D) averaged intensity of segregation is computed. Analyses like these are underway, see in *Figure (4.14)* an example, and our PhD student and later Postdoc Arash Fard is at night and in the weekends still working to finish the solution of the problem. We expect to, soon, be able to report on this.

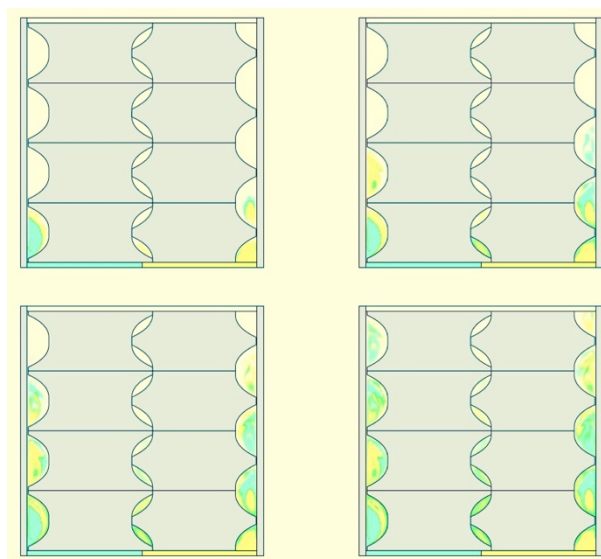


Figure 4.14 Arash Fard: Advanced analysis to determine mixing in a quantitative way in co-rotating twin-screw extruders. Shown is some results on particle tracking.

4.5 Dispersive mixing

4.5a Disintegration of threads into a row of droplets

When the original millimeter-sized liquid drops are extended into long slender filaments, as a result of the affine deformation, local radii are decreased such that the interfacial tension starts playing a role (active interfaces). In polymer melts, the shear stress and the interfacial stress become of the same order of magnitude if the radius R of the threads is decreased to $1 \mu\text{m}$.

$$\tau = \eta_c \cdot \dot{\gamma} = 10^2 \cdot 10^2 = 10^4 \text{ Pa}$$

and

$$\sigma / R = 10^{-2} \cdot 10^{-6} = 10^4 \text{ Pa}$$

thus:

$$Ca = \eta_c \cdot \dot{\gamma}_{dot} \cdot R / \sigma = 1 \tag{4.9}$$

The interfacial tension tends to minimize the interface between the two phases, minimizing as well the surface-to-volume ratio. As a consequence, small disturbances present at the interface of the liquid cylinder grow and finally result in the disintegration of the thread into a line of drops. These so-called Rayleigh distortions can be investigated experimentally every morning in the shower and are illustrated for a molten polyamide-6 (PA-6) filament, in an otherwise quiescent melt of PS, in *Figure (4.15)* [46].

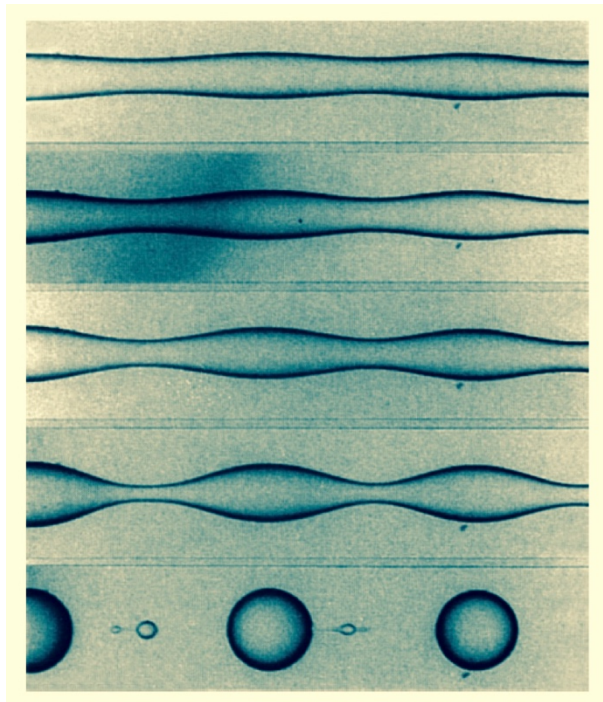


Figure 4.14 Thread breaking into drops caused by the growth of Rayleigh distortions that are driven by the interfacial tension that tries to minimize the surface-to-volume ratio of the dispersed phase.

A major difference between the two processes indicated is the value of the Reynolds number. In the shower, the interfacial stress mainly compares to inertia (We_1 : see [47]), while in molten polymer blends it compares to viscous shear stresses (Ca). Since in *Figure (4.15)* the viscosities are high and the thread is relatively thick, implying a small driving force (σ/R), the time scale of the experiment is typically minutes versus seconds in the case of breakup of free water jets. Between the drops, small satellite droplets are formed in the last stage of the disintegration process. This is a result of fast growth of Rayleigh disturbances on the fine filaments (σ/R large) formed between adjacent drops. Tjahjadi et al. [48] numerically

investigated the formation of satellite and subsatellite droplets and found that the smaller the viscosity ratio p between thread and matrix, the more satellite droplets are formed.

Figure (4.15), from Pierre Elemans, demonstrates the beautiful coordinated breakup of threads that are in proximity. *Figure (4.16)* demonstrates computed breakup, and *Figure (4.17a and 4.17b)* show computed break up during free retraction of an extended filament, without (4.17a) and with (4.17b) surfactant present.

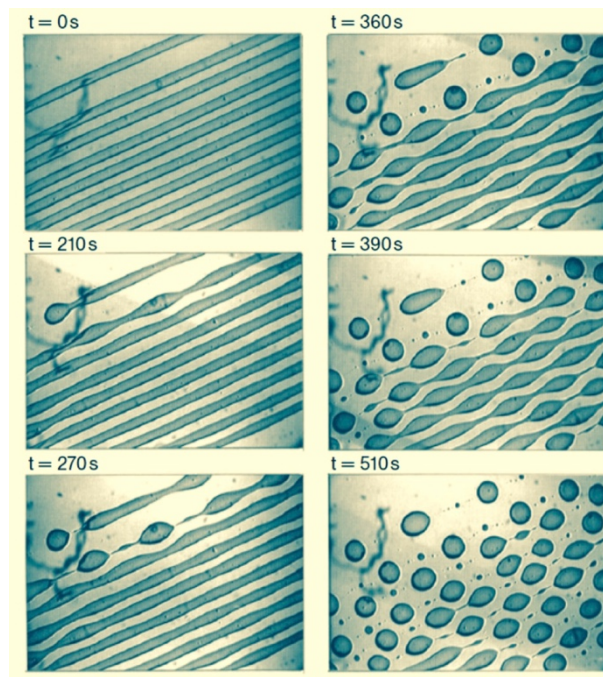


Figure 4.15 Threads in proximity break up in a coordinated way: out-of-phase breakup of 70 μm PA-6 threads in a PS matrix at 230 $^{\circ}\text{C}$; typical time scale of the experiments is 5 minutes [79].

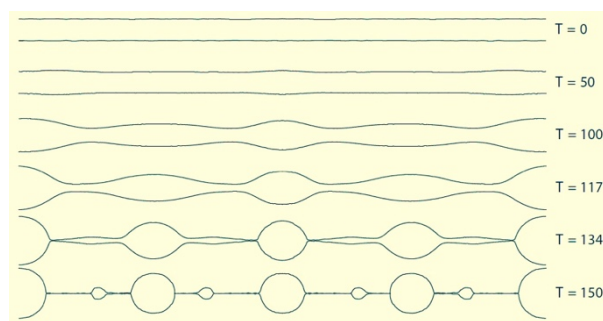


Figure 4.16 Computed thread break up.

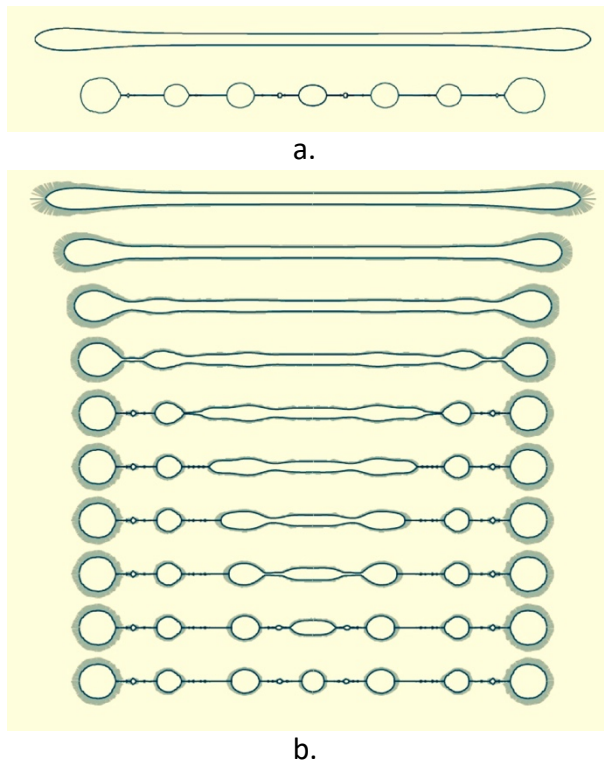


Figure 4.17 Thread break up during free contraction of an extended filament, without (a) and with (b) the presence of surfactant.

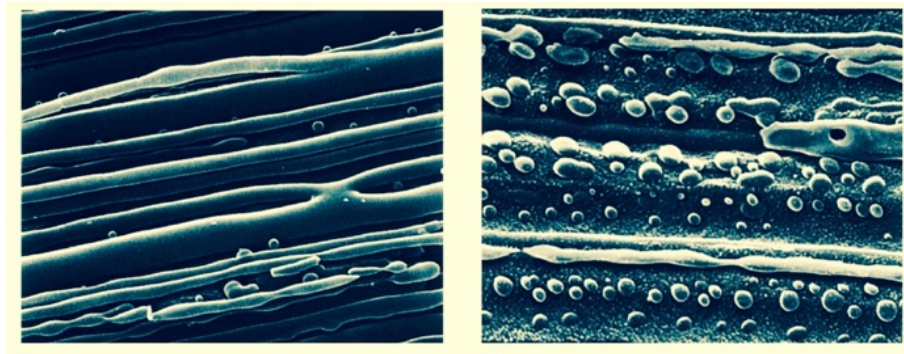


Figure 4.17 Threads leaving the extruder exit intact break up into a line of droplets once given sufficient time prior to cooling outside the extruder.

4.5b Break up of drops

Most work on dispersive mixing has been dedicated to the deformation and break up of a single drop in a steady uniform shear or extensional flow. It's relevance for practice is, however, somewhat questionable, and conclusions should be considered with some care. This is shown in *Figure (4.18)* that poses the question whether (left) stepwise drop breakup, increasing the shear rate stepwise until Ca_{max} is reached, does compare in terms of the

resulting droplet size distribution with (right) directly imposing Ca_{max} to form droplets via the break up of a thread.

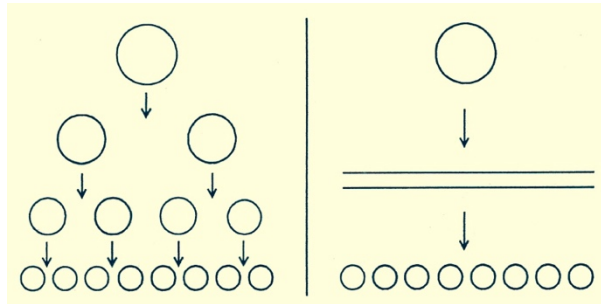


Figure 4.18 Schematic representation of two dispersion mechanisms: left, the stepwise equilibrium mechanism of repeated breakup at Ca_{crit} ; right, the transient mechanism of thread break-up during stretching. Both processes end at the same maximum shear rate, thus the same Ca_{max} .

The drop deformation and break up mechanism, that forms the basis of all classical studies on dispersive mixing, is shown in Figure (4.19). The computed process in Figure (4.20).

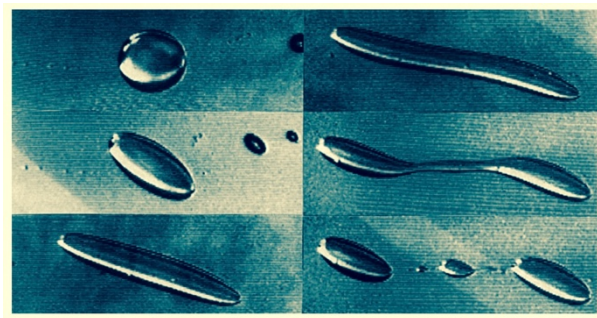


Figure 4.19 Break-up of a drop (~ 1 mm) in simple shear flow just above the critical capillary number.

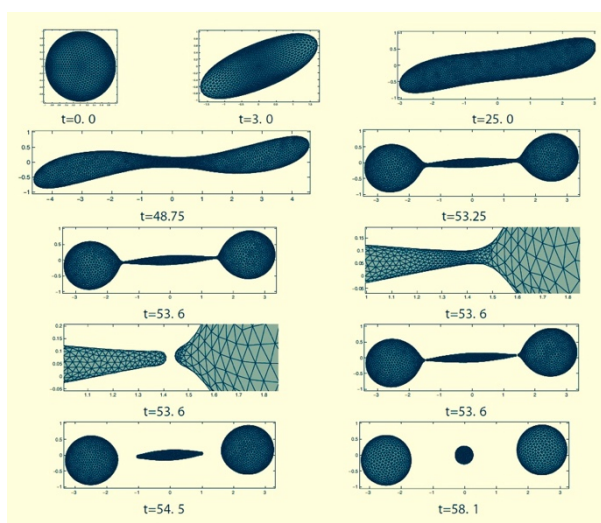


Figure 4.20 As Figure (4.19); an example of computed results.

Following the protocol of *Figures (4.19) and (4.20)*, this gradually increasing the shear rate until, at $Ca = Ca_{crit}$, the drop breaks, Grace, at that time working at DuPont, and Taylor, performed a multitude of experiments using Newtonian fluids with different viscosity ratio between dispersed and continuous phase:

$$\rho = \eta_d / \eta_c \tag{4.10}$$

The results are summarized in *Figure (4.21)* where the critical capillary number Ca_{crit} at which the drops breaks, is plotted as a function of the viscosity ratio ρ .

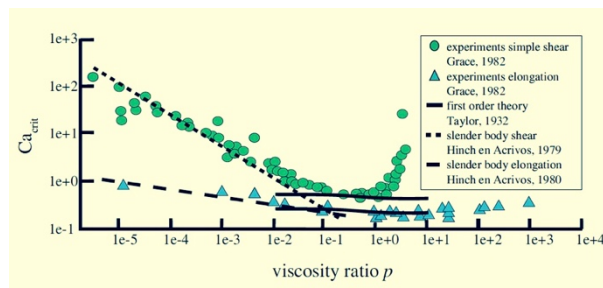


Figure 4.21 Critical capillary number Ca_{crit} versus viscosity ratio $\rho (= \eta_d/\eta_c)$, in simple shear and in elongational flow (after [62]).

In shear, very low viscosities of the dispersed drop phase ($\rho = 10^{-5}$) require a high shear rate to break ($Ca_{crit} = 100$). The low viscous drops are difficult to ‘grip’. Increasing the viscosity gradually lowers the shear rate required until the minimum of $Ca_{crit} = 1$ is reached at $\rho = 1$. At that point, the deforming shear stress τ and the spherical shape retaining surface tension force σ/R , are equal and balance. Upon further increasing the viscosity of the drops, the critical capillary number sharply start increasing again until at $\rho > 4$ no break up occurs, $Ca_{crit} = \infty$. The high viscous drops rotate away from the deformation and just tumble. Calculations confirm these experiments, see *Figure (4.22)*.

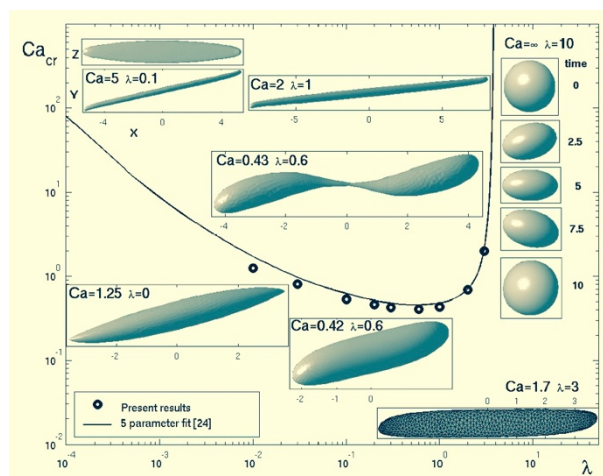


Figure 4.22 Deformation and breakup of drops at Ca_{crit} for all different viscosity ratios ρ

(from [90]).

4.5c Drops or threads

The practical conclusion of all this fundamental work on dispersive mixing was that, in order to obtain the smallest possible size of the dispersed phase, as expressed in the drop radius R , mixing at equal viscosities $p = 1$, is required. Since $Ca = \eta_c \cdot \dot{\gamma}_{dot} \cdot R / \sigma$ for a given blend system, characterized by the surface tension σ/R , and a give mixing process, characterized by the shear rate $\dot{\gamma}_{dot}$, the smallest Ca gives the smallest R . If mixing of drops with very high viscosities is required, only elongational flows can be used, see *Figure (4.21)*. The reason is that elongational flows are irrotational, such that drops can not rotate away from the deformation. A big practical disadvantage, however, is that elongational flows are difficult to sustain in technical processes.

Therefore, it is more useful to investigate what happens to drops, once partly stretched in a temporary elongational flow, when it re-enters a shear flow. This is demonstrated in *Figure (4.23)*. It shows the deformation rate of the drops versus that of the continuous matrix phase as a function of the dimensionless length L of the non-spherical drop. If $\dot{\epsilon}_{dot, d} / \dot{\epsilon}_{dot, m}$ is positive, the drop deforms, if it is zero, the drop stay stationary with the given deformation, if it is negative, the drops retract. Spherical drops are those with $L = 1$. All experiments by Grace and Taylor start in the left top of the plot, at $L = 1$ and $\dot{\epsilon}_{dot, d} / \dot{\epsilon}_{dot, m} = 1$. The viscosity ratio $p = 1$, such that $Ca_{crit} = 1$.

Drops that are sheared at $Ca < Ca_{crit}$ deform to reach a stationary slightly deformed state. Deformation at Ca_{crit} just leads to break up, while at $Ca > Ca_{crit}$ the drops keep deforming, finally with the matrix speed, into threads. Interesting is to see what happens to non-spherical drops, such as those just exiting a temporary elongational flow over a screw or kneading disc flight. Depending on the shear rate as expressed in the different Ca_{crit} numbers, $\frac{1}{4}$, $\frac{1}{2}$, drops below a certain length retract, while thos with sufficient length start deforming into long threads. *Figure (4.23)* summarizes all results, while *Figure (4.24)* gives the critical capillary number for non spherical drops. We conclude that for sufficiently elongated drops, $L = 20$, the critical capillary number is 1000 times smaller than for spherical drops.

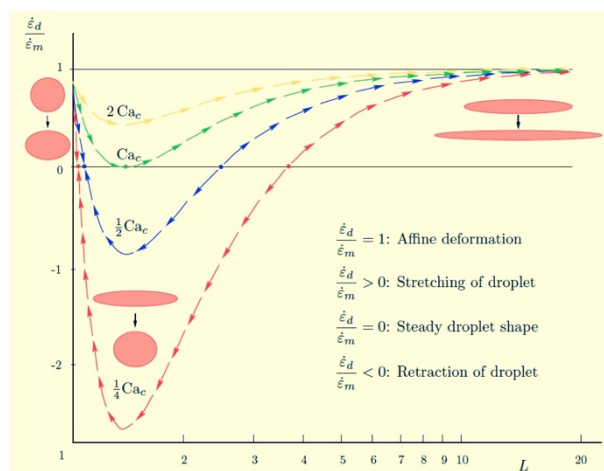


Figure 4.23 Deformation of non-spherical drops in simple shear flow at different values of Ca/Ca_{crit} . Drop stretching rate $\epsilon_{dot, d} / \epsilon_{dot, m}$ as a function of the dimensionless droplet length L at different values of the capillary number. Viscosity ratio $p = 1$ [94].

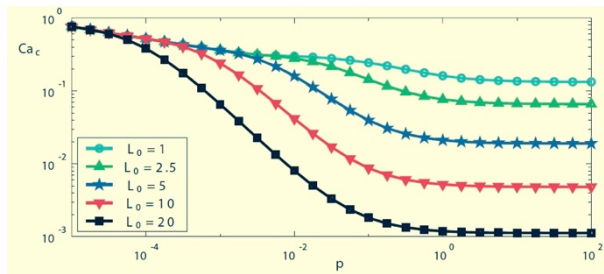


Figure 4.24 Critical capillary number Ca_{crit} as a function of the viscosity ratio p for drops with a non-spherical initial shape, characterized by length L , [94].

Finally, we investigate the even more simple situation of the deformation of a high viscosity drop in a non-homogeneous shear flow. Non-homogeneity consist of a constant, but temporary rotating, shear flow. Rotation stops after some time, See Figure (4.25).

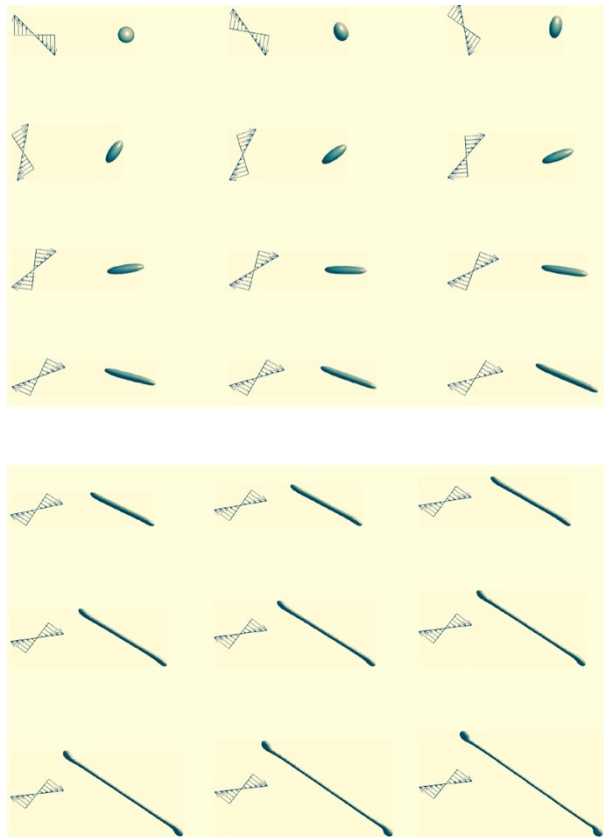


Figure 4.25 Drop in matrix with viscosity ratio $p = \eta_d/\eta_c = 10$ in temporary rotating simple shear flow. The shear flow rotates with the drop in the first 9 frames and stays

constant accordingly during the next 9 frames. Despite the large p -value the drop stretches!

It is clear that the high viscous drop, $p = 10$, that according to all classical dispersive mixing research could not deform and break in simple shear flow, indeed does deform and stretches out to infinite length if the shear flow gets 'grip' on the drop, in the initial stages just by rotating with the drop such that the latter can not escape from the deformation. These are an interesting and useful results that a.o. helps explaining why an automotive blend like *Noryl GTX*, with a high viscous dispersed phase (*PPE*) in a low viscous matrix (*PA*) could be produced on co-rotating twin-screw extruders by, at that time, GE-Plastics in Bergen op Zoom.

4.5d Coalescence of drops

Up to this point, the dispersion of isolated drops and threads was discussed. Most practical applications, however, involve blends that are sufficiently concentrated to exhibit coalescence of the drops formed. Elmendorp [96] in 1986 showed experimentally that already at a volume fraction of a few percent dispersed phase, the morphology is significantly coarsened by coalescence. At high volume fractions (around 50%, see Section 3.6.3), phase inversion may occur. In the modeling of coalescence, two aspects have to be considered:

- do drops collide within a given process time and
- will a collision be successful, *i.e.*, does the film between the drops drain sufficiently during the available interaction time.

Figure *Figure (4.26)* shows two colliding drops in simple shear flow. The 'external flow' and the volume fraction dispersed phase govern the collision frequency. In addition, the external flow is responsible for the contact force and the interaction time of the collision, the boundary conditions for the film drainage or 'internal flow'.

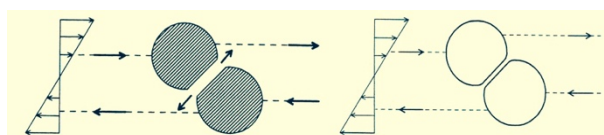


Figure 4.26 Collision of two deformable drops in simple shear flow, with drainage of the film in between.

The drainage process is controlled by the mobility of the interfaces between drop and matrix. We distinguish immobile, partially mobile and fully mobile interfaces, as e.g. controlled by the presence of surfactants, see *Figure (2.27)*. All local processes have been successfully modelled, resulting in the chance on collision, on successful drainage, and thus combined on successful coalescence, see *Figure (4.28)*. Combining binary break up models with successful coalescence models finally give an estimate of the size of the resulting drop size population as a function of the relative flow strength, see *Figure (4.29)*.

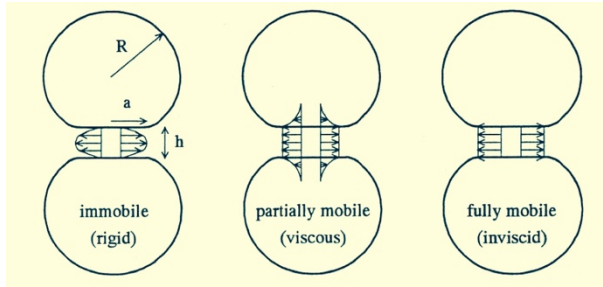


Figure 4.27 Internal flow field of film drainage between colliding deformable drops with immobile, partially mobile, and fully mobile interfaces.

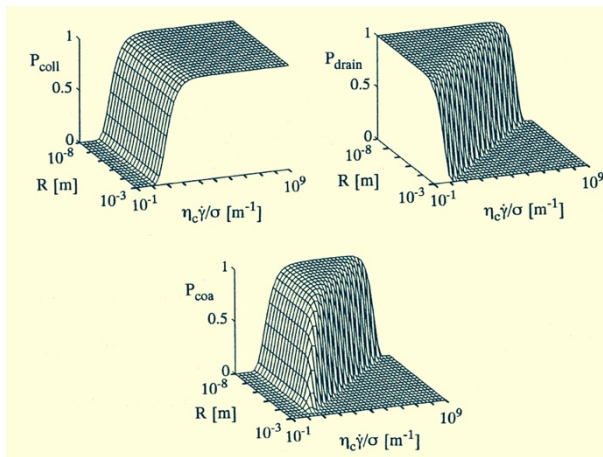


Figure 4.28 Collision-, drainage-, and overall coalescence probability as a function of radius R and flow parameter $\eta_c \dot{\gamma} / \sigma$. Conditions: simple shear flow, $t_{proc} = 50$ s, $\eta_d = \eta_c = 1$ Pa s, $\sigma = 10^{-2}$ N/m, $h_{crit} = 10^{-9}$ m, $\varphi = 0.1$, drainage with partially mobile interfaces.

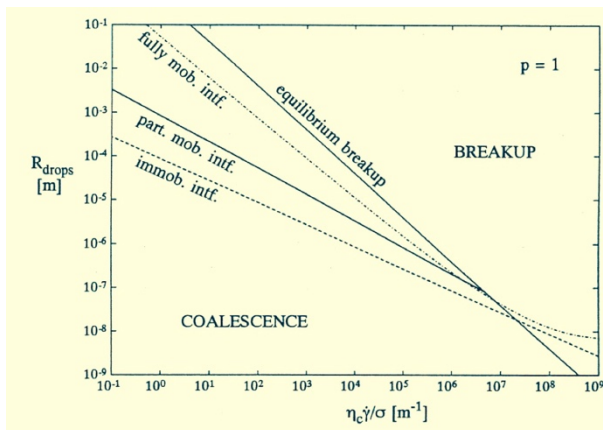


Figure 4.29 Comparison of drop sizes resulting from stepwise equilibrium breakup and coalescence after long process time in simple shear

4.6 A simplified dynamic model

In the preceding sections, the most relevant stages of the blending process of immiscible liquids have been discussed: affine stretching of dispersed drops including reorientations and folds, disintegration of the formed liquid threads, further drop deformation and breakup, and coalescence of small drops into larger ones. The resulting criteria for Newtonian liquids are quite complete and can be combined into an overall mixing model that describes the development of the morphology during the blending process (see Janssen and Meijer [114]). A schematic 2-zone model has been chosen that has an analogy with the mixing model for carbon black in rubber as proposed by Manas-Zloczower *et al.* [111,112]. The 2-zone model is depicted in *Figure (4.30)*. The material passes cycles through alternating 'strong' and 'weak' zones. A diversity of practical mixing devices can be modeled by variation of the flow conditions in the zones (residence times and deformation rates). The 2-zone model is directly applicable to stirred vessels (with the impeller region the strong and the macro circulation the weak zone), but it can also be applied to completely different types of mixers. Here, the model is treated mainly in view of polymer blending in melt extruders.

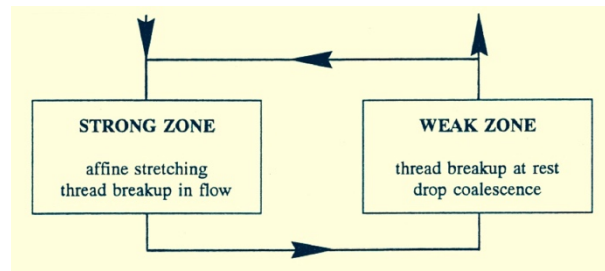


Figure 4.30 Principle of the 2-zone mixing model: material passes cycles through alternating strong and weak flow zone.

The strong zone represents regions of a mixer where high deformation rates are present. It is modeled by an elongational flow with high elongation rate $\dot{\epsilon}$ and a short residence time t . In this zone, exponential stretching of dispersed drops and threads takes place. During stretching, it is checked if the threads formed are thin enough to disintegrate in the flow. Although the strong zone is modeled by elongational flow, simulating, *e.g.*, the entrance of a narrow gap before a kneading disc, may also represent a sequence of stretching and folding in a simple shear dominated region. In both cases, stretching proceeds exponentially.

The weak zone represents quiescent regions of the mixer and is modeled by simple shear; the shear rate $\dot{\gamma}$ is small, the residence time t large. Threads entering this zone may break up at (almost) rest, if the residence time suffices. Drops coalesce, if the remaining residence time allows for collisions with successful film drainage. Repeated coalescence may take place during each passage of the weak zone, if there is time available. In order to get a distribution of drop sizes, the residence time in the weak zone is distributed as a cascade of n ideal mixers.

4.6a Transient mixing process

Next we focus on the numerical simulation of the 2-zone model. Since the number of drops increases enormously (1 mm sized drop yields 10^9 μm sized drops), drop ‘families’ are considered rather than individual drops. Each family contains a number of identical drops/threads that are characterized by a single radius R , an aspect ratio L/B (with $B = 2R$), and a cumulative residence time. Within a family, no time distribution is applied so that a number of different drop families has to be used (instead of 1) in order to generate a distribution of drop sizes. This distribution is initiated artificially to have a certain range from the start on. Further distribution is achieved due to the residence time in the weak zone. All drop families start in the strong zone, pass through a specified number of cycles, and finally leave from the weak zone. Passing each zone, subroutines check for each drop family whether or not the current size and flow conditions give rise to stretching, breakup, or coalescence. A schematic overview of the model is given in *Figure (4.31)*. An illustration of the dynamics of the dispersive mixing process is given in *Figure (4.32)*.

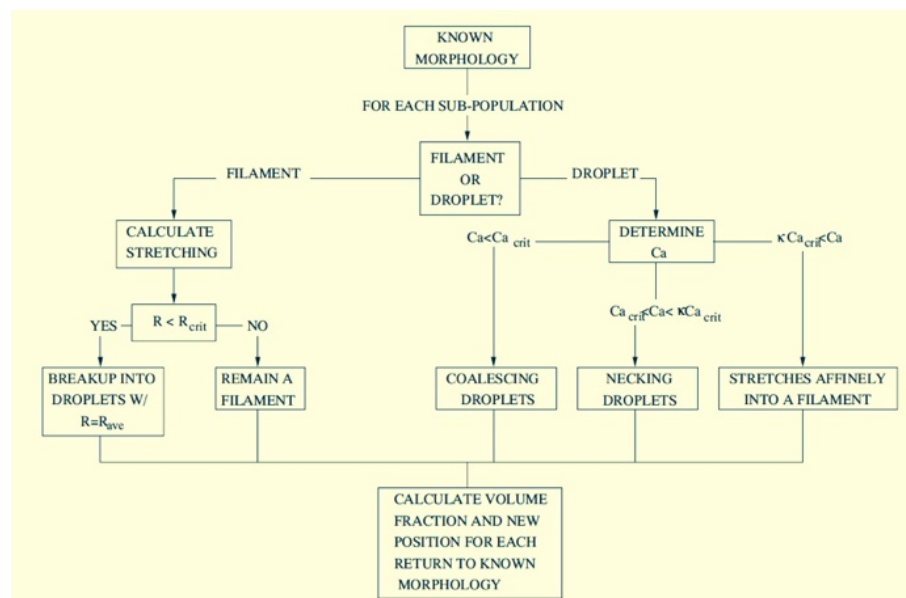


Figure 4.31 Structure development during flow in immiscible liquids; scheme used to compute the transient stress development [130].

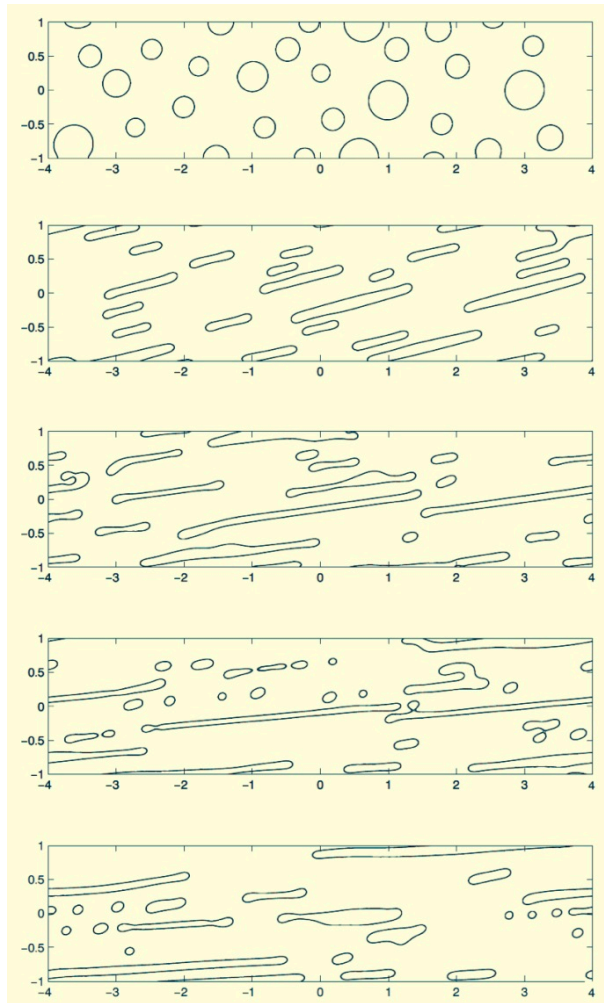


Figure 4.32 Transient structure developing during start-up flow using DIM with bi-periodic Lees Edwards boundary conditions [146].

As an example we consider melt blending of polymers in an extruder. The simulation is based on analyses for Newtonian liquids. The relevant material parameters are chosen as follows: $\eta_d = \eta_c = 100$ [Pa.s], $\sigma = 5 \cdot 10^{-3}$ [N/m], $\alpha_0 = 10^{-9}$ [m], and volume fraction of the dispersed phase is $\varphi = 0.2$. The strong zone is modeled by $\varepsilon_{dot} = 30 \text{ s}^{-1}$ and $t = 0.1 \text{ s}$ (yielding $L/B = e^3/e^{-3/2} = 90$ upon affine stretching of a sphere); in the weak zone $\gamma_{dot} = 3 \text{ s}^{-1}$ and the residence time distribution resembles a cascade of 2 ideal mixers with a total mean residence time $t = 10$ [s]. A population of 100 drop families is initiated with diameters around 1 [mm].

Figure (4.32) shows the evolution of the drop size distribution as the population passes cycles through alternating strong and weak zones. During the first 3 cycles of alternating strong and weak zones, all drops are stretched affinely in the strong zone: threads of approx. 10 μm thickness are formed. This is too thick to break up either during stretching or at rest in the weak zone (given the residence time); so, nothing happens in the weak zone. The extremely large aspect ratios (L/B) represent packages of folded threads. During the 4th cycle, after

further stretching in the strong zone, some of the threads break up into droplets ($L/B = 1$) in the weak zone. The breakup time required at rest has decreased with the radius and has now reached the mean residence time in the weak zone. In the 5th cycle, the drops and remaining threads are stretched again. All threads formed are thin enough to disintegrate during the residence time available in the weak zone. At this point, submicron drops appear that may easily coalesce: the lower limit of the drop size is reached. After 6 cycles, a dynamic steady state is reached: too small drops coalesce (repeatedly); too large ones stretch and break again.

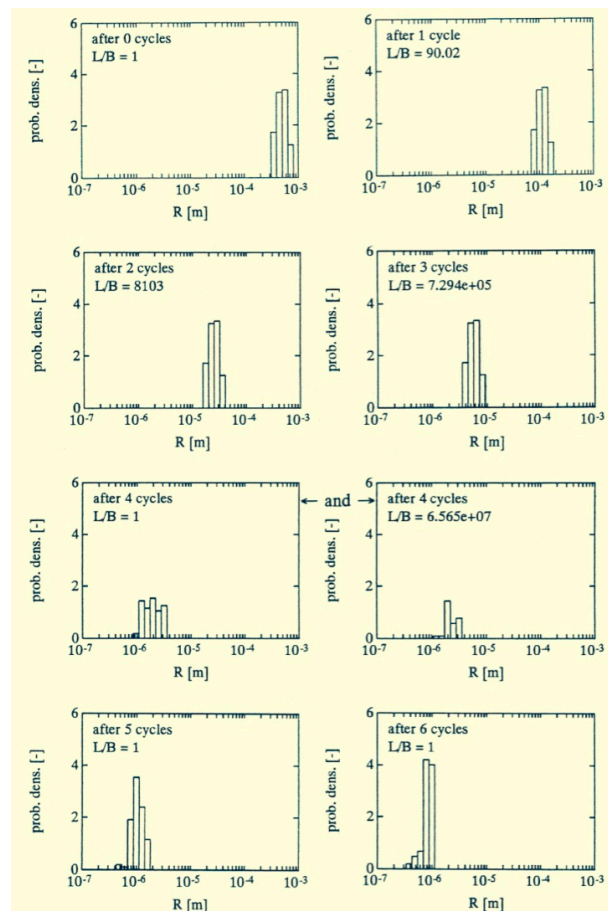


Figure 4.33 Morphology development in the 2-zone mixing model with: $\eta_d = \eta_c = 100 \text{ Pa s}$, $\sigma = 5.10^{-3} \text{ N/m}$, $\alpha_0 = 10^{-9} \text{ m}$, and $\varphi = 0.2$; strong zone: $\varepsilon = 30 \text{ s}^{-1}$ and $t = 0.1 \text{ s}$; weak zone: $\gamma = 3 \text{ s}^{-1}$ and $t = 10 \text{ s}$. Note that after 4 cycles two distributions with different L/B apply.

4.6b Optimization of viscosity ratio p

Figure (4.34) shows the steady state drop sizes (after 10 cycles) for different viscosity ratios p and the residence time distribution that is characteristic for all three cases. The drop size distribution for $p = 1$ corresponds to Figure (4.33) and confirms that the result after 6 cycles is indeed the steady state. Keeping η_c constant, a larger η_d ($p = 100$) promotes finer dispersion due to retardation of both thread breakup (allowing for further stretching) and coalescence (eventually switching to immobile interfaces). The dispersion route is mainly the one step

breakup of highly extended threads. Upon decreasing η_d ($p = 0.01$), threads break up more quickly, implying a stepwise stretching and breakup route, this results in coarser morphologies. In addition, the smaller value of η_d favors coalescence (eventually switching to fully mobile interfaces). Systems with higher viscosities favor a thread-like dispersion route (larger time required for thread breakup) with suppression of coalescence.

A similar effect of the viscosity ratio on the dispersion route and the drop size was reported by Tjahjadi and Ottino [55] and Muzzio *et al.* [117]; in addition, they found a broader drop size distribution upon increasing p , which is probably due to their omission of coalescence. In general, for a given set of processing conditions, a lower level of both viscosities yields a coarser morphology, while highly viscous systems can be dispersed finer.

As already mentioned in *Section 4.5c*, the commercial blend *Noryl GTX* (General Electric Plastics, now Sabic International) is a practical example where a large viscosity ratio p indeed leads to a fine dispersion. Essentially, a highly viscous polyphenylene ether melt is dispersed in a much lower viscous polyamide continuous phase ($p = 20$). Just looking at the critical capillary number for drop breakup suggests that a fine dispersion cannot be obtained, because the viscosity ratio p is far beyond 1. However, taking into account all mechanisms such as in the 2-zone model, it becomes clear that this blend can easily be dispersed to a length scale of 10^{-7} m, which is reality. It should be noted that this commercial blend, of course, contains many additives among which a rubbery third phase and compatibilizers.

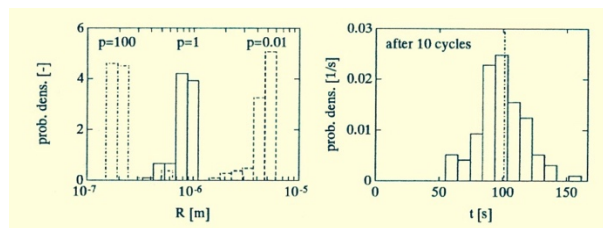


Figure 4.34 Left: Steady state morphology from the 2-zone mixing model with: $\eta_c = 100$ Pa s, and $\eta_d = 104, 102,$ or 1 Pa s ($p = \eta_d/\eta_c = 102, 1$ and 10^{-2}); other conditions are the same as in Fig. 3.124. Right: Residence time distribution characteristic for all 3 cases.

4.6c Optimization of mixer geometry

The 2-zone model lends itself for comparing the influence of processing conditions. Increasing the strain ($\epsilon_{dot} \cdot t$) applied in the strong zone yields thinner threads within a single passage. In the extreme, thread breakup during stretching results in drop sizes. In most cases, however, the final drop size strongly depends on the occurrence of coalescence. In the weak zone, a longer residence time favors thread breakup at rest and thus implies a stepwise breakup route. Whether coalescence is also favored by a longer residence time in the weak zone depends on the shear rate: not too small to be sure of collisions and not too large to assure successful film drainage. The volume fraction ϕ affects the model both via the enlarged

effective matrix viscosity and the collision frequency for coalescence: generally, a larger φ gives a coarser morphology. Moreover, in reality a larger φ generates a higher level of initial disturbances α_0 due to the pushing of neighboring drops and threads. This accelerates thread breakup and makes the dispersion route more stepwise, resulting in a coarser morphology. A nice example of varying the processing conditions is the optimization of the gap height δ between kneading flight and barrel wall in an extruder. The converging flow region at the entrance of the gap can be made more effective for the stretching of drops and threads by decreasing the gap width, causing a larger strain (rate)). However, if the gap becomes narrower, less material actually passes through, while more and more material avoids the gap. The extreme cases are

- a gap height equal to zero, $\delta/H = 0$ so that $\varepsilon = \infty$, but implying that no material can pass and
- a gap width equal to the channel depth ($\delta/H = 1$, or no flight at all) so that all material will pass, however, with $\varepsilon = 0$.

Both cases correspond to a sequence of weak zones only, which is bad for the purpose of stretching drops and threads. Somewhere in between the extremes, there is an optimal gap width δ/H such that a certain fraction of the material indeed passes through, while the value of ε is still considerable. In *Figure (4.35)* such an optimization is illustrated, based on the two-zone mixing model. The resulting mean drop size is calculated as a function of δ/H .

The points in *Figure (4.35)* represent the mean drop diameters resulting from the simulations; the curve is a fit.

For very narrow gaps (regime I), the stretching rate is large ($\varepsilon_{dot} = 44$ [s^{-1}]), but only a few cycles are performed within the residence time given ($N = 3$). The dispersion route contains a few large stretching operations followed by final breakup.

In regime II, more cycles are included, while ε_{dot} is still substantial (e.g., in the reference case indicated by the arrow, $N = 6$ and $\varepsilon_{dot} = 30$ [s^{-1}]) The dispersion route includes stretching, breakup, and coalescence.

In regime III, the value of ε_{dot} becomes quite small, but the number of cycles is large enough to obtain a steady state morphology.

In regime IV, although N is large ($N = 20$), the strain per passage is so small that it takes this many cycles to thin the stretching threads down to the micrometer range. At the same time, the residence in the weak zone becomes so short ($t = 3$ [s]) that only very thin threads ($R < 1$ μm) break up. If, in the simulation results underlying *Figure (4.35)*, threads result after the last cycle, they are broken artificially to obtain drops, thus mixing ends with a long stay in a weak zone in all cases. The presence of an optimum gap height δ/H of about 0.25 is evident. For large values of δ/H , the simulations are somewhat questionable, since some basic assumptions no longer hold. In particular, the strong zone becomes weaker and loses its character. Irrespective of the exact values, the main message from this exercise is that “worn” extruder screws or kneading wings might be superior to new (more closely fitting) ones, as

already pointed out by Manas Zloczower *et al.* [111]. Moreover, this result suggests that in the scaling up of a compounder, the gap should be scaled accordingly in order to keep δ/H optimal, instead of minimizing its value.

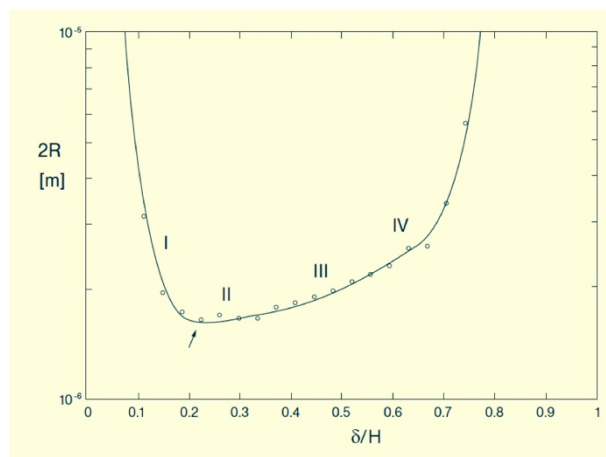


Figure 4.35 Mean drop size as a function of the gap height using a two-zone model with the parameters of Fig. 3.125. Symbols give the simulation results; the line is a fit. The arrow indicates the reference case, *i.e.*, conditions as in Fig. 5.3 after 6 cycles.

The 2-zone model is relatively simple but clearly illustrates the dynamics and interaction of the relevant mechanisms. An important conclusion after many simulations is that the final drop size cannot be predicted just by the critical capillary number for drop breakup under quasi-equilibrium conditions. The transient character of the mechanisms (including coalescence) has to be taken into account to predict the typical trends observed in practice.

5. List of symbols

symbol	dimension	description
a	[-]	'drossel' ratio; ratio pressure to drag flow
B	[m]	channel width
B	[-]	B number; ratio heat dissipation to radial heat transfer
Br	[-]	Brinkman number; ratio heat dissipation to conduction
c	[J/kg ⁰ C]	heat capacity
D	[m]	extruder diameter
D_{is}	[J/sm ³]	heat dissipation
E	[W] = [J/s] = [Nm/s]	energy
E_{sp}	[N/m ²] = [J/m ³]	specific energy
f	[-]	degree of fill
Gz	[-]	Graetz number; ratio heat convection to conduction
H	[m]	channel height
h	[m]	die/resistance height
k	[m ²] in 2D; [m ³] in 3D	reciprocal die resistance coefficient
L	[m]	channel length
L_{ax}	[m]	axial extruder length
L_f	[m]	completely filled screw length
L_a	[-]	local length screw part a
L_b	[-]	local length screw part b
L_c	[-]	local length screw part c
l_a	[-]	relative local length screw part a
l_b	[-]	relative local length screw part b
l_c	[-]	relative local length screw part c
l	[m]	die/resistance length
N	[rpm]	extruder screw rotational speed in rounds per minute
P	[Pa = N/m ²]	pressure
P	[-]	P number; ratio heat convection to radial heat transfer
ΔP	[Pa]	pressure difference
dP/dx	[Pa/m] = [N/m ³]	pressure gradient
Q	[m ² /s] in 2D; [m ³ /s] in 3D	throughput
Q_d	[m ³ /s]	drag flow in 3D
Q_p	[m ³ /s]	pressure flow in 3D
q''	[J/sm ²]	heat flux density
T	[⁰ C]	temperature

T^*	[-]	<i>dimensionless temperature ($T/(T_1-T_0)$)</i>
T_0	[°C]	<i>lower wall temperature</i>
T_1	[°C]	<i>upper wall temperature</i>
T_o	[Nm]	<i>torque</i>
u	[m/s]	<i>velocity</i>
V	[m/s]	<i>wall velocity</i>
V_f	[m ³]	<i>completely filled screw volume</i>
w	[1/m ²] in 2D; [1/m ³] in 3D	<i>die resistance coefficient</i>
W	[m]	<i>extruder channel width</i>
x	[m]	<i>x-coordinate</i>
x^*	[-]	<i>dimensionless x-coordinate (x/L)</i>
y	[m]	<i>y-coordinate</i>
y^*	[-]	<i>dimensionless y-coordinate (y/H)</i>
z	[m]	<i>z-coordinate</i>
η	[-]	<i>pump efficiency</i>
λ	[J/sm ⁰ C]	<i>heat conductivity coefficient</i>
μ	[Pa.s]	<i>viscosity</i>
ρ	[kg/m ³]	<i>density</i>
τ	[Pa] = [N/m ²]	<i>shear stress</i>

6. References

6a. Modelling chapter

1. W. Szydlowski, R. Brzoskowski, and J. L. White, *Int. Polym. Proc.*, 1, 207 (1987).
2. J. L. White and K. Min, *Eur. Symp. on Pol. Blends*, Strasbourg, France (May 1987).
3. M.L. Booy, *Polym. Eng. Sci.*, 18, 973 (1978).
4. H. Werner, Ph.D. Thesis, Munich University of Technology, West Germany (1976).
5. M.L. Booy, *Polym. Eng. Sci.*, 20, 1220 (1980).
6. *Engineering (London)*, 114, 606 (1922).
7. H. W. Rowell and D. Finlayson, *Engineering (London)*, 126, 249, 385 (1928).
8. C. J. Rauwendaal, *Polym. Eng. Sci.*, 21, 1092 (1981).
9. H. Herrmann and U. Burckhardt, *Kunststoffe*, 68, 753 (1978).
10. H. Herrmann and U. Burckhardt, *Kunststoffe*, 68, 19 (1978).
11. K. Eise, S. Jakopin, H. Herrmann, U. Burckhardt, and H. Werner, *Adv. Plast. Technol.*, 18 (April 1978).
12. U. Burckhardt, H. Herrmann, and S. Jakopin, *Plast. Compounding*, 73 (1978).
13. M. L. Booy, *Polym. Eng. Sci.*, 15, 606 (1975).
14. C. J. Rauwendaal, "Polymer Extrusion," Hanser Publishers, Munich (1986).
15. L. P. B. M. Jansen, "Twin Screw Extrusion," Elsevier, Amsterdam (1978).
16. R. Chella, R.W. Foster, and J.T. Lindt, paper presented at the Third Meeting of the PPS, Stuttgart, West Germany (April 1987).
17. J. M. McKelvey, "Polymer Processing," John Wiley & Sons, New York (1962).
18. Z. Tadmor and C. G. Gogos, "Principles of Polymer Processing," John Wiley & Sons, New York (1979).
19. S. Middleman, "Fundamentals of Polymer Processing," McGraw Hill, New York (1977).
20. J. Noordermeer, *Proceedings Int. Conf. on Rheology*, Acapulco, Mexico (1985).
21. N. Tokita and J. L. White, *J. Appl. Polym. Sci.*, 10, 1011 (1966).
22. J. L. White and N. Tokita, *J. Appl. Polym. Sci.*, 12, 1589 [1968].
23. I. Manas-Zloczower, A. Nir, and Z. Tadmor, *Rubber Chem. Technol.*, 55, 1250 (1982).
24. I. Manas-Zloczower, A. Nir, and Z. Tadmor, *Rubber Chem. Technol.*, 57, 583 (1984).
25. I. Manas-Zloczower, A. Nir, and Z. Tadmor (submitted to *Rubber Chem Technol.*).
26. H. Gosler (Werner & Pfeleiderer), private communications.
27. B. H. Maddock, *SPE ANTEC Tech. Papers*, 5, 383 (1959).
28. Z. Tadmor, *Polym. Eng. Sci.*, 6, 185 (1966).
29. J. F. Ingen Housz and H. E. H. Meijer, *Polym. Eng. Sci.* 21, 352 (1981).
30. J. F. Ingen Housz and H. E. H. Meijer, *Polym. Eng. Sci.* 21, 1156 (1981).

31. Z. Tadmor, P. Hold, and L. Valsamis, SPE ANTEC, Tech. Papers, 25, 193 (1979).
32. J. Nordmeier, Ph.D. Thesis, Aachen University of Technology, West Germany (1986).
33. J. F. Carley, R. S. Mallouk, and J. M. McKelvey, Ind. Eng. Chem., 45, 974 (1953).
34. J. F. Carley and R. A. Strub, Ind. Eng. Chem., 45, 970 (1953).
35. R. S. Mallouk and J. M. McKelvey, Ind. Eng. Chem., 45, 987 (1953).
36. K. Y. Ng and L. Erwin, Polym. Eng. Sci., 21, 4 (1981).
37. P. Fischer, Ph.D. Thesis, Aachen University of Technology, West Germany (1976).
38. C. D. Denson and B. K. Hwang, Polym. Eng. Sci., 20, 965 (1980).
39. J. R. A. Pearson and S. M. Richardson, ed., "Computational Analysis of Polymer Processing," Appl. Sci., London (1983).
40. Jepson, Ind. Eng. Chem., 45, 992 (1953).
41. H. Janeschitz-Kriegl and J. Schijf, Plast. Polym., 523 (Dec. 1969).
42. R. Erdmenger, Chem. Ing. Techn., 35, 175 (1964).
43. J. J. Elmendorp, Ph.D. Thesis, Delft University of Technology (1986).
44. J. F. Ingen Housz, Intern. Zeitschrift für Lebensmittel Technologie, 1/82, 48 (1982).
45. J. F. Ingen Housz, Polymer Extrusion 2. Paper 8, London (1982).
46. J. R. A. Pearson, Plast. Rubber Process., 119 (Sept. 1976).

6b. Mixing chapter

- [1] Meijer, H. E. H., Lemstra, P. J., Elemans, P. H. M., Makromol. Chem., Macromol. Symp., **16**, 113 (1988).
- [2] Catchpole, J., Fulfort, G. D., in Fluid Mechanics Source Book, Dimensionless Groups, Parker, S. P. (Ed.), McGraw Hill, London, p. 158 (1988).
- [3] Taylor, G. I., Proc. R. Soc., London, **A138**, 41 (1932).
- [4] Taylor, G. I., Proc. R. Soc., London, **A146**, 501 (1934).
- [5] Einstein, A., Ann. Phys., **19**, 289 (1906), **34**, 591 (1911).
- [6] Ghosh, A. K., Ranganathan, S., Lindt, J. T., Lorek, S., SPE ANTEC Tech. Pap., 232 (1991).
- [7] Gordon, J. E., The New Science of Strong Materials, or Why You Don't Fall Through the Floor, Chap. 10, Penguin, London (1968, 1978).
- [8] Gordon, J. E., Structures, or Why Things Don't Fall Down, Penguin, London (1978).
- [9] Ng, K. Y., Erwin, L., Polym. Eng. Sci., **21**, 4 (1981).
- [10] Sluijters, R., Ingenieur (in Dutch), **77**(15), 33 (1965) and US Patent 3051453, 1959.
- [11] Schilo, D., Ostertag, K., Verfahrenstechnik (in German), **6**(2), 45 (1972).
- [12] Prigogine, I., Stengers, I., Order Out of Chaos, Flamingo, Glasgow (1984).
- [13] Van de Sanden, M. C. M., Meijer, H. E. H., Lemstra, P. J., Polymer, **34**(10), 2148–2154 (1993).

- [14] Van de Sanden, M. C. M., Buijs, L. G. C., De Bie, F., Meijer, H. E. H., *Polymer*, **35**(13), 2783–2792 (1994).
- [15] Kruijt, P. G. M., Galaktionov, O. S., Peters, G. W. M., Meijer, H. E. H., *International Polymer Processing*, **XVI**(2), 151–160 (2001).
- [16] Van der Hoeven, J. C., Wimberger-Friedl, R., Meijer, H. E. H., *Polymer Engng. & Sc.*, **41**(1), 32–42 (2001).
- [17] Liu, S. P., Hrymak, A. N., Wood, P. E., *AIChE Journal* **52** (1): 150–157 (2006).
- [18] Kruijt, P. G. M., Galaktionov, O. S., Anderson, P. D., Peters, G. W. M., Meijer, H. E. H., *AIChE Journal*, **47**(5), 1005–1015 (2001).
- [19] Galaktionov, O. S., Anderson, P. D., Peters, G. W. M., Meijer, H. E. H., *International Polymer Processing*, **XVIII**(2), 138–150 (2003).
- [20] Galaktionov, O. S., Anderson, P. D., Peters, G. W. M., Meijer, H. E. H., *CJCHE*, **80**(6), 604–613 (2002).
- [21] Meleshko, V. V., Galaktionov, O. S., Peters, G. W. M., Meijer, H. E. H., *Eur. J. Mech. B/Fluids*, **19**(4), 529 (2000).
- [22] Galaktionov, O. S., Anderson, P. D., Peters, G. W. M., Tucker III, C. L., *Int. Journal of Multiphase Flow*, **28**(3), 497–523 (2002).
- [23] Galaktionov, O. S., Anderson, P. D., Peters, G. W. M., *Phys. Fluids*, **14**(9), 3009–3017 (2002).
- [24] Anderson, P. D., Galaktionov, O. S., Peters, G. W. M., Meijer, H. E. H., Tucker III, C. L., *Int. J. Num. Meth. Fluids*, **40**(1–2), 189–196 (2002).
- [25] Krasnopolskaya, T. S., Meleshko, V. V., Peters, G. W. M., Meijer, H. E. H., *Eur. J. Mech. B/Fluids*, **18**, 793–822 (1999).
- [26] Kruijt, P. G. M., Galaktionov, O. S., Peters, G. W. M., Meijer, H. E. H., *International Polymer Processing*, **XVI**(2), 161–171 (2001).
- [27] Galaktionov, O. S., Anderson, P. D., Peters, G. W. M., Meijer, H. E. H., *Int. J. Num. Meth. Fluids*, **40**(3–4), 345–351 (2002).
- [28] Sarhangi Fard, A., Famili, N. M., Anderson, P. D., *Computers & Chemical Engineering*, **32**, 1471–1481 (2008).
- [29] Ottino, J. M., Chella, R., *Polym. Eng. Sci.*, **23**, 7 (1983).
- [30] Chella, R., Ottino, J. M., *Ind. Eng. Chem. Fundam.*, **24**, 170 (1985).
- [31] Elemans, P. H. M., Chapter 10 in *Encyclopedia of Fluid Mechanics*, Cheremisinoff, N. P. (Ed.), Vol. 9, *Polymer Flow Engineering* (1990).
- [32] Metcalfe, G., Rudman, M., Brydon, A., Graham, L. J. W., Hamilton, R., *AIChE J.* **52**, 1, 9–28 (2005).
- [33] Speetjens, M., Metcalfe, G., Rudman, M., *Physics of Fluids* **18** (10) (2006).
- [34] Ottino, J. M., *The Kinematics of Mixing: Stretching, Chaos and Transport*, Cambridge University Press, Cambridge (1989).
- [35] Ottino, J. M., *Annu. Rev. Fluid Mech.*, **22**, 207 (1990).
- [36] Leong, C. W., Ottino, J. M., *J. Fluid Mech.*, **209**, 463 (1989).
- [37] Anderson, P. D., Galaktionov, O. S., Peters, G. W. M., Meijer, H. E. H., *J. Fluid Mech.*,

- 386**, 149–166 (1999).
- [38] Galaktionov, O. S., Anderson, P. D., Peters, G. W. M., van de Vosse, F. N., *Int. J. Num. Meth. Fluids*, **32**, 201–218 (2000).
- [39] Anderson, P. D., Meijer, H. E. H., *Applied Rheology*, **10**(3), 119–133 (2000).
- [40] Spencer, R. S., Wiley, R. H., *J. Colloid Sci*, **6**, 133–145 (1951).
- [41] Anderson, P. D., Galaktionov, O. S., van de Vosse, F. N., Peters, G. W. M., Meijer, H. E. H., *J. Non-Newtonian Fluid Mech.*, **93**(2–3), 265–286 (2000).
- [42] Anderson, P. D., Galaktionov, O. S., Peters, G. W. M., Meijer, H. E. H., *Int. J. Heat Fluid Flow*, **21**(2), 176–185 (2000).
- [43] Ottino, J. M., *Phys. Fluids*, **A3**(5), 1417 (1991).
- [44] Galaktionov, O. S., Anderson, P. D., Kruijt, P. G. M., Peters, G. W. M., Meijer, H. E. H., *Computers and Fluids*, **30**(3), 271–289 (2001).
- [45] Anderson, P. D., Ternet, D. J., Peters, G. W. M., Meijer, H. E. H., *International Polymer Processing*, **04**, 412–420 (2006).
- [46] Elemans, P. H. M., Janssen, J. M. H., Meijer, H. E. H., *J. Rheol.*, **34**(8), 1311 (1990).
- [47] Weber, C., *Z. Angew. Math. Mech.*, **11**, 136 (1931).
- [48] Tjahjadi, M., Stone, H. A., Ottino, J. M., *J. Fluid Mech.*, **243**, 297 (1992).
- [49] Rayleigh, Lord, *Proc. R. Soc., London*, **29**, 71 (1879).
- [50] Tomotika, S., *Proc. R. Soc., London*, **A150**, 322 (1935).
- [51] Chappellear, D. C., *Polym. Prep.*, **5**, 363 (1964).
- [52] Paliarne, J. F., Lequeux, F., *JNNFM*, **40**, 289 (1991).
- [53] Stone, H. A., Leal, L. G., *J. Fluid Mech.*, **198**, 399 (1989).
- [54] Stone, H. A., Leal, L. G., *J. Fluid Mech.*, **206**, 223 (1989).
- [55] Tjahjadi, M., Ottino, J. M., *J. Fluid Mech.*, **232**, 191 (1991).
- [56] Kuhn, W., *Kolloid Z.*, **132**, 84 (1953).
- [57] Mikami, T., Cox, R., Mason, R. G., *Int. J. Multiphase Flow*, **2**, 113 (1975).
- [58] Tomotika, S., *Proc. R. Soc., London*, **A153**, 302 (1936).
- [59] Khakhar, D. V., Ottino, J. M., *Int. J. Multiphase Flow*, **13**(1), 71 (1987).
- [60] Acrivos, A., *4th Ann. N. Y. Acad. Sci.*, **404**, 1 (1983).
- [61] Rallison, J. M., *Annu. Rev. Fluid Mech.*, **16**, 45 (1984).
- [62] Grace, H. P., *Chem. Eng. Commun.*, **14**, 225 (1982).
- [63] Bentley, B. J., Leal, L. G., *J. Fluid Mech.*, **167**, 219 (1986).
- [64] Bentley, B. J., Leal, L. G., *J. Fluid Mech.*, **167**, 241 (1986).
- [65] Meijer, H. E. H., Bos, H. L., in German: *Extruder im Extrusionsprozess*, VDI-Verlag, Düsseldorf, p. 59 (1989); in English: *Academic Seminar: Current Situation and Topics of Polymer Processing Technology*, p. 39, JP90, Tokyo (1990); in Japanese: *Seikei-Kakou*, [*J. Jap. Polym. Process. Soc.*], **3**(1), 33 (1991).
- [66] (a) Elemans, P. H. M., Ph. D. Thesis, Technical University, Eindhoven (1989). (b) Elemans, P. H. M., Bos, H. L., Janssen, J. M. H., Meijer, H. E. H., *Preprints of IACIS Conference/EFCE Event 439, The Preparation of Dispersions*,
- [67] Bruijn, R. A. de, Ph. D. Thesis, Technical University, Eindhoven (1989).

- [68] (a) Janssen, J. M. H., AIO-2 Report, Technical University, Eindhoven, WFW 91.8 (1991).
 (b) Janssen, J. M. H., Peters, G. W. M., Meijer, H. E. H., Preprints of IACIS Conference/EFCE Event 439, The Preparation of Dispersions, p. 121, Veldhoven, The Netherlands, Oct. 14–16, 1991; and Chem. Eng. Sci., **48**(2), 255 (1993).
- [69] Giesekus, H., Rheol. Acta, **2**(2), 112 (1962).
- [70] Tanner, R. L., AIChE J., **22**(5), 910 (1976).
- [71] Fuller, G. G., Leal, L. G., J. Polym Sci, Polym. Phys. Ed., **19**, 557 (1981).
- [72] Olbricht, W. L., Rallison, J. M., Leal, L. G., JNNFM, **10**, 291 (1982).
- [73] Milliken, W. J., Leal, L. G., JNNFM, **42**, 231 (1992).
- [74] Milliken, W. J., Leal, L. G., JNNFM, **40**, 355 (1991).
- [75] Rumscheidt, F. D., Mason, S. G., J. Colloid. Sci., **16**, 238 (1961).
- [76] Bruijn, R. A. de, Preprints of IACIS Conference/EFCE Event 439, The Preparation of Dispersions, p. 103, Veldhoven, The Netherlands, Oct. 14–16, 1991; and Chem. Eng. Sci., **48**(2) (1993).
- [77] Janssen, J. M. H., Meijer, H. E. H., J. Rheol. **37** (4), p. 597 (1993).
- [78] Khakhar, D. V., Ottino, J. M., J. Fluid Mech., **166**, 265 (1986).
- [79] Elemans, P. H. M., van Wunnik, J. M., van Dam, R. A., AIChE Journal **43** (6): 1649–1651 June (1997).
- [80] Knops, Y. M. M., Slot, J. J. M., Elemans, P. H. M., et al. AIChE Journal **47** (8): 1740–1745 Aug. (2001).
- [81] Jackson, N. E., Tucker, C. L., Journal of Rheology **47** (3): 659–682 (2003).
- [82] Yu, W., Bousmina, M., Grmela, M., Paliarne, J. F., Zhou, C. X., Journal of Rheology **46** (6): 1381–1399 (2002).
- [83] Yu, W., Zhou, C. X., Bousmina, M., Journal of Rheology, **49** (1): 215–236 (2005).
- [84] Doi, M., Ohta, T., J. Chem. Phys. **95**, 1242–1248 (1991).
- [85] Maffettone, P. L., Minale, M., Journal of non-Newtonian Fluid Mechanics **78** (2–3): 227–241 (1998)
- [86] Tucker, C. L., Moldenaers, P., Annual Review of Fluid Mechanics **34**: 177–210 (2002).
- [87] Grmela, M., Ait-Kadi, A., Utracki, L., Journal of Non-Newtonian Fluid Mechanics **77**: 253–259 (1998).
- [88] Yu, W., Bousmina, M., Journal of Rheology **47** (4): 1011–1039 (2003).
- [89] Bentley, B. J., Ph. D. thesis, California Institute of Technology, Pasadena (1985).
- [90] Bazhlekov, I., Anderson, P. D., Meijer, H. E. H., J. Colloid Interface Sci., **298**, 369–394 (2006).
- [91] Kruijt-Stegeman, Y. W., van de Vosse, F. N., Meijer, H. E. H., Phys. Fluids, **16**(8), 2785–2796 (2004).
- [92] Bazhlekov, I., Anderson, P. D., Meijer, H. E. H., Phys. Fluids, **16**(4), 1064–1081 (2004).
- [93] Stegeman, Y. W., van de Vosse, F. N., Chesters, A. K., Meijer, H. E. H., Break-up of (non-) Newtonian droplets in a time-dependent elongational flow, in 15th Annual Meeting Polymer Processing Society; Editors: P. D. Anderson and P. G. M. Kruijt, 's-Hertogenbosch, Netherlands, On CD-Rom (1999).

- [94] Stegeman, Y. W., van de Vosse, F. N., Meijer, H. E. H., *CJCHE*, **80**(4), 632–637 (2002).
- [95] Bazhlekov, I., Anderson, P. D., Meijer, H. E. H., *J. Colloid Interface Sci.*, **298**, 369–394 (2006).
- [96] Elmendorp, J. J., Ph. D. Thesis, Technical University, Delft (1986).
- [97] Smoluchowski, M., *Z. Phys. Chem.* **92**, p. 129 (1917).
- [98] Chesters, A. K., *Trans. Ind. Chem. Eng. A*, **69**, 259 (1991).
- [99] MacKay, G. D. M., Mason, S. G., *Canal.1. Chem. Eng.* **41**, p. 203, 1963.
- [100] Chesters, A. K., *Euromech 234, International Conference Turbulent Two-Phase Flow Systems, Toulouse, France* (1988).
- [101] Chesters, A. K., *Int. J. Multi-phase Flow* **2**, 191 (1975).
- [102] Abid, S., Ph. D. Thesis, Inst. Fluid Mech., Toulouse, France (1993).
- [103] Abid, S., Chesters AK, *ML J. Multiphase Flow*, **20**, 613 (1994).
- [104] Chesters, A. K., Hofman, G., *Appl. Sci Res.* **38**, 353 (1982).
- [105] Gisbergen, J. van, Meijer, H. E. H., *J. Rheol.*, **35**(1), 63 (1991).
- [106] Zdravkov, A. N., Peters, G. W. M., Meijer, H. E. H., *J. Colloid Interface Sci.*, **266**(1), 195–201 (2003).
- [107] Zdravkov, A. N., Peters, G. W. M., Meijer, H. E. H., *J. Colloid Interface Sci.*, **296**(1), 86–94 (2006).
- [108] Ivanov, I. B., *Pure Appl. Chem.* **52**, 1241 (1980).
- [109] Hu, Y., Lips, A., *Phys. Rev. Lett.* **91**, 44501 (2003).
- [110] Hansen, S. G., Peters, G. W. M., Meijer, H. E. H., *J. Fluid Mech.*, **382**, 331–349 (1999).
- [111] Manas-Zloczower, L., Nir, A., Tadmor, Z., *Rubber Chem. Techn.*, **55**, 1250 (1982).
- [112] Manas-Zloczower, I., Nir, A., Tadmor, Z., *Rubber Chem. Techn.*, **57**, 583 (1984).
- [113] Levenspiel, O., in *Chemical Reaction Engineering*, 2M ed., p. 292, John Wiley & Sons, New York (1972).
- [114] Janssen, J. M. H., Meijer, H. E. H., *Polymer Engng. & Sc.*, **35**(22), 1766–1780 (1995).
- [115] Becher, P., McCann, Mi., *Langmuir* **7**, 1325 (1991).
- [116] Krieger, L. M., Dougherty, Ti., *Trans. Soc. Rheol* **3**, 137 (1959).
- [117] Muzio, F. J., Tjahjadi, M., Ottino, J. M., *Phys. Rev. Let.* **67** (1), 54 (1991).
- [118] Utracki, L. A., *J. Rheol.* **35** (8), 1615 (1991).
- [119] Avalosse, T., Crochet, M., Fobelets, A., Dehennau, C., *Proc. XI-th Int. Congr. on Rheol, Brussels Belgium*, p. 318, Elsevier Amsterdam (1992).
- [120] Avalosse, T., Crochet, M., Fobelets, A., Dehennau, C., *PPS meeting for the Americas, Morgantown USA, August* (1993).
- [121] Jana, S. C., San, M., *Polymer* **45** (5): 1665–1678 (2004).
- [122] Sau, M., Jana, S. C., *AIChE Journal* **50** (10): 2346–2358 (2004).
- [123] Perilla, J. E., Jana, S. C., *AIChE Journal* **51** (10): 2675–2685 (2005).
- [124] Dharaiya, D. P., Jana, S. C., Lyuksyutov, S. F., *Polymer Engineering and Science* **46** (1): 19–28 (2006).
- [125] Zumbrennen, D. A., Inamdar, S., *Chemical Engineering Science* **56** (12): 3893–3897 (2001).

- [126] Zumbrunnen, D. A., Chhibber, C., *Polymer* **43** (11): 3267–3277 (2002).
- [127] Zumbrunnen, D. A., Subrahmanian, R., Kulshreshtha, B., Mahesha, C., *Advances In Polymer Technology* **25** (3): 152–169 (2006).
- [128] Almusallam, A. S., Larson, R. G., Solomon, M. J., *Journal Of Rheology* **48** (2): 319–348 (2004)
- [129] Yu, W., Zhou, C. X., *Journal Of Rheology* **51** (2): 179–194 (2007).
- [130] Peters, G. W. M., Hansen, S. G., Meijer, H. E. H., *J. Rheol.*, **45**(3), 659–689 (2001).
- [131] Jansseune, T., Moldenaers, P., Mewis, J., *Rheologica Acta* **43** (6): 592–601 (2004).
- [132] Palierne, J. F., *Rheologica Acta* **29**, 204–215 (1990).
- [133] Vinckier, I., Moldenaers, P., Mewis, J., *Journal Of Rheology* **40** (4): 613–631 (1996).
- [134] Vinckier, I., Moldenaers, P., Mewis, J., *Journal Of Rheology* **41** (3): 705–718 (1997).
- [135] Van Hemelrijck, E., Van Puyvelde, P., Moldenaers, P., *Macromolecular Symposia* **233**: 51–58 (2006).
- [136] Jansseune, T., Moldenaers, P., Mewis, J., *Rheologica Acta* **43** (6): 592–601 (2004).
- [137] Cahn, J. W., Hilliard, J. E., *Journal Of Chemical Physics* **28**: 258 (1958).
- [138] Cahn, J. W., *Journal Of Chemical Physics* **42**: 93 (1965).
- [139] Khatavkar, V., Anderson, P. D., Meijer, H. E. H., *Chem. Eng. Sc.*, **61**(8), 2364–2378 (2006).
- [140] Yue, P. T., Feng, J. J., Liu, C., Shen, J., *Journal of Fluid Mechanics* **515**: 293 (2004).
- [141] Lowengrub, J., Truskinovsky, L., *Proceedings Of The Royal Society Of London Series A- Mathematical Physical And Engineering Sciences* **454**: 2617 (1998).
- [142] Neumann, E. B., He, D. Q., *Chemical Engineering Science* **56**: 1999 (2001).
- [143] Anderson, D. M., McFadden, G. B., Wheeler, A. A., *Annual Review Of Fluid Mechanics* **30**: 139 (1998).
- [144] Prusty, M., Keestra, B. J., Goossens, J. G. P., Anderson, P. D., *Chem. Eng. Sci.*, **62**(6), 1825–1837 (2007).
- [145] Keestra, B. J., Van Puyvelde, P. C. J., Anderson, P. D., Meijer, H. E. H., *Phys. Fluids*, **15**(9), 2567–2575 (2003).
- [146] Anderson, P. D., Keestra, B. J., Hulsen, M. A., *J. Comput. Phys.*, **212**(1), 268–287 (2006).
- [147] Naumann, E. B., He, D. Q., *Rheol. Acta*, **29**, 204–214 (1990).
- [148] Carriere, C. J., Cohen, A., *J. Rheol.*, **35**(2), 205 (1991).
- [149] Khakhar, D. V. and Franjione, J. G. and Ottino, J. M., *Chemical Engineering Science*, **42**, 12 (1987).
- [150] Wetzal, E. D. and Tucker, C. L., *International Journal of Multiphase Flow*, **25**(1), 35–61 (1999).
- [151] Ha, J. W. and Leal, L. G., *Physics of Fluids*, **13**(6), 1568–1576 (2001).
- [152] Ross, S. L. and Verhoff, F. H. and Curl, R. L., *Industrial & Engineering Chemistry Fundamentals*, **17**(2), 101–108 (1978).
- [153] Eggleton, C. D., Tsai, T. M. and Stebe, K. J., *Physical Review Letters*, **87**, 4 (2001).

6c. Some book chapters for further reading

1. H.E.H. Meijer, J.M.H. Janssen, P.D. Anderson, *Mixing of immiscible liquids*, in *Mixing and Compounding of Polymers: Theory and Practice*; Editors: Ica Manas-Zloczower, 41-177, Hanser Publications, Book Chapter, ISBN 978-1569904244 (2009)
2. P.D. Anderson, H.E.H. Meijer, *Scale down of mixing equipment: microfluidics*, in *Mixing and Compounding of Polymers: Theory and Practice*; Editors: Ica Manas-Zloczower, 645-697, Hanser Publications, Book Chapter, ISBN 978-1569904244 (2009)
3. H.E.H. Meijer, *Materials Science and Technology. A Comprehensive Treatment. Volume 18. Processing of Polymers*, VCH-Wiley, Weinheim, Edited Book 3-527-26829-4, pp 1 - 787 (1997)
4. H.E.H. Meijer, Chapter 1: Processing for Properties, In: *Materials Science and Technology. A comprehensive treatment. Volume 18.*; Editors: Vol Ed. H.E.H. Meijer, Series eds.: R.W. Cahn, P. Haasen, E.J. Kramer, VCH - Wiley, Weinheim, ISBN 3-527-26829-4, pp 3-75 (1997)
5. H.E.H. Meijer, L.E. Govaert, T.A.P. Engels, *Predicting Mechanical Performance of Polymers*, in *Macromolecular Engineering, Precise Synthesis, Materials properties, Applications*; Editors: K. Matyjaszewski, Y. Gnanou, and L. Leibler, 1783-1825, Wiley-VCH Verlag GmbH & Co, KGaA, Weinheim, Book Chapter, ISBN 978-3-527-31446-1 (2007)